Control-Oriented Multi-physics Battery Modeling for Fast Discharging Near the Venting Threshold

by

Vivian Tran

A dissertation submitted in partial fulfillment
of the requirements for the degree of
Doctor of Philosophy
(Mechanical Engineering)
in the University of Michigan
2025

Doctoral Committee:

Research Associate Professor Jason Siegel, Co-Chair
Professor Anna Stefanopoulou, Co-Chair
Associate Professor Neil Dasgupta
Associate Professor Venkat Viswanathan

Vivian Tran
vvttran@umich.edu
ORCID iD: 0000-0002-9660-8090

© Vivian Tran 2025

DEDICATION

To my family for their unwavering support.

ACKNOWLEDGEMENTS

First and foremost, I would like to thank my advisors, Professor Anna Stefanopoulou and Professor Jason Siegel. Thank you for always believing in me and helping transform my ideas into actionable research to-dos. Your expertise and encouragement have not only shaped my research but also contributed to my growth into a more confident and well-rounded researcher. I am extremely lucky to have had the opportunity to learn from and work with you both.

I am also grateful to the members of my dissertation committee, Professor Neil Dasgupta and Professor Venkat Viswanathan, for dedicating the time and effort to review my work. Your constructive comments and insightful feedback challenged me to expand my perspective on the context and applications of my research.

This research was made possible through the financial support of several organizations, including the National Science Foundation under Grant No. 1762247, the National Center for Manufacturing Sciences, and an appointment to the Research Participation Program at the National Vehicle and Fuel Emissions Laboratory, U.S. Environmental Protection Agency (EPA), administered by the Oak Ridge Institute for Science and Education through an interagency agreement between the U.S. Department of Energy and EPA. I want to thank my colleagues at the EPA, especially Matt Brusstar, for being a supportive supervisor and mentor. Your guidance has helped me stay grounded in the bigger picture, and I continue to learn something new from our conversations.

A heartfelt thank you to all of my incredible current and former labmates in the Powertrain Control Lab and Battery Control Group for making the hard work so much fun. From our spontaneous hangouts to navigating tight submission deadlines, your camaraderie and encouragement have kept me motivated. You have made this research journey both productive and unforgettable, and I feel very lucky to have been surrounded by such a supportive and inspiring group.

I am also thankful for the friends I have made along the way, especially the Zetus group. From game nights and delicious food to all the (mis)adventures and travel, you inspire me to expand my horizons. I want to give special thanks to Ellen Kim and Owen Marshall, who have been there since the beginning of my graduate school journey. Thank you for bringing fun and laughter into my life, especially during the rough patches along the way.

Last but not least, to my family, thank you for your unconditional love and encouragement and for teaching me the value of learning and hard work. Without your guidance and sacrifices, I would not have made it to Michigan. Your unwavering support, from care packages to tax assistance, has been a constant source of encouragement throughout my journey. You inspire me every day to continue to chase my dreams.

TABLE OF CONTENTS

DEDICATION ii

ACKNOWLEDGEMENTS iii

LIST OF FIGURES viii

LIST OF TABLES xii

LIST OF APPENDICES xiii

ABSTRACT xiv

CHAPTER

1 Introduction 1

1.1 Background and Motivation 1
1.1.1 Challenges of Li-ion battery failures and reignitions 1
1.1.2 Role of modeling for battery safety 3
1.1.3 Normal operation for Li-ion batteries 4
1.1.4 Evolution of Li-ion Battery Failures 5
1.2 Dissertation Contributions and Organization 9

2 Control-oriented Electro-thermo-mechanical Model with Fast Discharge Control Application 11

2.1 Introduction 11
2.2 External short circuit experiments 13
2.2.1 Experimental setup 13
2.2.2 Experimental results 14
2.2.3 Experimental limitations 16
2.3 Electrical model 17
2.3.1 Nominal single RC model 17
2.3.2 Tab and external circuit resistances 18
2.3.3 Scaling of the nominal RC parameter functions 19
2.3.4 Equivalent circuit model results 20
2.4 Thermal model 21
2.4.1 Thermal model parameterization 23
2.4.2 Thermal model parameterization results 24

2.5 Pouch first venting model . . . 26
2.5.1 Geometric relationships . . . 28
2.5.2 Force balance . . . 30
2.5.3 Stage 1: No gas generation . . . 31
2.5.4 Stage 2: Gas generation *before* pouch lift-off . . . 31
2.5.5 Stage 3: Cell expansion due to gas generation . . . 32
2.5.6 Temperature-dependence of foam stiffness . . . 35
2.6 Electro-thermo-mechanical model validation . . . 35
2.7 Model predictive controller . . . 38
2.8 Fast discharge results and discussion . . . 39
2.9 Summary . . . 42

3 Extending a Physics-based Electrochemical Model from Normal Operation to High C-rate Discharge and Venting . . . 44

3.1 Introduction . . . 44
3.2 Multiphysics model . . . 45
3.3 Single particle model with electrolyte . . . 45
3.3.1 Solid diffusion coefficient parameterization . . . 46
3.3.2 Extending the nominal SPMe for an ESC . . . 48
3.3.3 Effect of concentration-dependent diffusion . . . 51
3.4 SEI decomposition parameterization . . . 54
3.4.1 SEI decomposition parameterization results . . . 55
3.5 Results and discussion . . . 57
3.6 Summary . . . 60

4 Pouch Venting Model Global Sensitivity Analysis for Fresh and Aged Cells 61

4.1 Introduction . . . 61
4.2 Global sensitivity analysis . . . 62
4.2.1 Morris method . . . 62
4.2.2 Sobol method . . . 65
4.3 Results and discussion . . . 66
4.3.1 Global sensitivity analysis . . . 66
4.3.2 Modeled implications for force-based detection and control . . . 68
4.4 Summary . . . 72

5 Inhomogeneity-aware State-of-Health Estimation for Bounding Li Consumption from SEI growth in Aged Cells . . . 75

5.1 Introduction . . . 75
5.2 Cell aging experiments . . . 77
5.2.1 Reference performance tests . . . 78
5.2.2 Electrode open-circuit potential characterization . . . 79
5.3 Open-circuit voltage model . . . 80
5.3.1 Full-cell OCV model . . . 80
5.3.2 LLI and LAM degradation modes . . . 81
5.3.3 Modeling inhomogeneity in aged electrode OCP . . . 81

5.4 Model parameterization 84
5.4.1 Data preprocessing 84
5.4.2 Defining the optimization problem 84
5.5 Results and discussion 86
5.5.1 Experimental results 86
5.5.2 Characterization and modeling results 92
5.5.3 Temperature-dependence of inhomogeneity growth 93
5.5.4 Relating degradation modes to SEI decomposition 97
5.5.5 Comparing model complexity and performance 98
5.6 Summary 98

6 Conclusion 100

6.1 Summary of contributions 100
6.2 Future work and open challenges 102
6.2.1 Implementation of model-based algorithms for battery management systems 102
6.2.2 Relating degradation pathways to failure behavior 103
6.2.3 Instrumentation in large systems 103
6.2.4 Early failure detection algorithms 104
6.2.5 Discharge mitigation and infrastructural requirements 105

APPENDICES 107

BIBLIOGRAPHY 116

LIST OF FIGURES

FIGURE

1.1 Growth in global LIB demand and incidents [1, 2, 3]. 2
1.2 Example EV fire emergency response and disposal timeline based on accounts from [4, 5, 6]. After the initial incident, battery fires can reignite until the stranded energy is removed. 2
1.3 Discharge and charge process inside a lithium-ion cell [7]. 4
1.4 Evolution of exothermic reactions leading to thermal runaway 6
1.5 Effect of SOC and SOH on thermal runaway onset and peak temperatures . . . 8

2.1 Modeling the progression of short circuit abuse and first venting hazard. An electrochemical model predicts the electrical behavior of a cell as it discharges. The corresponding Joule heating informs a thermal model that predicts the cell temperature. At high temperatures, gases are generated from electrolyte vaporization and SEI decomposition, building the internal cell pressure until the cell vents. 11
2.2 Diagram of external short circuit setup. Red and grey lines indicate positive and negative terminal wire connections, respectively, for the main circuit. Measurement signals from the instrumented fixture, cell, and gas sensor including current (I), terminal voltage (V_T), cell temperature (T), and expansion force (F). . . . 14
2.3 Experimental data for a 15-minute external short circuit. From top to bottom, these are measured cell current, voltage, center surface temperature, and compression stress from cell expansion, all plotted versus linear time (left) and log time (right). 15
2.4 Battery EqCM with a single RC pair and additional series R_{tab}. 17
2.5 Nominal EqCM simulation of 2C pulse testing and calculated parameters 18
2.6 Comparison of ESC experimental data and electrical model results for Cell a) 100A, a) 100B b) 75, and c) 50. 22
2.7 Thermal fit results for all cells for predicted temperature (top row) and rate of change of temperature (bottom row) using total heat generation calculated from data then filtered with $\pm(0.01\tilde{I} + 0.5)$ A current error. Electrolyte vaporization before venting occurs between the dotted lines (magenta), where the mismatch in $\frac{dT}{dt}$ trajectory due to vaporization cooling can be observed in the insets. . . . 25
2.8 Evolution of cell expansion at high temperatures. All foam sheets are illustrated as a single, thick sheet for simplicity 27
2.9 Diagram of force relationships and geometric constraints on the pouch cell in the fixed displacement fixture 29

2.10 Gas pressure build-up at the surface between porous cell stack material and pouch materials sharing the load with the solid cell stack material. 32
2.11 Combined EqCM-based multiphysics model simulation for a 15-min ESC with parameters from fitting Cell 100A. The parameters that were fitted for each cell were R_{esc} and R_{tab}. The h, C_p, α, and β fitted for Cell 100A were used to simulate all SOCs. 36
2.12 Contributions to total a) heat generation and b) gas pressure for Cell 100A . . 37
2.13 Simulated 20-minute emergency discharge results with the nominal operating temperature limit and extended temperature limit with and without temperature and pressure venting constraints. 40

3.1 Diagram of submodel relationships and the parameters identified. SEI decomposition heating (grey) is not considered during parameterization but is included in the combined model. I is current; V_{T} is terminal voltage; x_{SEI} is the mole ratio of SEI to negative active material; P_{elyte} is electrolyte saturation pressure, and F is the cell expansion force. The parameters listed in blue are identified for the corresponding submodel. 46
3.2 Example simulation from fitting electrode diffusion coefficients for a 2C pulse at $\text{SOC}_0 = 0.73$. Terminal voltage error is minimized during the rest period by solving Eq. 3.1. 47
3.3 Diffusion coefficients fitted from the 2C pulse test where $D_{\text{s,n}} = \gamma_n D_{\text{s,n,0}}$ and $D_{\text{s,p}} = \gamma_p D_{\text{s,p,0}}$, where z is SOC. 48
3.4 2C pulse test validation with constant and fitted diffusion coefficients where e_V is the voltage error. Adapted from [8] 49
3.5 Effect of concentration-dependent diffusion [8]. ESC simulation with Cell 100A. Transitions are marked based on the simulation with concentration-dependent diffusion (red). 52
3.6 Temporal evolution of voltage overpotentials and spatial evolution of limiting concentrations during the transition points. The first transition is caused by concentration depletion in the electrolyte of the positive electrode. The second is due to increasing positive particle concentration overpotential from the steep decrease in U_p at high stoichiometric. Further definitions and equations are provided in Section B.1. 53
3.7 Result of tuning A_{SEI} using measured temperature with ±2.2 °C measurement bias error (right axis) and applying the literature value from Coman et al 2017 (blue), the cell's fitted value (green), and using the fitted value from Cell 100A (red) 56
3.8 Combined multiphysics model simulation for a 15-min ESC with parameters from fitting Cell 100A. Submodel results with data inputs are shown to isolate the effect of parameter mismatch. The parameters that were fitted for each cell were R_{ESC}, R_{tab}, h, C_p, and A_{sei} with $D_{s,n}$ and $D_{s,n}$ only fitted for Cell 100A. The h, C_p, A_{sei}, $D_{s,n}$, and $D_{s,n}$ fitted for Cell 100A were used to simulate all SOCs. 58

4.1 Morris method sensitivity analysis for cell expansion stress (top) and vent timing (bottom) for a fresh cell and an aged cell. 67

4.2 Sobol indices for cell expansion stress (top) and vent timing (bottom) for a fresh cell and an aged cell. 69
4.3 Effect of increasing preload pressure according to the venting model. As the preload pressure increases, the drop in expansion force becomes less observable. After the stress due to solid expansion surpasses the critical venting pressure, venting is unobservable. 71
4.4 Increased temperature-dependence of foam stiffness improves observability of solid expansion stress 72
4.5 Example of uncertainty in $x_{\text{SEI},0}$, A_{SEI}, and $E_{a,\text{SEI}}$, respectively, for fresh and aged cells, where $\Delta\sigma_{\text{crit}} = P_{\text{crit}} - \sigma_0$. 73

5.1 HPPC current and voltage profiles used to calculate $R_s = R_{0.4\text{s}}$ and $R_{10\text{s}}$. Each charge and discharge pulse is 10 s long at 2 A 79
5.2 Constructed aged negative electrode OCP. Assuming a normal distribution of C_n, $U_n(C_n)$ is calculated for each representative electrode over a range of z-scores in $\mathcal{N}(C_n, \sigma_{C_n})$ (grey), then a weighted average is calculated to model an aged electrode with inhomogeneity (red) where the weights are proportional to $f_n(C_{n,z})$ from Eq. 5.9. The opacity of each $c_{n,z}$ and $U_{n,z}^{\text{fresh}}(x|_{c_{n,z}})$ reflect the z-score and contribution to the inhomogeneous U_n. For comparison, the U_n^{fresh} is plotted in blue. 83
5.3 Parameterization SOC window for calculating RMSE_{dVdQ} (Eq. 5.15). The location of the next highest peak in the data (Point A) determines the threshold and corresponding minimum SOC (Point B). In this example, data in the shaded low SOC region is ignored. 86
5.4 The peaks observed in the full cell DV are attributed to $\frac{dU_n}{dQ}$ and are used to initialize negative electrode parameters. The voltage (black) and DV (red) signals for the PE (top), full cell (middle), and NE (bottom) are plotted to illustrate the alignment of the transition peaks. 87
5.5 Evolution of R_s charge pulse resistance versus Q with degradation 88
5.6 Capacity loss (left) and resistance growth (right) for (a) cycle-aged cells, (b) only C/3 cycle-aged cells to show the effect of temperature, and (c) only RT-aged cells to show the effect of C-rate. The $R_{0.4\text{s}}$ at 50% SOC, where SOC is calculated relative to the aged cell. 90
5.7 Comparison of measured and modeled voltage and differential voltage of Cell 85 (45°C, C/3) from fresh to 50% SOH 93
5.8 Parameterized degradation modes for all cycle-aged cells for (a) C/3 and 2C cycle-aged cells to show the effect of temperature and (b) only room-temperature cells to show the effect of C-rate. 94
5.9 Relationships between σ_{C_n}, R_s, LAM, and LLI for C/3 cycle aging cells show distinct trajectories for cold- and hot-temperature cells. 95
5.10 Recovery of inhomogeneity while resting after cycling. Values of σ_{C_n} are normalized between the last RPT before resting and the last available RPT, assuming the process is at quasi-steady state. 96

5.11 Comparison of error metrics across SOH to illustrate the impact of adding differential voltage error (V+DV) to the loss function and σ_k parameter to θ (V+DV+σ) compared to conventional voltage fitting (VF). Each set of violin plots represents the distribution of error across all cells within the respective 10% capacity loss window. The median of each distribution is indicated with a dot, while the bars indicate the extrema. 99

6.1 Overview of emergency discharge with EVSEs 106

A.1 Thermocouple placement on surface of pouch cell 107
A.2 Cell edge and center surface temperatures measured during the ESC experiments. The center surface temperature was used for model development in this work. . 108

LIST OF TABLES

TABLE

2.1 Summary of key metrics over the 15-min ESC. 16
2.2 Summary of electrical model parameters from Cell 100A 20
2.3 Final SOC error and RMSE of current, voltage, and SOC 21
2.4 Summary of fitted thermal model parameters and simulation errors. Errors include the before the boiling point is reached ($\text{RMSE}_{T<BP}$) and temperature RMSE for the 15-min simulation (RMSE_T); dT/dt error for the 15-min simulation ($\text{RMSE}_{\Delta T}$); peak temperature error ($\Delta T_{\max}$); and temperature error that can be accounted for by electrolyte vaporization ($\Delta\ \text{T}_{\text{H}_{\text{vap}}}$). 26

3.1 Summary of fitted R_{ESC}, R_{tab}, initial current error (ΔI_0) and initial voltage error ($\Delta V_{\text{T},0}$) for each cell 51
3.2 Summary of fitted A_{SEI} and venting model $\Delta\sigma$ prediction error for three values of A_{SEI}. Error metrics from simulation results with A_{SEI} equal to the literature value, value fitted to the cell, and value fitted to Cell 100A ($A_{\text{SEI}}^{100\text{A}}$) are presented. The error metrics include root-mean-squared error of Δ_σ ($\text{RMSE}_{\Delta\sigma}$) and error in venting timing (Δt_{vent}). $\text{RMSE}_{\Delta\sigma}$ is calculated for the time before venting occurs in simulation. The fit for Cell 100B used interpolated temperature data where data was missing. 55
3.3 Summary of combined electrochemical-thermal-venting model simulation errors. $\Delta\text{SOC}_\text{f}$ is the error in the final SOC. $\Delta T_{\max}$ and $\text{e}_{\Delta\sigma}^{\max}$ are the errors in the maximum temperature and maximum cell expansion stress, respectively. All RMSEs are calculated for the 15-minute period. The exceptions are Cells 100A and 100B which vented, so the RMSE_σ is calculated until the simulation vents. 59

4.1 Overview of venting model parameters included in the sensitivity studies. Parameter ranges used for fresh cell analysis are assumed to be $\pm 10\%$ of the nominal. Parameter ranges not listed for aged cell analysis are the same as for the fresh cell. 64

5.1 Overview of test conditions 78
5.2 Summary of initial conditions, upper bounds, and lower bounds for model parameterization 88

B.1 Summary of venting and thermal model parameters 113
B.2 Summary of SPMe parameters 114
B.3 SPMe open circuit potential and active material diffusivity 115

LIST OF APPENDICES

A Pouch Cell Temperature Measurements 107

B SPMe-based Multiphysics Model Equations and Parameters 109

Single Particle Model with electrolyte equations 109

ABSTRACT

To improve lithium-ion battery (LIB) safety, predictive multiphysics algorithms are needed that can manage battery operation from normal to abnormal conditions. To address this gap, this dissertation develops control-oriented multiphysics LIB models that capture behavior from normal operation to first venting with minimal parameterization.

Two reduced-order multiphysics models are developed by extending a normal operation model to simulate LIB pouch cell behaviors under high temperatures and currents, observed during external short circuit (ESC) experiments. This includes diffusion-limited electrical behaviors, cell expansion, gas generation, and first venting. The model emphasizes computational efficiency by coupling an equivalent circuit model (EqCM) with lumped thermal and cell venting phenomena. This parameterizable model is used to develop a model-predictive controller for safe and fast emergency discharge. Simulations show that imposing temperature and pressure constraints while maximizing discharge current allows a cell to discharge to 60% SOC in 2.5 minutes while avoiding venting. However, the empirical EqCM cannot transition between normal and early failure conditions. To address this, a physics-based Single Particle Model with Electrolyte (SPMe) is used to capture the transition between normal and abnormal behavior, predicting venting timing within 10 seconds, consistent with experiments.

A global sensitivity analysis of the pouch cell venting model highlights that uncertainties in preload, solid-electrolyte interphase (SEI) decomposition parameters, and temperature-dependent foam stiffness strongly influence the cell expansion force across temperature and age. The venting model shows that gas generation is highly sensitive to SEI stability and quantity, which are difficult to quantify in situ.

To this end, a voltage fitting method is combined with a modeled electrode capacity distribution, where the standard deviation represents cell inhomogeneity. Inhomogeneity can accelerate degradation in localized regions, increasing the risks of failure. Taking into account inhomogeneity when characterizing degradation in cells with $< 50\%$ capacity loss significantly reduced the differential voltage error throughout LIB life. These advances pave the way for an advanced state-of-health (SOH) estimation that accounts for inhomogeneity to help guide robust, aging-aware detection and mitigation strategies.

CHAPTER 1

Introduction

1.1 Background and Motivation

With the growing prevalence of Li-ion battery (LIB) systems, there is an urgent need for effective early failure detection, hazard mitigation, and fire reignition prevention to manage thermal runaway (TR) and its propagation (TRP). To develop effective strategies, we need battery models that can predict the state-of-charge (SOC), temperature, and expansion, from normal operation to the onset of TR. Modeling allows for testing under a wide range of conditions beyond typical experiments and enables adaptive battery management system (BMS) algorithms, including early detection and safe discharge mitigation. The research presented in this thesis aims to bridge the modeling gap by extending battery models of normal operation to capture the evolution of early battery failure behaviors, including first venting before TR, and to demonstrate the application for control.

1.1.1 Challenges of Li-ion battery failures and reignitions

As demand for LIBs grows, so does the frequency of LIB failure incidents and public concern about battery safety (Fig. 1.1). The growth in demand is mainly driven by electric vehicles (EVs) and battery energy storage systems (BESSs), with significant growth projected for the next decade as new markets and regions electrify [9, 10, 11]. Although still rare, the increasing frequency and high-profile nature of select LIB failure incidents have raised public concerns about battery safety. In dense areas, the consequences can be magnified as fires spread to neighboring vehicles and infrastructure, causing significant damage and putting public health and safety at risk [12, 13].

Furthermore, responding to LIB fires poses additional challenges for emergency responders due to the emission of toxic and flammable gases and the risks of explosion and reignition, which stretch the limited resources of average fire departments and tow yards [4]. Compared to conventional vehicles, fighting EV fires requires up to 40 times more water and over 24 hrs

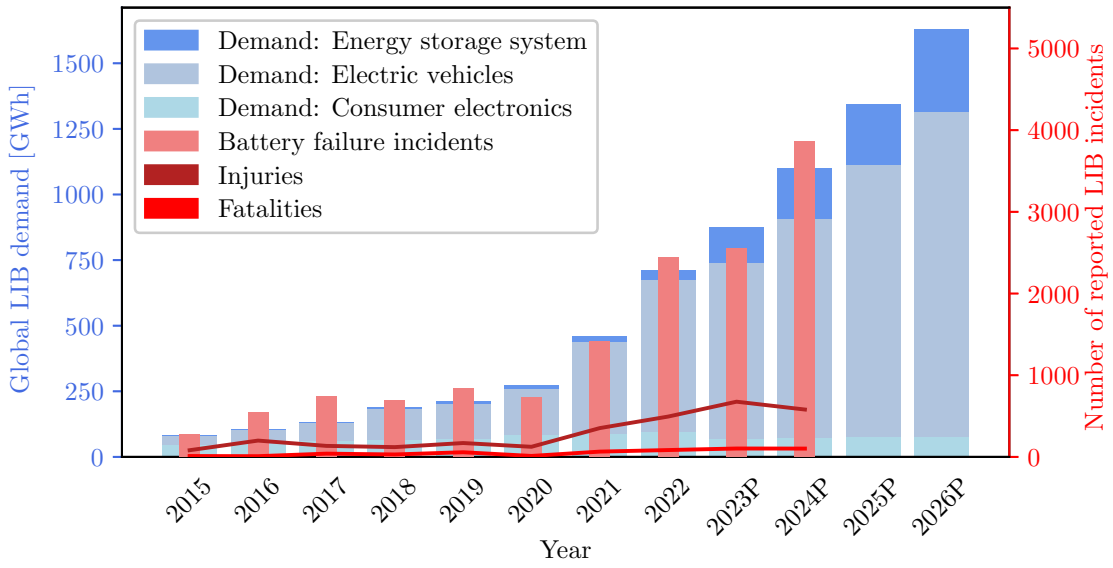


Figure 1.1: Growth in global LIB demand and incidents [1, 2, 3].

due to reignitions from stranded energy in the system [5, 14]. As illustrated in Fig. 1.2, reignition risks endanger reverse logistics workers until the system can be deenergized, even months after the original incident [5, 6, 15].

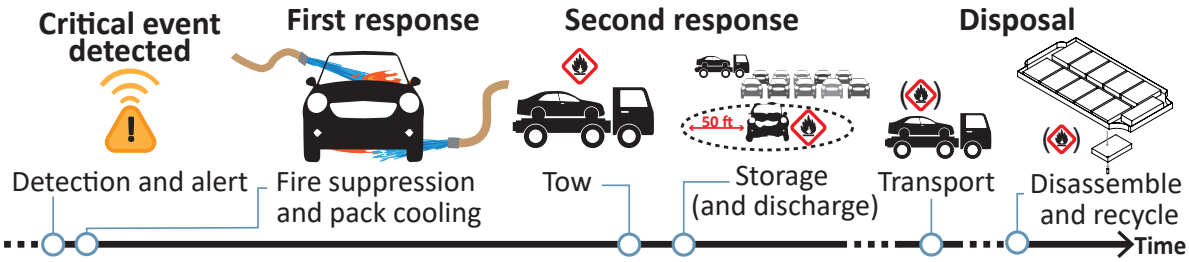


Figure 1.2: Example EV fire emergency response and disposal timeline based on accounts from [4, 5, 6]. After the initial incident, battery fires can reignite until the stranded energy is removed.

Current deenergization strategies for large LIB systems are slow, space-intensive, and require specialized equipment. Manufacturer and aftermarket discharge tools (e.g. resistor banks) can discharge stranded energy, but may require an intact BMS or specific configuration [5]. Damaged LIB systems can also be submerged in water to discharge for days or weeks. For transporting damaged EVs in Europe, cranes are used to place EVs into water-filled containers, but cranes are unavailable to most U.S. fire departments [16, 17]. Alternatively, tow yards can build makeshift dams around damaged EVs to submerge the damaged packs, but second-responders are still vulnerable during transport [18]. Rather than deenergizing post-failure, this thesis considers proactive discharge mitigation via the

BMS, addressing the problem at the source by preemptively removing stranded energy when a failure is detected. While this is a more recent concept enabled by model-based control, it is only one application for modeling in LIB safety.

1.1.2 Role of modeling for battery safety

In general, the reliability of conventional threshold-based detection methods and built-in passive protections depends on system design and environmental, operational, and system conditions [19]. However, these limitations can be addressed by developing advanced model-based detection and mitigation strategies for BMSs. Model-based methods can enable more accurate predictions of LIB failure and more adaptive mitigation responses to a wide range of real-world scenarios. Control-oriented multiphysics modeling plays an important role in developing and testing these algorithms and is the focus of this thesis.

For conventional detection, the reliability of each sensor alone depends on several factors, including sensor placement, cell-module-pack configuration, age of the system, and more [19, 20]. In addition to using existing system sensors like current, voltage, and temperature, novel sensors are being explored, including gas concentration and expansion force, which can provide earlier and more observable indications of impending TR [20, 21]. Model-based detection methods can set adaptive thresholds to account for normal, long-term changes in the system (e.g. LIB aging and degradation), which improves detection accuracy and robustness. Multiphysics modeling also adds the capability for multi-modal sensor fusion, which combines signals from different types of sensors to compensate for individual weaknesses and provide a more comprehensive understanding of the LIB system's condition.

For proactive mitigation strategies, discharge to low SOC is one method that can decrease the risk and severity of TR and slow or stop the propagation of TR [22, 23]. Proactively discharging a system can remove remaining stored energy before it becomes stranded, helping to eliminate the risk of fire reignitions. However, discharging too quickly may generate significant heat, causing gas generation, cell expansion, and first venting, introducing additional fire hazards. Model-based control provides guarantees to help ensure that safety constraints are not violated. Ultimately, mitigation strategies require a holistic, multiphysics understanding of battery failure behaviors to balance safety risks with limited time to act.

Furthermore, modeling can effectively broaden the testing scope during algorithm development beyond typical experiments. Experimental testing can be limited in scope by practical considerations and overlook real-world factors, including manufacturing variability and LIB degradation, which can be prohibitively expensive and time-consuming to address. Modeling can help address the gaps if the relevant phenomena are well-represented. While

modeling can support the development of additional smart BMS capabilities, the effectiveness of model-based algorithms depends on various factors, including model accuracy and computational complexity, which involve inherent trade-offs.

1.1.3 Normal operation for Li-ion batteries

To better understand and predict the evolution of LIB failures and develop informed strategies for detection and hazard mitigation, we need to first understand how LIBs work. Lithium-ion batteries are rechargeable batteries popular due to their high energy density, low self-discharge, and long lifespan. LIB cells have six main components: positive and negative electrodes, positive and negative current collectors, electrolyte, and separator. The electrodes are porous structures composed of a matrix of active material particles, a polymeric binder, and conductive additives, with electrolyte filling the pores. The active material for the positive electrode is a lithium metal oxide (LMO), e.g lithium nickel-manganese-cobalt (NMC) and lithium iron phosphate (LFP), while the negative electrode active material is usually graphite for most commercial LIBs. The aluminum and copper foil current collectors are used as electrode substrates for the positive and negative electrodes, respectively.

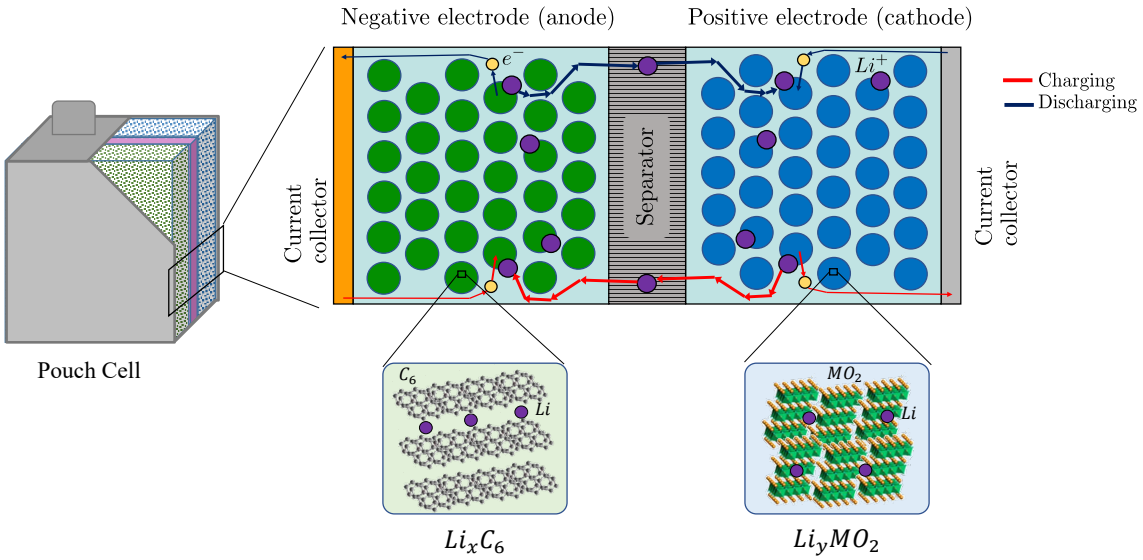


Figure 1.3: Discharge and charge process inside a lithium-ion cell [7].

During charge and discharge of a cell, Li is effectively transferred from one electrode to the other. Li deintercalates and is oxidized to Li^+ at the surface of the active material particle, which diffuses through the separator to the opposite electrode, creating an ionic current. Meanwhile, the electrons travel a conductive path from one current collector to the other through an external circuit, creating an electronic current. At the opposite electrode,

the ions are reduced to Li atoms and reintercalate into the active material. The chemical reactions that occur at the surface of the negative graphite and positive LMO particles are

$$\mathrm{Li_xC_6} \underset{\mathrm{c}}{\overset{\mathrm{d}}{\Longleftrightarrow}} x\mathrm{Li^+} + x\mathrm{e^-} + \mathrm{C_6}$$
$$\mathrm{Li_yMO_2} + (1-y)\mathrm{Li^+} + (1-y)\mathrm{e^-} \underset{\mathrm{c}}{\overset{\mathrm{d}}{\Longleftrightarrow}} \mathrm{LiMO_2}$$

where the stoichiometric states x and y represent the degree of lithiation of the negative and positive electrodes, respectively. In this case, the forward reaction occurs on discharge, and the backward reaction occurs on charge.

During normal operation, LIBs experience degradation and aging, noticeable through loss of performance, e.g., reduced capacity and power. The connection between the operating conditions, evolution of underlying degradation mechanisms, and battery performance and safety is complex. However, there are two important mechanisms to note. The first is solid-electrolyte interphase (SEI) growth, where electrolyte decomposition products form a passivation layer on the negative electrode particles, which grows over the battery's life, regardless of cycling. Additionally, during unfavorable charging conditions, Li plating can also occur on the surface of the negative electrode instead of intercalating into the particles, which can create and grow dendrites that are notorious for causing internal short circuit failures. High-level, parameterizable states, also known as degradation modes, can in part capture the effect of these mechanisms. These are typically considered to be loss of Li inventory (LLI) and loss of active material (LAM) from each electrode. The LLI is typically the main mode of capacity loss and is a composite of degradation mechanisms, including SEI growth, electrolyte decomposition, Li plating, and LLI due to LAM.

As cells degrade, their safety behaviors will evolve, potentially compromising or improving safety, depending on the metrics. In this thesis, SEI plays an important role in understanding the effect of aging on early failure behaviors as its decomposition at intermediate temperatures leads to early gas generation and contributes to first venting.

1.1.4 Evolution of Li-ion Battery Failures

LIB failures can originate from different types of related battery abuse, including mechanical (e.g. penetration), electrical (e.g. short circuits), and thermal (e.g. overheating) abuse that can ultimately lead to thermal runaway. The severity of the consequences depends on other factors, including the battery system design, conditions of abuse, and state of the cell, but can include venting of toxic gas, smoke, fire, and explosion. The evolution of a LIB failure, including the exothermic reactions preceding thermal runaway is illustrated in Fig. 1.4.

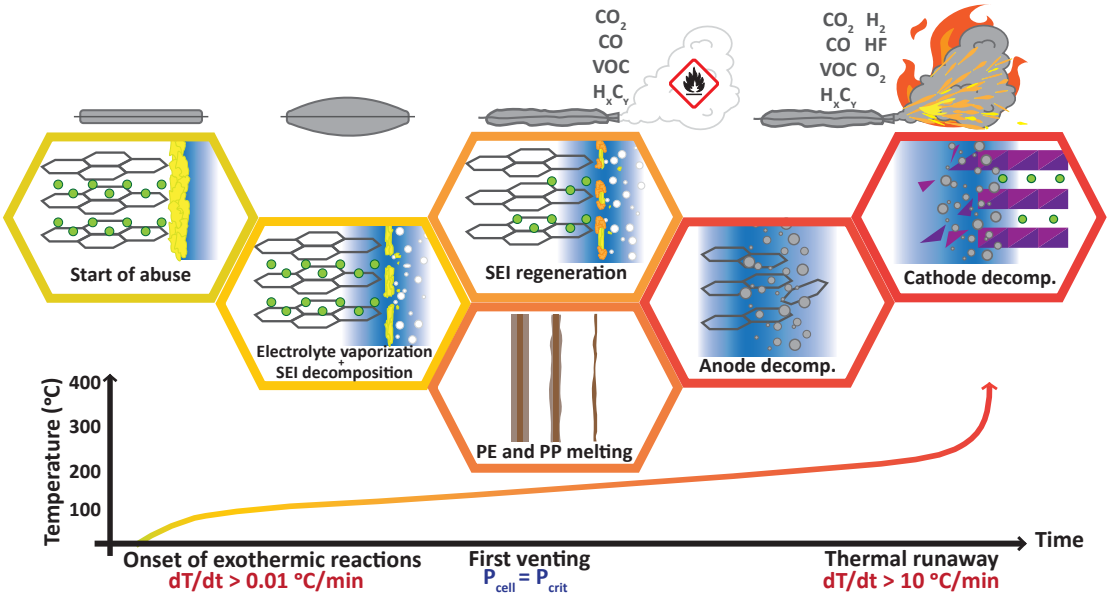


Figure 1.4: Evolution of exothermic reactions leading to thermal runaway

1.1.4.1 Early failure behaviors and onset of exothermic reactions

At intermediate temperatures between normal operating limits and before the onset of thermal runaway there are a few indicators of abnormal temperatures that the modeling work in this thesis will focus on. Active material thermal expansion and gas generation due to electrolyte vaporization occur, causing the cell to expand beyond the normal range. At this stage, the most reliable indicator, besides temperature, is expansion force for prismatic and pouch cells. Electrolyte vaporization causes a slight cooling effect and increases cell resistance, but these changes are more difficult to detect.

The first exothermic reaction is the decomposition of the solid-electrolyte interphase (SEI) on the negative electrode. From calorimetry testing, the onset temperature of SEI decomposition is typically about 80-120°C [24]. Similar to previous works, this thesis will assume that CO_2 is the primary gas generated during SEI decomposition, according to the following reaction that converts metastable $(CH_2OCO_2Li)_2$ to stable Li_2CO_3 [25, 26, 27, 28]

$$(CH_2OCO_2Li)_2 \rightarrow Li_2CO_3 + C_2H_4 + CO_2 + \frac{1}{2}O_2. \tag{1.1}$$

Continued SEI decomposition erodes the passivation layer, allowing Li to deintercalate and react with the electrolyte. At about 120-150°C, SEI decomposition and regeneration will simultaneously occur [24].

Simultaneously, the internal cell pressure will continue to increase due to gas generation from SEI decomposition and increased electrolyte vapor pressure. When the internal pressure

exceeds a critical venting pressure, the cell will vent hot, flammable vent gas [20, 29]. At this stage, the vent gas is mainly CO_2 but also includes other components such as CO, VOCs, and hydrocarbons that can be detected through gas concentration sensors [20]. This first venting event is considered to be a precursor to thermal runaway.

1.1.4.2 Onset of thermal runaway

As temperatures rise, several highly exothermic reactions can occur in quick succession, also known as thermal runaway (TR). When the cell temperature reaches the separator melting temperature, the plastic separator will shrink (about 130-170°C). The melting initially provides limited cooling and shuts down the separator pores, limiting the ionic current flow, but higher temperatures will eventually lead to separator collapse, inducing an ISC. At the electrodes, above 170°C, cathode decomposition begins, releasing oxygen. The actual onset temperature depends on the cathode chemistry and SOC, where metal oxides in the cathode, especially those containing Ni and Co, are more likely to be reduced at higher temperatures and stoichiometries [30, 31, 32, 33]. Above 250°C, the graphite negative electrode decomposes and the structure collapses, further generating heat. At these later stages, the TR vent gas is even more toxic and flammable, leading to jet flames, fire, and explosion.

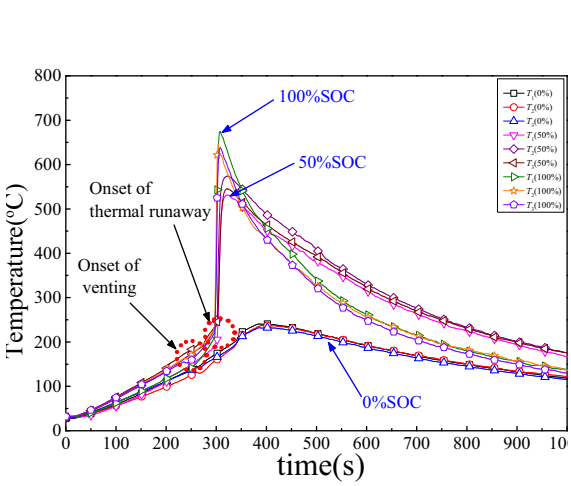
1.1.4.3 Thermal runaway propagation and system-level hazards

Thermal runaway can rapidly propagate to neighboring cells and modules through various modes. Heat transfer (e.g. conduction and radiation) can cause neighboring cells to overheat and fail, leading to sequential cell failure. Even with thermal barriers between cells, cell-to-cell conduction can still occur through their connected tabs and bus bars. Non-consecutive failure can also occur with the ignition of released flammable gases and arcing between exposed high voltage components, exacerbated by melting insulation [34]. Further fire and explosion hazards will develop if vent gases accumulate, depending on the flammability and explosion limits of the gas mixture, which may be ignited by hot particles and ejecta from cells undergoing TR.

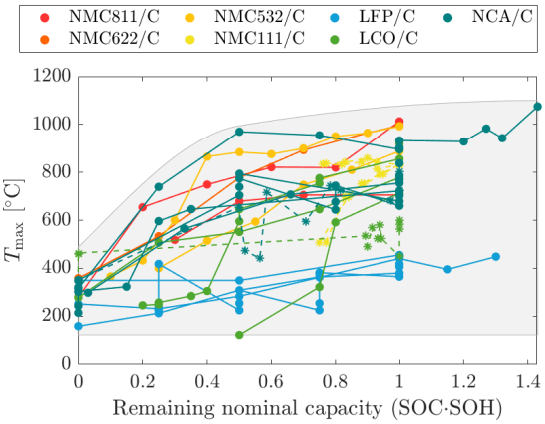
1.1.4.4 Impact of aging and state-of-charge

At the cell level, the state-of-charge (SOC) and aging pathway affect the thermal stability of the SEI and electrodes. In general, the safety of battery systems can be improved by discharging to a low SOC to reduce the risk of TR and mitigate the hazards if TR does occur. Previous studies show that the onset temperature of TR can increase with decreasing SOC, while the peak temperature during thermal runaway will decrease with decreasing SOC

[22, 35, 36, 37, 37, 38, 39], as shown in Fig. 1.5. This is due to reduced Ohmic heat generation from internal short circuit (ISC) after the separator melts and improved thermal stability and heat release from the electrode decomposition reactions [31, 32, 33, 40]. This means that at lower SOCs, especially below 50%, thermal runaway events will be more difficult to trigger. If thermal runaway occurs, the energy release is expected to be smaller compared to that at higher SOCs. Additionally, the total amounts of vent gas and of major asphyxiant and toxic gases (e.g., CO, HF, SO_2, NO_2, NO, and HCl) decrease with decreasing SOC [41, 42].



(a) Accelerated rate calorimetry testing of cells at different initial SOC illustrate different onset of TR temperature [39]



(b) Effect of remaining nominal capacity (SOC·SOH) and chemistry on peak temperature across 26 sets of cells over 21 overheating studies. Studies with "*" markers include SOH-dependence.

Figure 1.5: Effect of SOC and SOH on thermal runaway onset and peak temperatures

The aging pathway and state-of-health (SOH) also affect the peak temperature and onset temperatures of self-heating reactions and TR [43]. Previous works show that the presence of metallic lithium reduces the thermal stability of the SEI, which can develop from low-temperature and high-current cycling [22, 44, 45, 46]. On the other hand, high-temperature aging increases SEI thermal stability due to SEI thickening by impeding Li deintercalation and preventing or slowing the Li-electrolyte reaction for SEI regeneration [22, 44]. SEI growth and electrolyte dry-out can also increase the TR onset temperature and decrease the peak temperature due to decreased heat generation from the SEI regeneration reaction, ISC, and electrolyte decomposition [47].

To this end, one aim of this thesis is to demonstrate the potential of a discharge-based mitigation strategy to bring LIBs down to low SOC. This would enable discharging energy over a wide range of time-constrained scenarios while being aware of the safety risks of fast

discharging during an emergency. In this case, using a model-based approach would allow the controller to adapt the constraints as the LIB degrades.

1.2 Dissertation Contributions and Organization

This dissertation develops reduced-order multiphysics models to simulate the electrical, thermal, gas generation, and expansion behaviors of LIB pouch cells under early failure conditions. These include high C-rate discharge and high temperatures like during external short circuits, with the goal to enable early detection with multi-modal sensor fusion and guide fast discharge strategies. Unlike previous models, which focus on normal operation, aging, or TR, these models extend conventional control-oriented models to capture early failure behaviors and demonstrate their use for control and detection. The key contributions are summarized as follows.

In Chapter 2, an electro-thermo-mechanical model is developed by adapting an equivalent circuit model (EqCM) parameterized during normal operating conditions for high C-rate discharge. The EqCM is coupled with a zero-dimensional thermal model and a pouch venting model to account for the bulk temperature rise and expansion force during an electrical short circuit (ESC). A mechanical pouch venting model is derived that captures the two-stage cell expansion pressure from active material expansion and gas generation. With the coupled model, a model predictive control problem is defined to rapidly discharge the cell while avoiding venting, using constraints on voltage, temperature, and pressure. The simulation results show that incorporating pressure constraints and a long prediction horizon enables the controller to discharge the cell as quickly as when only the temperature limit is raised to 80 °C, but can also prevent first venting, which avoids additional fire hazards.

Chapter 3 focuses on upgrading the electrical submodel in the first multiphysics modeling configuration to a Single Particle Model with Electrolyte (SPMe), which is a reduced-order, physics-based model. The SPMe was initially parameterized from a previous aging study but is extended here to capture the diffusion-limited discharge behavior observed during a hard ESC by adding concentration dependence to the diffusion parameters, which were parameterized from data measured under normal operation. With minimal modifications, the SPMe can capture the current and voltage decay observed during ESC experiments across cells undergoing an ESC with different initial SOC. When coupled with parameterized thermal and pouch cell venting models, the combined model can also predict whether a cell will generate gas and vent under different initial SOC conditions.

In Chapter 4, a global sensitivity analysis is conducted on the pouch cell venting model to identify key parameters that influence cell expansion across temperature and age, which were

parameters related to preload, SEI decomposition, and thermal dependence of foam stiffness. By exercising the model across the key parameters, we also identified potential long-term challenges for expansion force-based algorithms, such as reduced expansion observability with increased preload pressure and the influence of temperature-dependent stiffness on detection sensitivity. The substantial variability in aging-related SEI decomposition highlights the importance of further research into modeling the relationships between cell degradation and safety.

Chapter 5 characterizes cell inhomogeneity and other degradation modes by augmenting a differential voltage analysis (DVA) algorithm with a modeled aged cell open circuit potential. We quantify inhomogeneity in cells aged under various temperature and C-rate conditions with up to 50% capacity loss. Our results show that accelerated degradation and inhomogeneity evolve differently in cells aged at cold and hot temperatures with similar cycling profiles. Furthermore, the degradation modes are used to bound estimates of SEI quantity in the venting model. Future exploration of the relationship between SOH diagnostic parameters and SEI thermal stability, quantity, and gas generation, can enable the development of robust BMS safety algorithms.

CHAPTER 2

Control-oriented Electro-thermo-mechanical Model with Fast Discharge Control Application

2.1 Introduction

In this chapter, an Li-ion battery (LIB) pouch cell model is developed that captures the multiphysics behavior during normal operation and external short circuit (ESC) conditions. The electro-thermal-mechanical model, illustrated in Fig. 2.1, will capture abnormal expansion and first venting as a result of gas generation, which depends on cell temperature. In the case of a high C-rate discharge or short circuit, these are driven by Ohmic heat generation from current and voltage losses.

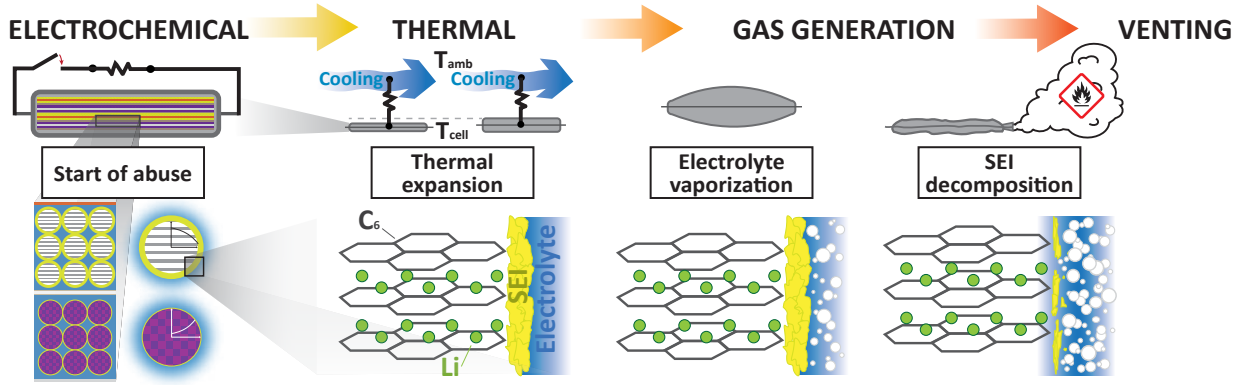


Figure 2.1: Modeling the progression of short circuit abuse and first venting hazard. An electrochemical model predicts the electrical behavior of a cell as it discharges. The corresponding Joule heating informs a thermal model that predicts the cell temperature. At high temperatures, gases are generated from electrolyte vaporization and SEI decomposition, building the internal cell pressure until the cell vents.

Previous studies developing low-dimensional electro-thermal models address high C-rate electrical behavior and temperature rise in cylindrical cells during ESCs but overlook gas generation and expansion. Smith et al. [48] developed and experimentally validated an equivalent circuit model (EqCM) to model the electrical behavior for a 16P module of cylindrical cells with positive temperature coefficient (PTC) devices that increase cell resistance at high temperatures to limit current. In this case, the maximum C-rate is only about 7.5 C, and the PTC devices tripped 12 seconds after the start of the short, dropping the current to C/5 [48]. Similarly, Chen et al. also developed an EqCM, which was then coupled to a 3D thermal model to capture the temperature distribution in a cylindrical cell [49]. In their study, the polarization resistance was modeled as an empirically-fitted function of SOC and temperature using test data from 30 different ESC test conditions to accurately model the electrical and thermal behavior. These cells included current interrupt devices that disconnected the circuit when the cell vented. However, battery systems also use other cell formats that may not have similar built-in safety devices, including pouch cells that can experience notably early gas generation, expansion, and venting.

This chapter will present ESC experimental results at different initial state-of-charage (SOC), explain each submodel (i.e. EqCM, lumped thermal, and pouch cell venting), and discuss the model modifications and parameter tuning needed to capture the bulk ESC behavior from a model that captures normal operating conditions. Then, the submodels will be cascaded to simulate the ESC of cells at different initial SOCs. Finally, a fast discharge controller will be developed using the model to demonstrate its application for control. The contributions of this chapter include

- Measuring pouch cell expansion force, which dictates the venting limit, for cells at multiple initial SOC conditions during an ESC
- Coupling an EqCM with a thermal and pouch cell venting model to capture the diffusion-limited electrical behavior, temperature rise, expansion, and vent timing for cells at high initial SOCs.
- Developing a nonlinear model predictive controller (NMPC) to safely and quickly discharge a fully charged cell while avoiding venting with temperature and pressure constraints.

Section 2.2 describes the ESC experiments and presents the results for cells tested at different initial SOCs. Sections 2.3-2.5 describe the EqCM, lumped thermal model, and pouch venting submodels and their parameterization. Section 2.6 integrates the submodels into a cascaded, multiphysics model and presents the results using parameters fitted for one

cell. Finally, Section 2.7 presents the constrained, fast discharge control application of the combined model.

2.2 External short circuit experiments

For the ESC experiments, four NMC 111/graphite pouch cells were used with 1.0 M $LiPF_6$ 3:7 (%vol) ethylene carbonate (EC) to ethyl methyl carbonate (EMC) electrolyte manufactured at the University of Michigan Battery Lab. The pouch cell dimensions are 130 mm $\times$ 89 mm $\times$ 5.5 mm. The nominal cell capacity was 5 Ah, but the cells calendar-aged at room temperature to about 4.6 Ah at the time of the experiment. The current is normalized by the latter capacity to calculate C-rate. The cells were externally short-circuited at 100%, 75%, and 50% initial SOC (SOC_0) with two cells at 100% SOC, denoted as 100A and 100B.

2.2.1 Experimental setup

The experimental setup is the same as that reported in Cai et al. [27] and is illustrated in Fig. 2.2. First, K-type thermocouples ($\pm$2.2°C) were placed on the surface of the cell at the center and at the edge between the tabs to measure the cell surface temperature. Appendix A provides more details about temperature measurements at the center and edge of the cell, but for this work, only the surface center temperature is considered. The pouch cell was then secured between two compressible, polyurethane foam sheets in a fixed-displacement fixture instrumented with an Omegadyne LC305-500 load cell to measure the expansion force. The cell tabs were reinforced with copper plates, then secured to the acrylic plate underneath the cell to ensure a reliable connection to the circuit and prevent contact between the tabs during the remaining setup and testing. The fixture with the cell was then placed in an acrylic box to contain any ejected electrolyte in case of venting, along with an NDIR CO_2 sensor. The entire box was then placed inside a fume hood for the experiment.

The cell was then connected in series with a Gigavac GV141BAB DC contactor (max contact resistance of 0.4 mΩ and insulation resistance of 100 MΩ) and a NUVX-LB-200-100 current shunt rated for 200 A at 100 mV using 4 AWG wires. The current shunt resistance has a 0.25% tolerance, corresponding to a 0.5 A error in measured current from the full-scale range. The cell terminal voltage was measured using a National Instrument SCXI-1102 module, which has an accuracy of $\pm$3.5 mV. The short circuit was initiated by supplying a 12 V signal to the contactor to close the circuit, and the current (I), terminal voltage (V_T), surface temperature (T), expansion force (F), and vent gas CO_2 concentration measurements

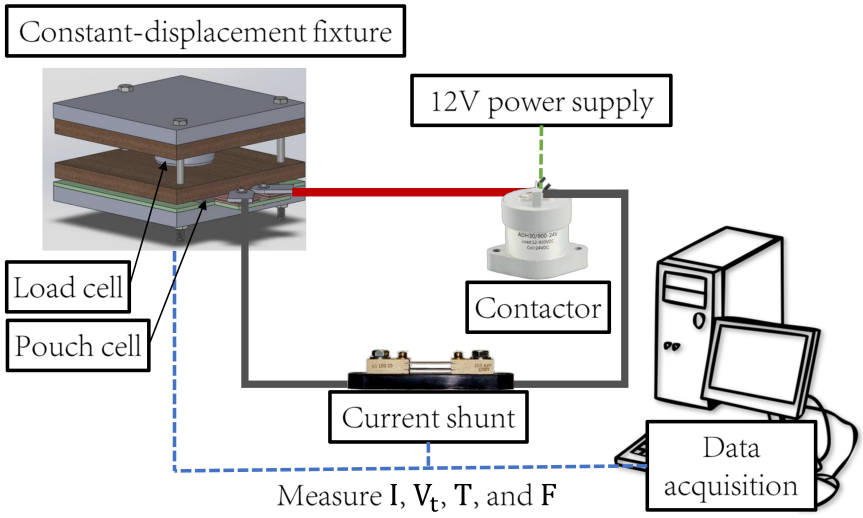


Figure 2.2: Diagram of external short circuit setup. Red and grey lines indicate positive and negative terminal wire connections, respectively, for the main circuit. Measurement signals from the instrumented fixture, cell, and gas sensor including current (I), terminal voltage (V_T), cell temperature (T), and expansion force (F).

were all recorded at a 10 Hz sampling rate. The circuit was opened again about 15 minutes after the ESC was initiated, ending the test.

Before the ESC testing, Cell 100A underwent a C/10 discharge to approximate an open-circuit voltage (OCV) curve and a 2 C discharge pulse test consisting of a 2-minute 2 C discharge pulse followed by a 5-minute rest, repeated until the minimum voltage condition (<3.0 V) was reached. Before each test, the cell was fully charged to 4.2 V with a 1 C constant-current, constant-voltage (CCCV) procedure. The pre-test characterization data were used to tune the EqCM at normal operating conditions. The OCV data was used to determine the initial ESC voltage and corresponding initial SOC (SOC_0) for the other cells, calculated via voltage inversion. While C/10 may be faster than what is typically used to characterize the OCV (e.g. C/20 or C/100), accounting for Ohmic resistance, the OCV error is expected to be within 5 mV. All pre-test characterization was performed on the BioLogic BCS-815 cycler.

2.2.2 Experimental results

The experimental results of the ESC are shown in Fig. 2.3, where the data are plotted in linear time and logarithmic time to highlight the evolution of different physical ESC behaviors on different timescales. The current and voltage behavior was the most dynamic in the first two minutes of discharge, while the SOC, temperature, and expansion force evolved more slowly.

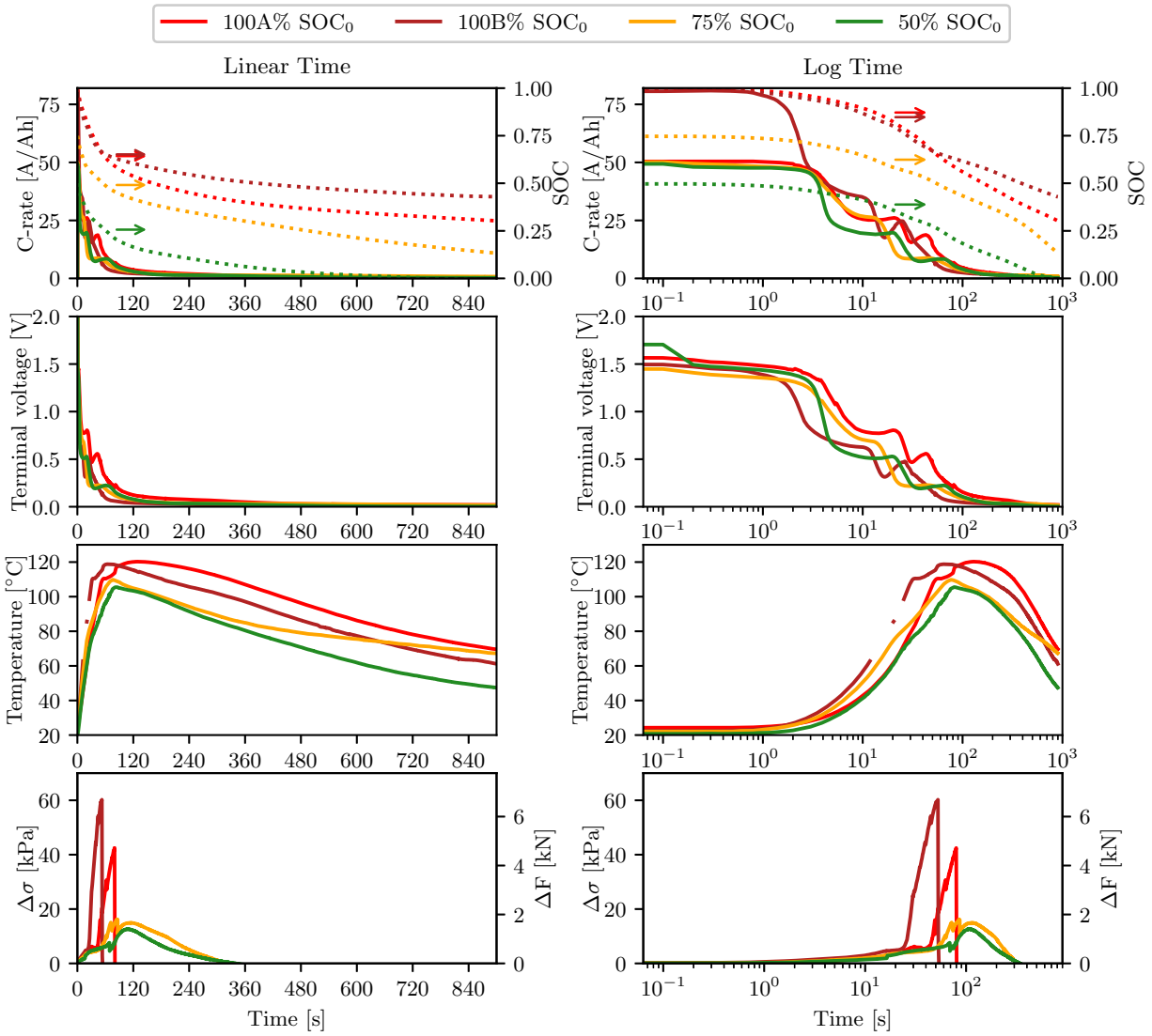


Figure 2.3: Experimental data for a 15-minute external short circuit. From top to bottom, these are measured cell current, voltage, center surface temperature, and compression stress from cell expansion, all plotted versus linear time (left) and log time (right).

When the short circuit was initiated, the current immediately peaks at about 50 C for all cells except for cell 100B, which peaked at 81 C, and the voltage drops to about 1.5 V. These signals can be seen more clearly in the log-time plots of Fig. 2.3. Within 2.5 s, the current drops by at least 20 C, and continues to drop with step-like behavior for the first minute, with the terminal voltage responding similarly. For all cells, the current decays to 10 C in the first minute and 1 C within 5-11 min.

SOC was calculated from the current through Coulomb counting from SOC_0. Accounting for the 0.5 A current measurement error over the 15-min ESC, the maximum error in SOC

is ±3% SOC. At the end of the experiment, the depth-of-discharge (DOD) for each cell was ≥50% SOC, where about 25% SOC was discharged in the first minute before slowing significantly as the current continued to decay. The center surface temperature peaked within the first two minutes with a maximum temperature between 106-120 °C, which increases with initial SOC.

Cell expansion during the ESC can be seen in the plot of change in compression stress in the fixture, denoted as $\Delta\sigma$, which illustrates the effects of gas generation, internal pressure increase, and venting. From the expansion force measured by the load cell ($\tilde{F}$), the $\Delta\sigma$ is calculated as

$$\Delta\tilde{\sigma} = (\tilde{F} - \tilde{F}_0)/A \tag{2.1}$$

where $\tilde{F}_0$ is the initial force from the pre-load compression (10-14 N). The compression force from the fixture is applied to the top face of the cell stack, which has a surface area of A. For all cells, a two-stage expansion was observed, indicative of thermal expansion of active material followed by gas generation [27]. Only fully charged cells, Cell 100A and Cell 100B, vented after 80 s and 53 s, respectively, at different critical pressures. While the other cells experienced gas generation, the effect was reversible with no observable or measured gas leak through the CO_2 gas sensor. From visual and tactile inspection of Cells 50 and 75 after the tests, there were no noticeable signs of irreversible gas generation, suggesting that expansion and contraction were due to electrolyte vaporization and recondensation.

The important characteristics for the model to reproduce are summarized in Table 2.1, including the final SOC, DOD, maximum cell temperature, maximum expansion stress ($\Delta\sigma_{\max}$), and venting timing (t_{vent}) for all four cells.

Table 2.1: Summary of key metrics over the 15-min ESC.

Cell	SOC_0	SOC_f	DOD	T_{max} [°C]	$\Delta\sigma_{max}$ [kPa]	t_{vent} [s]
100A	1	0.30	0.70	120.3	42.5	79.8
100B	1	0.43	0.57	118.8	60.2	52.6
75	0.75	0.133	0.62	109.8	16.2	-
50	0.50	-0.01	0.51	105.6	12.6	-

2.2.3 Experimental limitations

There are a couple of experimental limitations to note. First, in the load cell fixture, the rapid change in expansion force caused the bottom plate to slip, resulting in small discontinuities in the force data as seen for all four cells in Fig. 2.3. The CO_2 gas sensor confirmed that the discontinuities are not due to venting or gas leakage from the pouch. Second, the raw

thermocouple data for Cell 100B had large spikes in temperature (>1100 °C) between 12-26 s, so those values were filtered out. This may have been due to a loose thermocouple connection. These issues can be addressed with slight design and procedural modifications in future experiments.

2.3 Electrical model

In modeling an external short circuit to predict behavior during a fast and safe cell discharge, predicting the final SOC is an important metric to evaluate effectiveness. An equivalent circuit model (EqCM) was chosen because of its simplicity, scalability, low number of parameters, and low computational complexity.

In the ESC electrical model shown in Fig. 2.4, a single RC EqCM is used. An additional constant series tabbing resistance term, R_{tab}, was included to account for additional contact resistance at the connection between the clips used for voltage measurement and the hardware-reinforced tabs. Because of this, the measured terminal voltage, V_T, includes the nominal single RC and the voltage drop across R_{tab}.

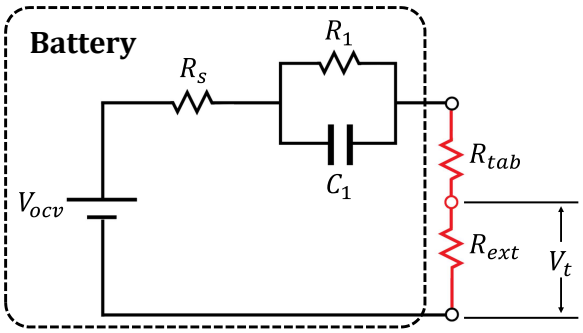


Figure 2.4: Battery EqCM with a single RC pair and additional series R_{tab}.

2.3.1 Nominal single RC model

The electrical behavior for the cell is described by two ordinary differential equations for the SOC and capacitor voltage, V_1,

$$\begin{bmatrix} \dot{\text{SOC}} \\ \dot{V}_1 \end{bmatrix} = \begin{bmatrix} 0 & 0 \\ 0 & -\frac{1}{R_1 C_1} \end{bmatrix} \begin{bmatrix} \text{SOC} \\ V_1 \end{bmatrix} + \begin{bmatrix} -\frac{1}{Q_{\text{nom}}} \\ \frac{1}{C_1} \end{bmatrix} I(t) \tag{2.2}$$

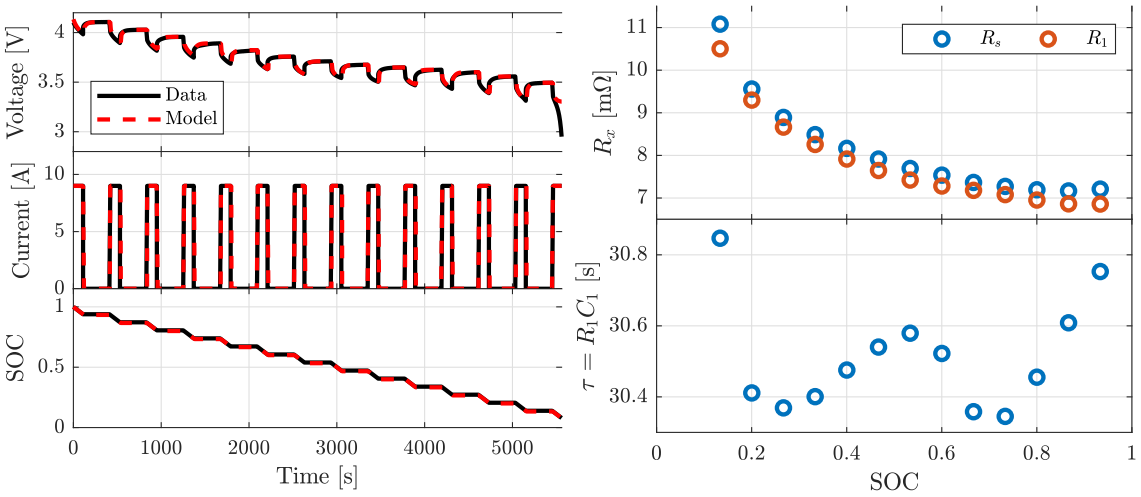
$$V_T(t) = V_{\text{OCV}}(\text{SOC}) - V_1 - (R_s + R_{\text{tab}})I(t), \tag{2.3}$$

where $V_T(t)$ is the cell terminal voltage, Q_{nom} is the capacity of the cell before the ESC, and $V_{\text{OCV}}(\text{SOC})$ is the open-circuit voltage. $I(t)$ is the short circuit current (Eq. 2.4), where $I > 0$ for discharge and is calculated as

$$I(t) = \frac{V_{\text{OCV}} - V_1}{R_{\text{ext}} + R_{\text{tab}} + R_s}. \tag{2.4}$$

Physically, the voltage drop across R_s can be interpreted as the internal cell resistance, for example, due to contact resistances, while V_1 across the RC pair can be interpreted as a voltage polarization due to charge transfer at the surface of the active material and lithium diffusion in the solid and electrolyte. For the system, the time constant is defined as $\tau = R_1 C_1$

The R_s, R_1, and C_1 parameters (Fig. 2.5b) were obtained through least-squares fitting of the 2C pulse test characterization data of the Cell 100A. The model is validated in Fig. 2.5a with a voltage root mean square error of 10 mV, which is comparable to other EqCMs [50].



(a) Nominal electrical model validation

(b) 2C pulse test characterization

Figure 2.5: Nominal EqCM simulation of 2C pulse testing and calculated parameters

2.3.2 Tab and external circuit resistances

Due to the variability expected from the leads connected to the cell during the experimental setup, the measured voltage and current are used to identify the resistance at the tabs,R_{tab}. In the model, R_{tab} was evaluated as the difference between the resistance calculated from the measured initial voltage drop ($V_{T,0}$), measured initial current peak (I_0), and expected initial $R_s(\text{SOC}_0)$. The external resistance, R_{ext}, was calculated with Ohm's law as the initial

voltage after the voltage drop divided by the initial current. These were calculated for each cell to match the initial voltage and current.

$$R_{\text{tab}} = \frac{1}{I_0}(V_{\text{OCV}}(\text{SOC}_0) - V_{T,0}) - R_s(\text{SOC}_0) \tag{2.5}$$

$$R_{\text{ext}} = \frac{V_T}{I_0} \tag{2.6}$$

After further analysis, the main metrics of interest (e.g. peak temperature and final SOC), were not sensitive to a 10% change in these parameters in the simulations, so the set of R_{ext} and R_{tab} obtained for Cell 100A was also used in the other initial SOC simulations.

2.3.3 Scaling of the nominal RC parameter functions

At abnormally high temperatures and C-rates observed in an external short, two competing factors affect diffusion, namely improved reaction kinetics and mass transport limitations, respectively. Looking at other works that model more normal operating conditions, Arrhenius parameter dependencies are used to capture increased reaction kinetics at higher temperatures, which correspond to a decrease in R_1 and increase in C_1 [48, 50]. However, under external short conditions, the cell discharge behavior is dominated by mass transport limitations in electrolyte and solid diffusion from operating at high currents [51]. A linear scaling of the diffusion-related parameters was chosen as the simplest modification of the nominal model that represents the overall effect of the phenomenon.

To capture the measured current and voltage decay from the external short circuit, the time constant, R_1C_1, needs to be increased, which is done by scaling R_1 and C_1 by constants α and β, respectively, where $R_1(\text{SOC})$ and $C_1(\text{SOC})$ are the curves used in the model and $\tilde{R}_1(\text{SOC})$ and $\tilde{C}_1(\text{SOC})$ are the original parameters from pulse test characterization.

$$R_1 = \alpha\tilde{R}_1(\text{SOC}) \tag{2.7}$$

$$C_1 = \beta\tilde{C}_1(\text{SOC}) \tag{2.8}$$

The parameterization for α and β is formulated as a constrained optimization problem (Eq. 2.9). The objective function was designed to reflect the goals of the model, which are to predict the final SOC and peak temperature. Therefore, penalties for SOC and cell

temperature error were included in addition to the current. The objective function is then

$$\begin{aligned} \underset{\alpha,\beta}{\arg\min} \quad J = \frac{||\hat{I} - I||_2}{I_{\max}} + \frac{||\hat{\mathrm{SOC}} - \mathrm{SOC}||_2}{\Delta \mathrm{SOC}} + \frac{||\hat{T} - T||_2}{\Delta T}, \\ \text{subject to} \quad 0.1 < \alpha < 1000 \\ 0.001 < \beta < 1 \end{aligned} \tag{2.9}$$

where $\hat{I}$, $\hat{\mathrm{SOC}}$, and $\hat{T}$ are the simulated current, SOC, and temperature, respectively, for the first ten minutes of the ESC. The thermal model used to simulate the cell temperature will be presented in the following section. From the data, $I_{\max}$ is the maximum measured current, ΔSOC is the total change in SOC during discharge ($\mathrm{SOC}_{\max}$-$\mathrm{SOC}_{\min}$), and ΔT is the total change in measured cell center temperature ($T_{\max} - T_{\min}$). For the first ten minutes of the ESC of Cell 100A, these are 232 A (50 C), 0.65 (65% SOC), and 96 °C, respectively. The optimization problem was solved using the MATLAB functions `multistart` with 20 local solvers and `fmincon` with the interior-point algorithm and an optimality tolerance of 1e-6. The bounds on α and β were chosen based on a sweep of the parameters between $\alpha \in [10, 1000]$ and $\beta \in [0.1, 1000]$ for the objective function J (Eq. 2.9), where a region near the minimum was identified. The sweep suggested that the problem is locally convex, but more analysis is needed to prove this.

For the fully-charged cell, α and β were fitted to be 64.53 and 0.48, respectively, ultimately increasing the time constant by a factor of 31 from 30.5 s to 946 s (about 16 minutes). A summary of the electrical parameters used in the subsequent simulations for all cells are provided in Table 2.2.

Table 2.2: Summary of electrical model parameters from Cell 100A

Parameter	Value	Unit	Description	Source
Q	4.6	Ah	Cell capacity	Measured
R_{ext}	6.7	mΩ	External resistance	Eq. 2.6
R_{tab}	3.7	mΩ	Tabbing resistance	Eq. 2.5
α	64.53	-	R_1(SOC) scalar	Fitted
β	0.48	-	C_1(SOC) scalar	Fitted

2.3.4 Equivalent circuit model results

ESCs were simulated for each initial SOC condition. The results compared to the data can be seen in Figure 2.6. In application, the initial SOC may not be known or measurable; however, the results show that across relatively high initial SOCs, the same parameter set

and linear scalings on the diffusion-related parameters work well in predicting the final SOC after a 15-minute short circuit as seen in Table 2.3. Overall, for Cell 100A the model captures the intermediate current decay from a peak of 50 C down to below 1 C and similarly for the voltage decay from 1.6 V to 25 mV. The root-mean-squared errors (RMSE) for current and voltage are 5.8 C and 0.18 V, respectively. During the first two minutes, the absolute SOC error peaks due to the error in the predicted current, but decreases and ultimately underpredicts the final SOC by almost 10% SOC. Applying the same parameters to Cell 100B gives the same simulation results, but with larger errors.

Applying the same parameters to the 75% and 50% SOC_0 cells, the final SOC error was underpredicted by 6.6% SOC to be 14.3% SOC, whereas the calculated SOC from the measured current is 20.8%. Additional error metrics are provided in Table 2.3.

Table 2.3: Final SOC error and RMSE of current, voltage, and SOC

SOC_0 [%]	e_{SOC_f} [%]	$RMSE_I$ [A/Ah]	$RMSE_V$ [V]	$RMSE_{SOC}$ [%]
100(A)	-9.3	5.5	0.17	3.4
100(B)	-21.7	11.7	0.66	7.8
75	-6.4	5.5	0.21	7.0
50	-1.6	6.0	0.23	3.6

Because of the simplicity of the model, not all of the dynamics can be captured, especially during the first two minutes of the short circuit. The stepwise behavior of current and voltage during the first minute of discharge can be attributed to high-current mass transport limitations [51]. This is due to local Li depletion in the electrolyte and particle surface at very high currents, which can be modeled with a higher fidelity, physics-based electrochemical model [52]. However, a single RC EqCM does not have the mechanisms to describe this. Still, the error in the predicted SOC after a 15-minute ESC for most cells is at $< 10\%$ SOC. Recall that the current shunt has an accuracy of 0.25% full scale range, so over the duration of the ESC, this can account for up to 1.8% SOC error in SOC_f. While the RMSEs are relatively large for current and voltage compared to normal operation, much of this is from the first two minutes. Overall, the model is still able to capture the decay in current and voltage.

2.4 Thermal model

A single-state, lumped thermal model is used to describe the cell temperature

$$mC_p\frac{dT}{dt} = \dot{Q} - hA_{\text{cool}}(T - T_{\text{amb}}), \tag{2.10}$$

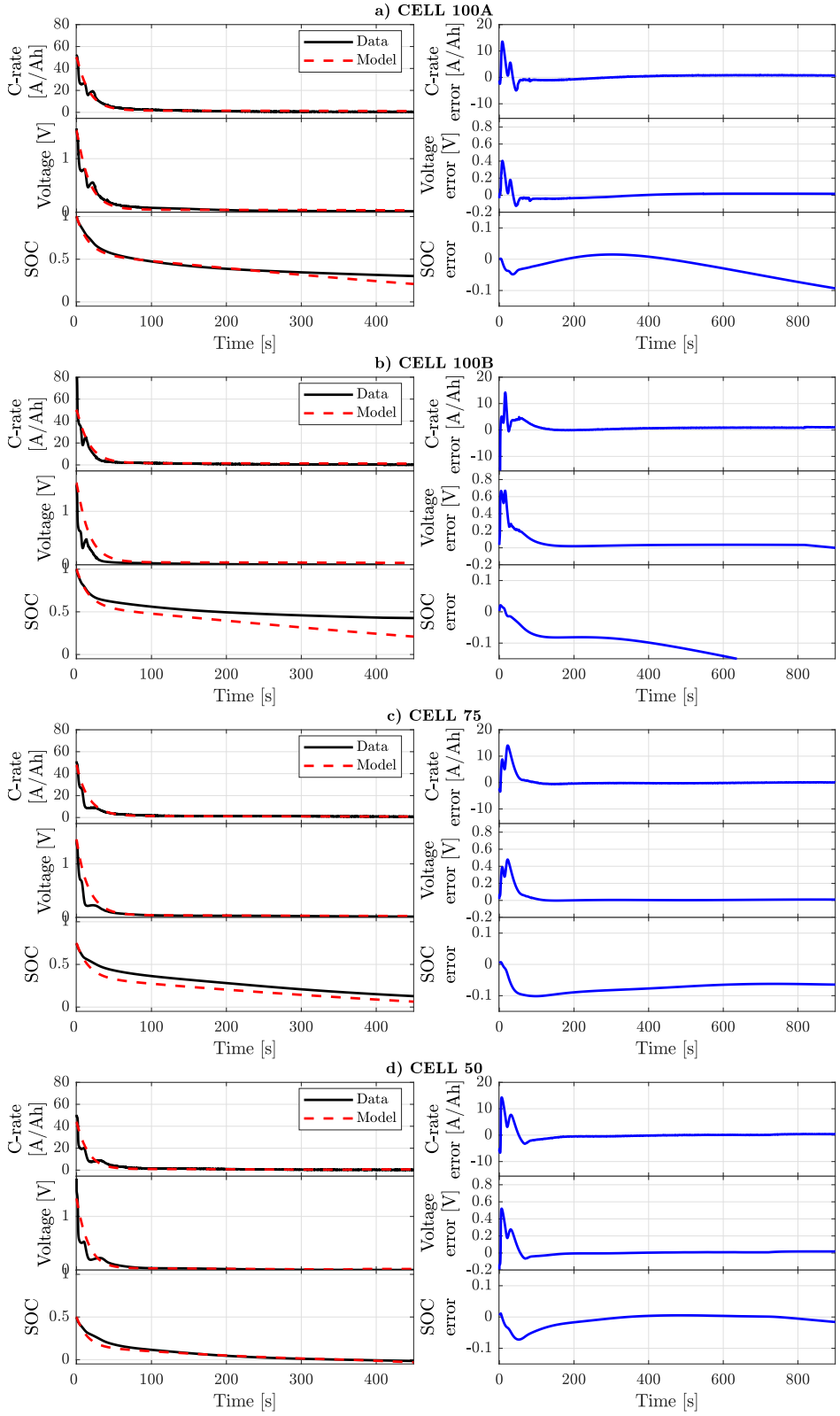


Figure 2.6: Comparison of ESC experimental data and electrical model results for Cell a) 100A, a) 100B b) 75, and c) 50.

where m is the mass of the cell; C_p is the effective specific heat capacity; h is the effective heat transfer coefficient; A_{cool} is the cell surface area available for cooling; and T_{amb} is the ambient temperature. The cell temperature is T, which has an initial condition of $T_0 = T_{\text{amb}}$. The input of the model is the total heat generation, $\dot{Q}$.

The total heat generation is calculated as the sum of heat sources, including Ohmic heating, $\dot{Q}_{\text{ohm}}$, and SEI decomposition heating, $\dot{Q}_{\text{SEI}}$. Other decomposition reactions can also be included; however, in the temperature range of our experiments ($\leq$120 °C), the higher temperature decomposition reactions (e.g. anode, cathode, and electrolyte) are considered negligible. Then, $\dot{Q}$ is calculated as

$$\dot{Q} = \dot{Q}_{\text{ohm}} + \dot{Q}_{\text{SEI}}, \tag{2.11a}$$

$$\dot{Q}_{\text{ohm}} = I(V_{\text{OCV}} - V_T) = I^2(R_s + R_{\text{tab}}) + IV_1, \tag{2.11b}$$

$$\dot{Q}_{\text{SEI}} = -m_{\text{an}} h_{\text{SEI}} \dot{x}_{\text{SEI}}. \tag{2.11c}$$

where m_{an} is the mass of the anode; h_{SEI} is the enthalpy of SEI decomposition reaction; and $\dot{x}_{\text{SEI}}$ is the rate of SEI decomposition. These parameters are from [29, 40]. For controller development, $\dot{Q}_{\text{SEI}}$ is only included in the plant model for completeness, not in the controller model, because the total heat generated from the SEI decomposition reaction is small compared to the Ohmic heat generation in our model [40]. In the expected temperature range ($\leq$120 °C) with the coupling between temperature and SEI decomposition, the thermal model dynamics are still stable with a time constant of 451 s (7.5 minutes). The main concern from the SEI decomposition reaction is the gas generation driven by an Arrhenius-like reaction that can ultimately lead to venting.

2.4.1 Thermal model parameterization

In practice, the thermal model can be parameterized from data collected under normal conditions. However, in this case, because the ESC testing was done in a separate fixture from that used for the pre-test characterization, the data from the ESC was used to fit the thermal model parameters. Additionally, we assume that the heat generation from SEI decomposition, $\dot{Q}_{\text{SEI}}$, is negligible compared to the Ohmic heat generation, which previous work has also shown [40, 53]. Assuming the coupling is weak, the thermal model can be parameterized separately by using the calculated total heat generation from experimental data, $\dot{\tilde{Q}}$, as the model input, such that

$$\dot{\tilde{Q}} = \dot{\tilde{Q}}_{\text{ohm}} = \tilde{I}(\tilde{V}_{\text{OCV}}(\tilde{\text{SOC}}) - \tilde{V}_T), \tag{2.12}$$

where $\tilde{I}$ is the measured current, and $\tilde{V}_T$ is the measured terminal voltage. $\tilde{V}_{\mathrm{OCV}}(\tilde{\mathrm{SOC}}))$ is the open-circuit voltage from C/10 discharge characterization data as a function of estimated SOC, $\tilde{\mathrm{SOC}}$, calculated through Coulomb counting.

To parameterize the thermal model, we fit C_p and h. The following minimization problem was solved for Γ^{opt}, such that

$$\begin{aligned} \Gamma^{\mathrm{opt}} &= [\gamma_{c_p}^{\mathrm{opt}}, \gamma_h^{\mathrm{opt}}] \\ &= \arg\min_{\Gamma} \frac{1}{N} \sum_{i=1}^{N} \left(\tilde{T} - T(\dot{\tilde{Q}}_{\mathrm{ohm}}, \Gamma) \right)^2 \\ &\text{subject to: } 0.1 \leq \gamma_{c_p} \leq 10 \\ &\qquad\qquad 10 \leq \gamma_h \leq 50 \end{aligned} \tag{2.13}$$

where $\tilde{T}$ is the measured cell temperature, and N is the total number of measurements. The γ_h and γ_{c_p} are scalars such that $h = \gamma_h^{\mathrm{opt}}$ and $C_p = \gamma_{c_p}^{\mathrm{opt}} C_{p,0}$, respectively, where $C_{p,0}$ is the initial guess. The bounds for γ_h were chosen to be representative of natural convection with additional heat loss due to conduction to the fixture. The bounds for γ_{c_p} were chosen to allow a magnitude of change due to the competing influence of thermal insulation from the foam sheets and conductive heat transfer through the plates of the fixture.

While the lumped thermal model assumes a uniform temperature across the bulk of the cell, temperature measurements at the center and edge of the cell surface indicate a temperature gradient as large as 7 °C at the peak (see Appendix A). As a future consideration, this can be captured by using a two-dimensional thermal model; however, this can significantly increase the computational complexity for the thermal and venting models, depending on the resolution of the spatial discretization and how the coupling between the two models is considered for the 2D case.

2.4.2 Thermal model parameterization results

The center surface temperature is used as the measured cell temperature. For each cell, the effective heat transfer coefficient, h, and the effective specific heat capacity, C_p, were fitted by solving Eq. 2.13. To fit Cell 100B, the cell temperature data was linearly interpolated where data was missing. Using the fitted parameters, the simulation results shown in Fig. 2.7 represent the case where there is no error in current or voltage propagating from the EqCM. The values for h and C_p along with error metrics from the simulation results for each cell

are provided in Table 2.4.

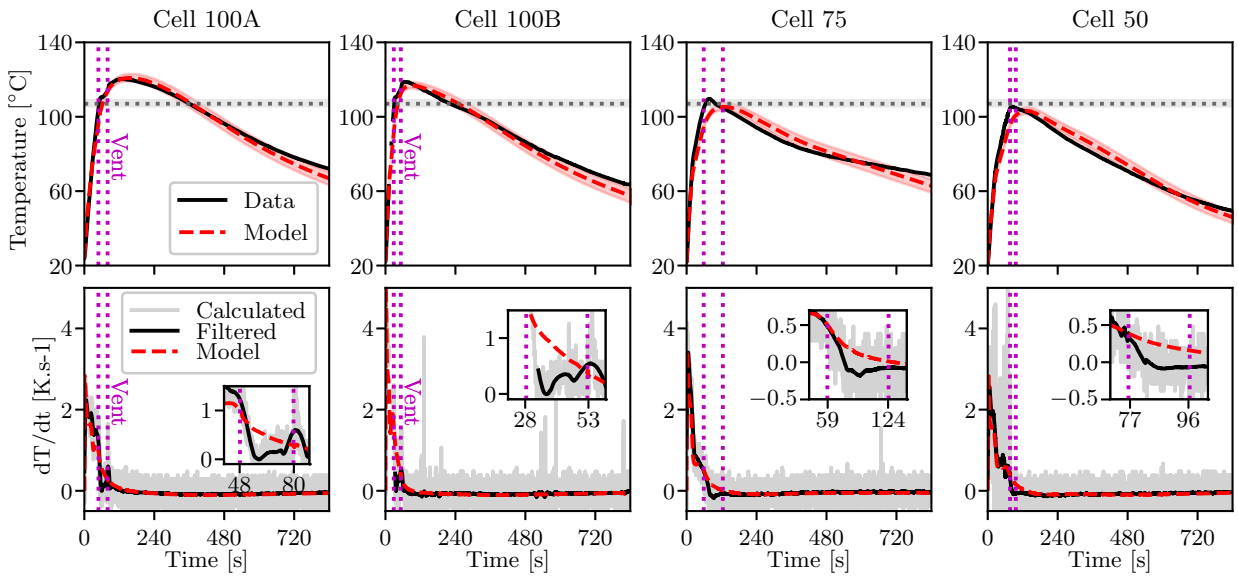


Figure 2.7: Thermal fit results for all cells for predicted temperature (top row) and rate of change of temperature (bottom row) using total heat generation calculated from data then filtered with $\pm(0.01\tilde{I} + 0.5)$ A current error. Electrolyte vaporization before venting occurs between the dotted lines (magenta), where the mismatch in $\frac{dT}{dt}$ trajectory due to vaporization cooling can be observed in the insets.

Across the cells, the fitted h is largely consistent, but the C_p for the fully-charged cells that vented is about 40% larger than that of the lower SOC cells. The variation in C_p may in part be due to unmodeled electrolyte vaporization cooling.

The RMSE is calculated for two periods, where $\text{RMSE}_{T<BP}$ is the temperature error before the cell first reaches the electrolyte boiling point of 107 °C for EMC [54] and RMSE_T is the temperature error for the full simulation. The RMSE_T is lower than $\text{RMSE}_{T<BP}$ which follows from the choice of minimizing the cost function for the full experiment. Overall, RMSE_T is fairly low, <5 °C, or about 4-6% of the total temperature rise.

Electrolyte vaporization can be observed by looking at the sudden drop in the rate of change of temperature that is not accounted for by Ohmic heating and occurs at the electrolyte boiling point. From the data, the calculated $\Delta\tilde{T}/\Delta t$ was filtered using a third-order Savitzky-Golay (SG) filter with a window of 50 samples (5 s) to reduce the impact of measurement noise. The cooling contribution from electrolyte vaporization ($\Delta T_{\text{H}_{\text{vap}}}$) can be approximated by integrating the error in dT/dt between the model and filtered data from when the cell temperature reaches the electrolyte boiling point until the cell either vents or cools back down below the boiling point. The approximation suggests that electrolyte

Table 2.4: Summary of fitted thermal model parameters and simulation errors. Errors include the before the boiling point is reached ($\text{RMSE}_{T<BP}$) and temperature RMSE for the 15-min simulation (RMSE_T); dT/dt error for the 15-min simulation ($\text{RMSE}_{\Delta T}$); peak temperature error ($\Delta T_{\max}$); and temperature error that can be accounted for by electrolyte vaporization (Δ $\text{T}_{\text{H}_{\text{vap}}}$).

Cell	h $[\frac{\text{W}}{\text{m}^2\text{K}}]$	C_p $[\frac{\text{J}}{\text{kgK}}]$	$\text{RMSE}_{T<BP}$ [°C]	RMSE_T [°C]	$\text{RMSE}_{\Delta T}$ [°C]	$\Delta T_{\max}$ [°C]	Δ $T_{\text{H}_{\text{vap}}}$ [°C]
100A	34.8	2733	4.03	2.86	0.13	0.78	7.51
100B	34.2	2345	6.38	3.90	0.09	-1.93	10.50
75	37.2	1937	7.55	4.32	0.13	-4.30	10.91
50	35.3	1987	6.25	3.60	0.13	-2.22	4.97

vaporization accounts for between 5-11 ° C of cooling, which is partially compensated for by increasing C_p and h, leading to the underprediction of temperature before the peak and at the end of the simulation in Fig. 2.7.

Additionally, 0.5 A error from the current shunt resistance is simulated as a measurement bias with an additional 1% scaling error to account for a temperature-dependent resistance change in the current shunt. For Cell 100A and Cell 100B, a current error of $\pm(0.01\tilde{I}+0.5)$ A corresponds to a range of <1.5 °C at the time of venting. For Cell 75 and Cell 50, this current error can cause the peak temperature to vary by < 1 °C. If the current and voltage predictions are accurate enough to capture the temperature rise within ±2.2° C, then the predicted temperature can reasonably tell.

2.5 Pouch first venting model

The mechanical first venting pouch cell model describes the cell expansion behavior as it transitions from normal to high-temperature operation before first venting under fixed displacement conditions. The following model is an extension of previous work by Cai et al. where the main modeling differences are in the additional considerations for cell stack compression from the applied force and temperature dependence of the foam sheets, which provide cushioning to accommodate the cell's deformation under pressure, the impacts of which are discussed later in the sensitivity study in Chapter 4 [27].

In the fixed displacement fixture illustrated in Figure 2.8, the distance between the top and bottom plates is fixed while the middle plate is free to move along the bolts to transfer the cell expansion force to the load cell. The initial preload compression force applied by the fixture is F_0. The fixture components are assumed to be rigid bodies and do not deform under load. However, small pouch cell deformation is allowed through the compliance provided by

the polyurethane foam sheets on either side of the cell.

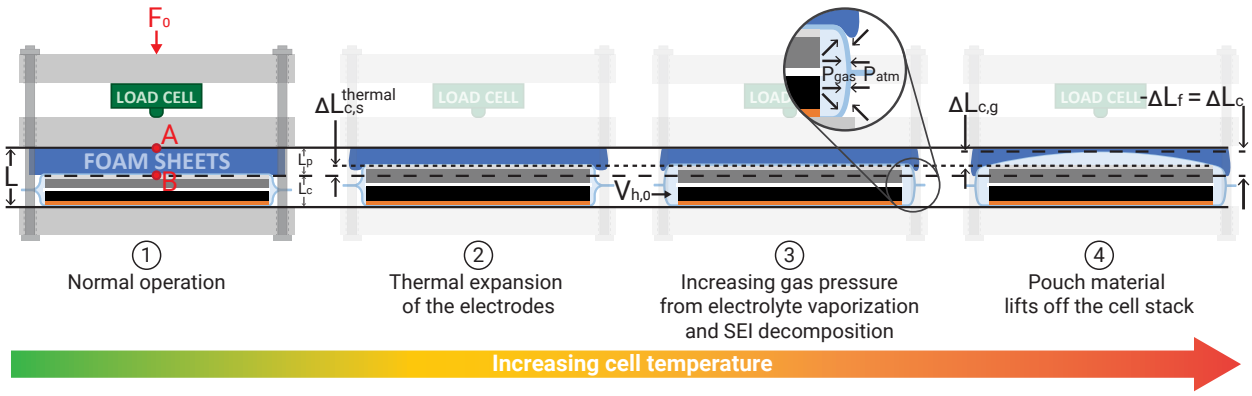


Figure 2.8: Evolution of cell expansion at high temperatures. All foam sheets are illustrated as a single, thick sheet for simplicity

Overall, the model captures the transition of cell expansion from normal operation to initial venting prior to TR. Under normal operation, the expansion of the solid electrode active material is due to changes in SOC and temperature. Solid expansion due to changes in SOC is not included in this work, but can be incorporated as an additional dependency. As the cell temperature increases beyond the normal operating range, the thermal expansion of the electrode ($\Delta L_{c,s}^{\text{thermal}}$) continues to grow. Meanwhile, increasing temperature increases internal gas pressure, P_{gas}, filling the initial headspace volume, $V_{h,0}$. The gas pressure in this work is modeled as the sum of electrolyte vaporization pressure and gas generation from SEI decomposition, which typically occurs at temperatures of about 80-120° C [25]. If the internal gas pressure exceeds the pressure applied to the solid cell stack, the pouch material will begin to lift off, leading to expansion due to gas generation ($\Delta L_{c,g}$). As the cell expands, the foam sheets contract to provide compliance in the fixed-displacement fixture. Venting occurs when the gas pressure exceeds the critical venting pressure, P_{crit}.

In this work, all the forces modeled are uniaxial in the through-plane, or $\hat{z}$-direction, aligned with the direction of the force measured by the load cell. The middle plate of the fixture is free to move along the bolts of the fixture, providing no additional forces. Within the pouch cell, each electrode layer is a thin film coated on a rigid current collector substrate, so the model assumes that there is no strain in the in-plane directions ($\epsilon_{xx} = \epsilon_{yy} = 0$) [55]. This implies that all cell solid expansion occurs in the $\hat{z}$-direction and that the surface area of the pouch cell in contact with the foam sheet, A, is constant. The model also assumes that there is no spatial gradient of stress in the in-plane direction due to the in-plane electrode asymmetry, meaning that the stress is uniformly applied over A [56]. The stress equilibrium

is then described by

$$\nabla \cdot \boldsymbol{\sigma} = \frac{\partial \sigma_{zz}}{\partial z} = 0, \tag{2.14}$$

where stress tensor is $\boldsymbol{\sigma}$ and σ_{zz} is the stress in the through-plane direction. When cell expansion occurs due to gas generation, these assumptions are maintained, so that the gas pressure is still applied over the original contact area A. Given these assumptions, we can simplify the stress tensor due to the applied force $\vec{F}$ as

$$\begin{aligned} \vec{F} &= F\hat{z} = A(\hat{z} \cdot \boldsymbol{\sigma}) \\ &= A\sigma_{zz} \end{aligned} \tag{2.15}$$

where $\vec{F}$ is the applied force vector in the $\hat{z}$-direction and F is its magnitude. Under these assumptions, the compressive stress on the pouch cell σ_c from the fixture due to cell expansion is equal to the stress in the z-direction σ_{zz}.

To model the cell expansion force with increasing temperature, we will model the change in cell expansion stress ($\Delta\sigma_c$) from normal operation where the cell temperature is equal to the ambient temperature, $T = T_{\text{amb}} = 25$ °C, and solve for $\Delta\sigma_c$ for the three main stages of expansion:

1. No gas generation
2. Gas generation *before* pouch lift-off
3. Gas generation *after* pouch lift-off

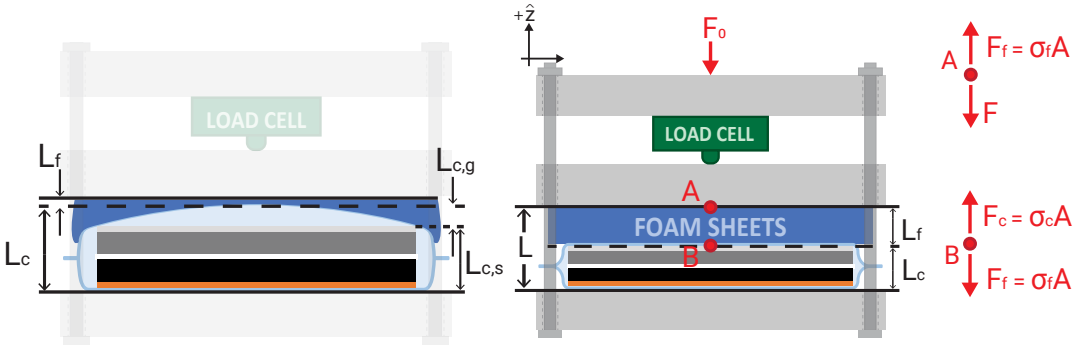
We assume that all forces act normally on the fixture plates and can be measured by the load cell. All changes in force, stress, and lengths refer to normal operation as the initial condition.

2.5.1 Geometric relationships

To set up the model, we first define terminology for the basic geometric and force balance relationships, illustrated in Fig. 2.9. As illustrated in Fig. 2.9a, the total fixed plate-to-plate distance, L, is assumed to be constant throughout the process and is the sum of the thickness of the foam sheets (L_f) and the thickness of the cell (L_c)

$$L = L_f + L_c \tag{2.16a}$$

$$L_c = L_{c,s} + L_{c,g} \tag{2.16b}$$



(a) Geometric definitions (b) General force balance

Figure 2.9: Diagram of force relationships and geometric constraints on the pouch cell in the fixed displacement fixture

where the cell solid stack thickness is $L_{c,s}$ and the cell thickness expansion due to gas generation is $L_{c,g}$. Additionally, for any length L_k for component $k \in \{f; c; c, s; c, g\}$, we can define

$$L_k = L_{k,0} + \Delta L_k \tag{2.17}$$

where $L_{k,0}$ is the initial thickness of component k under normal operation. Combining this with Eq. 2.16a and applying our fixed displacement assumption ($\Delta L = 0$), we can say that the expansion of the cell is equal to the compression of the foam

$$\Delta L_c = -\Delta L_f. \tag{2.18}$$

Through Eq. 2.16b and 2.17 and assuming no initial gas generation ($L_{c,g,0} = 0$), we can relate the change in thickness due to the solid and gas components of the cell as

$$\begin{aligned} L_c &= L_{c,0} + \Delta L_c \\ &= L_{c,s,0} + (\Delta L_{c,s} + \Delta L_{c,g}) \end{aligned} \tag{2.19}$$

where the change in cell solid stack thickness can be further defined as the sum of the contributions from thermal expansion $\Delta L_{c,s}^{\text{thermal}}$, mechanical compression from the applied force $\Delta L_{c,s}^{\text{force}}$

$$\Delta L_{c,s} = \Delta L_{c,s}^{\text{thermal}} + \Delta L_{c,s}^{\text{SOC}} + \Delta L_{c,s}^{\text{force}}. \tag{2.20}$$

The expansion or contraction due to change in SOC ($\Delta L_{c,s}^{\text{SOC}}$) can be included, but is assumed to be negligible in this study. The cell volume expansion due to changes in temperature and

fixture compression force, respectively, are

$$\Delta L_{c,s}^{\text{thermal}} = \alpha \Delta T \tag{2.21a}$$

$$\Delta L_{c,s}^{\text{force}} = -\frac{L_{c,s}}{E_{c,s}} \Delta \sigma_{c,s} \tag{2.21b}$$

where $E_{c,s}$ is the effective Young's modulus of the cell. For a stack of cell components mechanically in series, this may be determined by the least stiff material in the stack, e.g., the separator.

2.5.2 Force balance

As illustrated in Fig. 2.9b, a simple force balance on either side of the foam sheets in the fixture will show that the measured fixture compression force, F, is proportional to the compressive stress on the foam sheets, $\sigma_{zz} = \sigma_f$, and equal to that of the cell expansion force such that

$$\begin{aligned} F &= -F_f = F_c \\ &= -\sigma_f A = \sigma_c A. \end{aligned} \tag{2.22}$$

The forces F_f and F_c are the applied forces to the foam and cell, respectively, and σ_f and σ_c are the respective compressive stresses. For any component k, the change in force can be related to the change in thickness through the Young's modulus

$$\begin{aligned} \Delta F &= F - F_0 \\ &= A \Delta \sigma_k = A(\sigma_k - \sigma_0) \\ &= -E_k A \frac{\Delta L_k}{L_{k,0}} \end{aligned} \tag{2.23}$$

where E_k is the Young's modulus of k; F_0 is the initial preload force with corresponding compression pressure σ_0. For convenience, the change in expansion stress for the cell can be expressed in terms of the Young's modulus and initial thickness of the foam sheets by combining Eq. 2.22 and 2.23

$$\Delta \sigma_c = \frac{E_f}{L_{f,0}} \Delta L_c, \tag{2.24}$$

where the only unknown is ΔL_c.

For the cell stack, the change in thickness can be expressed as a function of $\Delta \sigma_{c,s}$ by

combining Eq. 2.17 and 2.21 so that

$$\Delta L_{c,s} = \alpha \Delta T - \frac{\Delta \sigma_{c,s}}{E_c} \left(\frac{L_{c,s,0} + \alpha \Delta T}{1 + \frac{\Delta \sigma_{c,s}}{E_c}} \right), \tag{2.25}$$

where the first and second terms represent the contributions from thermal expansion and contraction from the fixture compression force, respectively.

Finally, using Eqs. 2.25 and 2.16b, we have a general equation for $\Delta \sigma_c$

$$\Delta \sigma_c = \frac{E_f}{L_{f,0}} \left[\alpha \Delta T - \frac{\Delta \sigma_{c,s}}{E_c} \left(\frac{L_{c,s,0} + \alpha \Delta T}{1 + \frac{\Delta \sigma_{c,s}}{E_c}} \right) + \Delta L_{c,g} \right]. \tag{2.26}$$

to evaluate the different stages.

For this model, first venting is said to occur when $\sigma_{c,g} > P_{\text{crit}}$, where P_{crit} is the critical venting pressure, and t_{vent} is the time the vent occurs.

2.5.3 Stage 1: No gas generation

In the first stage, there is no gas generation, meaning that the solid cell stack carries the compression force of the fixture. When there is no gas generation, $\Delta L_{c,g} = 0$ and $\Delta \sigma_c = \Delta \sigma_{c,s}$, so Eq. 2.26 simplifies to a quadratic equation that can be solved analytically

$$0 = \Delta \sigma_c^2 + \left(E_c + \frac{L_{c,s,0}}{L_{f,0}} E_f \right) \Delta \sigma_c + \left(-\frac{E_f E_c}{L_{f,0}} \alpha \Delta T \right). \tag{2.27}$$

Note that dividing Eq. 2.27 by E_c and taking the limit as $E_c \to \infty$, assuming a rigid cell stack, recovers the equation from Cai et al. [27], where

$$\Delta \sigma_c = \frac{E_f}{L_{f,0}} \alpha \Delta T. \tag{2.28}$$

2.5.4 Stage 2: Gas generation *before* pouch lift-off

As temperatures increase, gas generation occurs. When the generated gas begins to fill the initial headspace volume as shown in the third stage in Fig. 2.8, the pouch material initially remains in contact with the cell stack, so $\Delta L_{c,g} = 0$ and Eq. 2.27 remain valid. We can use this case to show that the transition from observing solid expansion to expansion due to gas generation in the total cell expansion occurs when the change in gas pressure exceeds the applied pressure from solid expansion.

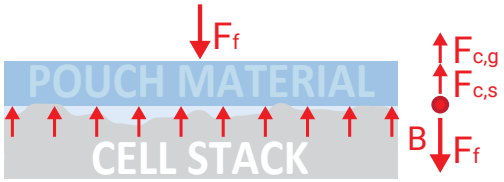


Figure 2.10: Gas pressure build-up at the surface between porous cell stack material and pouch materials sharing the load with the solid cell stack material.

When there's gas generation, the gas applies a force of

$$F_{c,g} = \gamma A \sigma_{c,g} = \gamma A (P_{\text{gas}} - P_{\text{atm}}) \tag{2.29}$$

on the pouch material over the area it's in contact with where γ is the fraction of the area carried by the gas. The gas pressure is P_{gas}, and P_{atm} is the atmospheric pressure.

Consider the case where the cell solid and gas share the load as illustrated in Fig. 2.10. The expansion force from the cell is then

$$F_c = F_{c,s} + F_{c,g} \tag{2.30}$$

where

$$F_{c,s} = (1-\gamma) A \sigma_{c,s} \tag{2.31}$$

$$F_{c,g} = \gamma A \sigma_{c,s} = \gamma A (P_{\text{gas}} - P_{\text{atm}}). \tag{2.32}$$

The transition between cell solid expansion and expansion due to gas occurs when $F_c = F_{c,g}$ or $F_{c,s} = 0$. Combined with Eqs. 2.23 and 2.29, this is the same as

$$\begin{aligned} F_{c,s} &= F_c - F_{c,g} = 0 \\ (1-\gamma)\sigma_{c,s} &= \sigma_c - \gamma \sigma_{c,g} \\ \sigma_{c,s} &= \sigma_{c,g} \\ \Delta\sigma_{c,s} &= \Delta\sigma_{c,g}, \end{aligned} \tag{2.33}$$

where $\Delta\sigma_{c,g} = P_{\text{gas}} - P_{\text{atm}} - \sigma_0$.

2.5.5 Stage 3: Cell expansion due to gas generation

Considering the expansion force applied by the gas as an internal force compressing two springs in series, i.e. the foam sheets and cell stack, Hooke's law can be applied to determine

the change in thickness of the foam sheets and cell stack, or equivalently the change in thickness of the gas layer according to Eq. 2.18 so that

$$\Delta L_{c,g} = -(\Delta L_f + \Delta L_{c,s}). \tag{2.34}$$

For a material with a spring constant of $\kappa_k = \frac{L_{k,0}}{E_k A}$ for $k \in \{f; c, s\}$, the effective spring constant is

$$\kappa_{\text{eff}} = \left(\frac{L_{f,0}}{E_f A} + \frac{L_{c,s,0}}{E_{c,s} A} \right)^{-1} \tag{2.35}$$

The cell expansion force is

$$\begin{aligned} F_c &= A\Delta\sigma_c = A\Delta\sigma_{c,g} \\ &= A(P_{\text{gas}} - P_{\text{atm}} - P_0). \end{aligned} \tag{2.36}$$

Using Hooke's law with Eq. 2.34-2.36, the thickness of the gas layer is

$$\Delta L_{c,g} = \max\left[\frac{A}{\kappa_{\text{eff}}} \left(P_{\text{gas}} - P_{\text{atm}} - \sigma_0 \right), 0 \right], \tag{2.37}$$

where taking the maximum ensures that $\Delta L_{c,g} = 0$ before expansion due to gas occurs.

The internal gas pressure, P_{gas}, is a sum of partial pressures from electrolyte decomposition and CO_2 generation from SEI decomposition. The latter is calculated through the ideal gas law making P_{gas} dependent on the increasing gas volume, V_g, which is in turn dependent on $\Delta L_{c,g}$, such that

$$\begin{aligned} P_{\text{gas}} &= \frac{n_{\text{CO}_2} RT}{V_g} + P_{\text{elyte}} \\ &= \frac{n_{\text{CO}_2} RT}{V_{h,0} + A\Delta L_{c,g}} + P_{\text{elyte}} \end{aligned} \tag{2.38}$$

where P_{elyte} is the electrolyte vaporization pressure; n_{CO_2} is the moles of CO_2 generated; and R is the universal gas constant.

Combining Eq. 2.37 and 2.38, the analytic solution is again a solution of a quadratic equation

$$\begin{aligned} 0 = {} & A\Delta L_{c,g}^2 + \\ & \left[V_{h,0} - \frac{A^2}{\kappa_{\text{eff}}} \left(P_{\text{elyte}} - P_{\text{atm}} - \sigma_0 \right) \right] \Delta L_{c,g} - \\ & \frac{A}{\kappa_{\text{eff}}} \left[n_{\text{CO}_2} RT + V_{h,0} (P_{\text{elyte}} - P_{\text{atm}} - \sigma_0) \right] \end{aligned} \tag{2.39}$$

After solving Eq. 2.39 with the quadratic formula for $\Delta L_{c,g}$, an analytic solution for $\Delta\sigma_c$ can be written using Eq. 2.37 and 2.38, where $\Delta\sigma_c(P_{\text{gas}}(V_{\text{gas}}(\Delta L_{c,g})))$.

The only remaining unknowns are P_{elyte} and n_{CO_2} in Eq.2.39 for calculating P_{gas}, which are summarized in the following subsections.

2.5.5.1 Gas generation from electrolyte vaporization

The electrolyte saturation vapor pressure (P_{elyte}) in Eq. 2.39 is modeled as a sum of ethylene carbonate (EC) and dimethyl carbonate (DMC) partial pressures calculated from their respective saturation pressures, $P_{\text{sat},i}$ for $i \in$ EC, DMC, using the Antoine equation:

$$P_{\text{elyte}} = y_{EC} P_{\text{sat,EC}} + y_{\text{DMC}} P_{\text{sat,DMC}} \tag{2.40a}$$

$$\log(P_{\text{elyte},i}) = A_i - \frac{B_i}{T + C_i}, \quad i \in \text{ EC, DMC}, \tag{2.40b}$$

where the component volume fraction is y_i, and the constants for the Antoine equation, A_i, B_i, and C_i, for each component are used from literature [25, 57].

2.5.5.2 Gas generation from SEI decomposition

The number of moles of CO_2 generated from SEI decomposition (n_{CO_2} in Eq.2.39) is modeled with an Arrhenius reaction rate, $\dot{x}_{\text{SEI}}$, can be captured by a self-limiting Arrhenius reaction as

$$\dot{x}_{\text{SEI}} = -A_{\text{SEI}} x_{\text{SEI}} \exp\left(-\frac{E_{a,\text{SEI}}}{k_b T}\right), \tag{2.41}$$

where x_{SEI} is the mole fraction of Li in the SEI to negative electrode active material (i.e. graphite C_6) [58, 59], and has an initial condition of $x_{\text{SEI},0}$ that depends on lithium consumption due to SEI growth from formation and aging [58, 60, 61]. The cell temperature is T, and k_b is Boltzmann's constant. The frequency factor and activation energy for SEI decomposition are A_{SEI} and $E_{a,\text{SEI}}$, respectively.

Finally, the number of moles of CO_2 produced is calculated through a mole balance of Eq. 1.1

$$n(\text{CO}_2) = \frac{1}{2}\left(\frac{m_{\text{an}}}{M_{C_6}}\right)(x_{\text{SEI},0} - x_{\text{SEI}}), \tag{2.42}$$

where M_{C_6} is the molar mass of the graphite C_6.

2.5.6 Temperature-dependence of foam stiffness

As an additional consideration to the model from Cai et al., the Young's modulus of the foam is modeled as a temperature-dependent parameter. Previous works characterized the compressive strength of polyurethane foams under a wide range of temperatures, demonstrating a general decreasing trend with increasing temperature [62]. Although these foams are significantly stronger than those used in these experiments, and because similar data are unavailable for comparable foams, the temperature dependence is modeled as another unknown parameter. As a first pass, the Young's modulus of the foam is modeled without accounting for the effect of pore collapse as

$$E_f = \max(E_{f,0} + k_{E_f}\Delta T, E_f^{\min}), \tag{2.43}$$

where $E_{f,0}$ is the nominal Young's modulus of the foam at 25 °C; $E_f^{\min}$ is the minimum value set at 10 kPa to avoid numerical issues when solving the model; and k_{E_f} is the thermal coefficient of stiffness of the foam sheet.

For the purposes of the simulations in Chapters 2-3, E_f is considered to be constant, but the impact of the temperature dependence will be explored in more detail in Chapter 4.

2.6 Electro-thermo-mechanical model validation

The results of the complete, cascaded electro-thermo-mechanical model can be seen in Fig. 2.11 for all cells, using the parameters fitted for Cell 100A. Individual contributions to heat generation and gas generation can also be examined and are presented in Fig. 2.12 for Cell 100A.

In the data, the initial fluctuations in current and voltage are characteristic of an external short circuit. These have been attributed to diffusion limitations in the electrolyte and solid particle surface [52]. The EqCM approximates the overall decay by increasing the time constant through the diffusion-related parameters, α and β in Eq. 2.2. The uncaptured current fluctuations also result a notable deviation in SOC, at least initially, especially for the cells that α and β were not parameterized for.

With the heat generation calculated from the modeled current and voltage, the initial temperature rise rate and peak temperature are captured by the model. The error is largest in the Cell 50 where the model underpredicts the peak temperature by 17 °C, which may be attributed in part to error propagation from the EqCM. Looking at the evolution of the heat generation components for Cell 100A, the Ohmic heat generation components from the series resistances, $\dot{Q}_{R_s} = I^2 R_s$ and $\dot{Q}_{R_{\text{tab}}} = I^2 R_{\text{tab}}$, dominate early in the ESC when current is large.

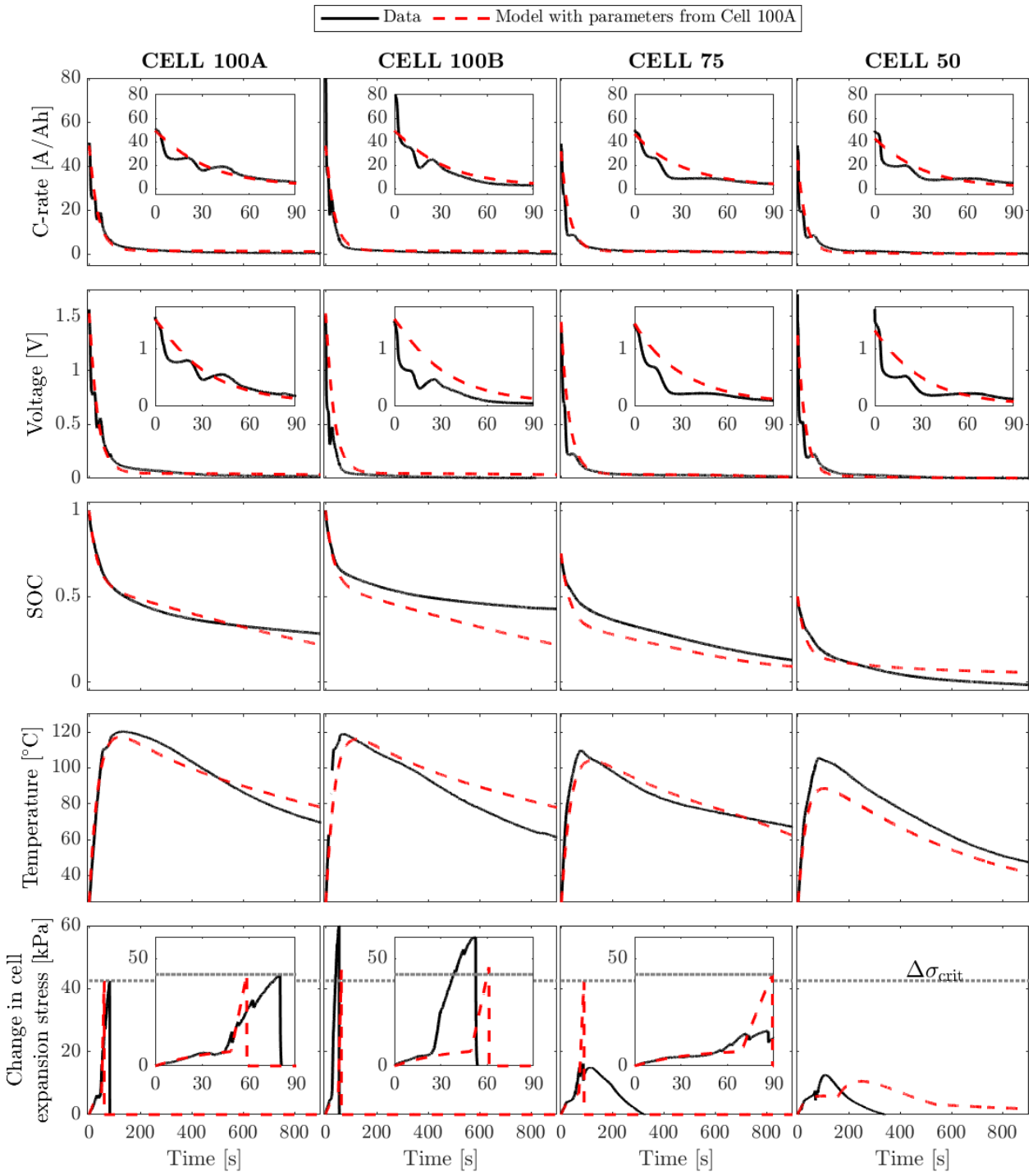
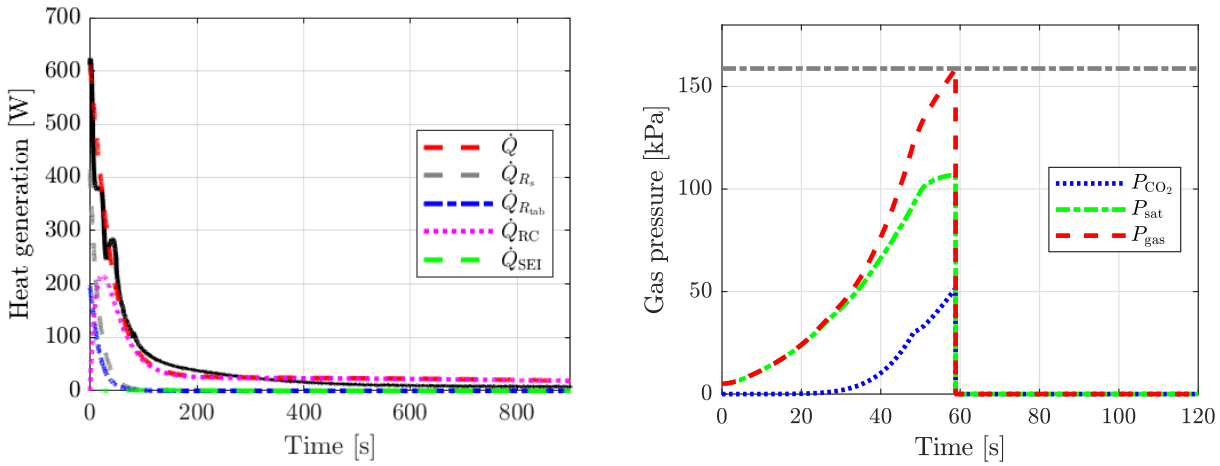


Figure 2.11: Combined EqCM-based multiphysics model simulation for a 15-min ESC with parameters from fitting Cell 100A. The parameters that were fitted for each cell were R_{esc} and R_{tab}. The h, C_p, α, and β fitted for Cell 100A were used to simulate all SOCs.

As concentration gradients build, so does the corresponding heat generation, $\dot{Q}_{RC} = IV_1$. To qualify the exclusion of the SEI decomposition heating in the controller, the modeled SEI decomposition heating in this case accounted for less than 1% of the total heat generation.

Using the modeled temperature as the input to the venting model, the combined model can largely predict when gas generation and venting will occur. The venting model captures the two-staged evolution of cell expansion. Initially, the expansion is due to the active material thermal expansion, which is well represented, but the model begins to deviate more significantly in the second stage with expansion due to gas generation. The combined model overpredicts gas generation, which causes it to predict venting for Cell 75, which did not vent in the experiment. This may be attributed in part to model mismatch, as the parameters of the SEI decomposition model are from the literature and are known to be affected by multiple factors, including aging condition [29, 44]. This also leads to more conservative predictions of vent timing, where the model predicts that fully charged cells would vent 20 s early and only 0.5 s late for Cells 100A and 100B, respectively. Looking at the gas generation components, the model suggests that the saturation pressure from electrolyte vaporization dominates the gas generation for a majority of the ESC. However, the model also shows that CO_2 from SEI decomposition grows more rapidly at high temperatures. At the time of venting, CO_2 from SEI decomposition accounts for a third of the total gas pressure. In the end, only 36% of the SEI decomposed according to the model. If either the critical vent pressure or the maximum temperature were higher, the fraction of CO_2 would likely increase, given the faster gas generation rate at high temperature.



(a) Heat generation by component

(b) Gas generation by component

Figure 2.12: Contributions to total a) heat generation and b) gas pressure for Cell 100A

2.7 Model predictive controller

The NMPC problem is set up as a static reference tracking problem, where the reference represents a nominal, fully-discharged cell, meaning a cell at ambient temperature with no SEI decomposition or gas generation. From the electro-thermo-mechanical model presented above, there are four states: SOC and V_1 from the electrical model; T from the thermal model; and x_{SEI} from the gas pressure model. The only input is current, I, and the output is the total cell expansion stress, σ_c, to monitor venting hazards. From the models defined above, the overall system input (u_k), output (y_k), and states (x_k) are

$$\begin{aligned} x_k &= \begin{bmatrix} \text{SOC} & V_1 & T & x_{\text{SEI}} \end{bmatrix}^T \\ u_k &= I \\ y_i &= \sigma_c. \end{aligned} \tag{2.44}$$

The cost function is described by

$$\begin{aligned} \min_{u,x,y,s,s_y} J_N = x_N^T \bar{V}_N x_N + \sum_{i=0}^{N-1} (& \frac{\Delta x_k^T \bar{Q} \Delta x_k}{||x_{\max}||^2} + \frac{u_k^T \bar{R} u_k}{||u_{\max}||^2} \\ & + \frac{\Delta y_k^T \bar{W} \Delta y_k}{||y_{\max}||^2} + \gamma_x s_k + \gamma_y s_{y,k}) \end{aligned}$$

subject to:

$$\begin{aligned} x_{k+1} &= f(x_k, u_k), && k = [0,N-1] \\ y_k &= f_2(x_k), && k = [1,N] \\ I_{\min} \leq I_k &\leq I_{\max}, && k = [0,N-1] \\ T_{\min} - 1s_k \leq T_k &\leq T_{\max} + 1s_k, && k = [1,N] \\ P_{\min} - 1s_{y,k} \leq P_k &\leq P_{\max} + 1s_{y,k}, && k = [0,N-1] \\ -s_k &\leq 0, && k = [1,N] \\ -s_{y,k} &\leq 0, && k = [1,N] \end{aligned} \tag{2.45}$$

where N is the prediction and control horizon. Deviations from a nominal, fully-discharged cell is represented by $\Delta x_i = x_i - x_{\text{ref}}$ and $\Delta y_i = y_i - y_{\text{ref}}$. Here, the reference state vector, $x_{\text{ref}} = \begin{bmatrix} 0 & 0 & T_{\text{amb}} & x_{\text{SEI},0} \end{bmatrix}^T$, and the reference output pressure, $y_{\text{ref}} = \sigma_0$, are equal to the initial, assuming that the battery discharge begins within normal operating conditions. The input current constraint is implemented as a hard constraint, which would reflect equipment limitations. In addition, soft constraints are placed on the temperature state and pressure

output to prevent venting. Exact penalization is used so that positive slack, or constraint violations, only occur when there is no feasible solution [63].

The slack on the states and output are s_k and s_y, respectively. The cost penalties on the state, input, and output are $\bar{Q}$, $\bar{R}$, and $\bar{W}$, respectively. Penalties on the state and output slacks for the soft constraints are γ_x and γ_y, respectively. The terminal cost penalty from solving the Riccati equation for the linearized system at x_{ref} is $\bar{V}_N$. The contribution of each penalty to the cost is normalized by the largest expected value.

For the equality constraints, $f(x_i, u_i)$ is the set of equations that describes the system dynamics (Eq. 2.2, 2.10, 2.41), while $f_2(x_i)$ is the output from the pressure model (Eq. 2.38).

The nonlinear control problem was then set up as a sequential quadratic programming (SQP) problem to solve for the primal variable increments and dual variables directly at each optimization iteration. The formulation was adapted from [64]. The optimization was solved iteratively using `quadprog` in Matlab. Because long prediction horizons are needed and many of the MPC matrices are sparse, MATLAB's sparse matrix multiplication was used to solve the SQP problem more efficiently. When solving, the maximum number of iterations was set to 10 and the tolerance to 1e-4. All submodels are simulated using a forward Euler approximation with a time step of Δt.

2.8 Fast discharge results and discussion

As a case study, an emergency discharge was simulated for a 4.6 Ah pouch cell using temperature and pressure constraints. For these simulations, the prediction and control horizons were chosen to be $N = 90$ with a sampling time $\Delta t = 1$ s. These were chosen to balance run time and controller performance. The same Δt was used to linearize and numerically solve the model with forward Euler approximations since the submodels have relatively slow time constants. The long horizon allowed the controller to better enforce the pressure constraint with some slack.

The simulation results can be seen in Fig. 2.13 for the first 20 minutes of discharge under three different constraint condition scenarios:

1. Nominal ($T_{\max} = 45$ °C)
2. High temperature constraint ($T_{\max}= 80$ °C)
3. High temperature and pressure constraints
   ($T_{\max} = 80$ °C and $P_{\max} = 79$ kPa)

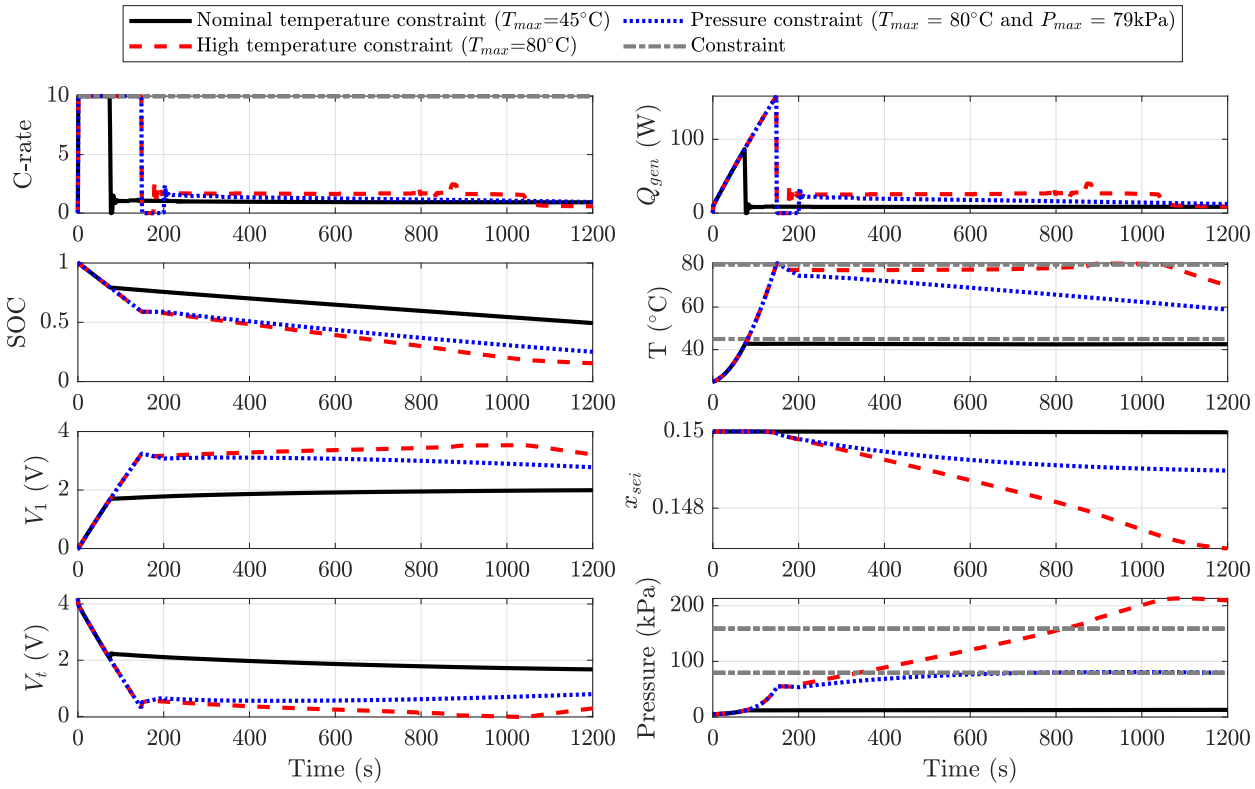


Figure 2.13: Simulated 20-minute emergency discharge results with the nominal operating temperature limit and extended temperature limit with and without temperature and pressure venting constraints.

For illustrative purposes, the maximum pressure is set to be half of the critical pressure reported in [27]. The maximum and minimum currents are 46 A (10 C) and 0 A, respectively.

The weighting matrices were calibrated through simulation with relative magnitudes to reflect the goals of the fast discharge. The penalties relating to the electrical and thermal behavior were first tuned to yield a controller that executed a fast discharge by following the temperature constraint (Scenarios 1 and 2). Then, $q_{x_{\text{SEI}}}$ and $\bar{W}$ were tuned such that the controller followed the pressure constraint (Scenario 3). The following weighting matrices were used for the simulations:

$$\begin{aligned}
\bar{R} &= 1\text{e} - 1 \\
\bar{Q} &= \text{diag}(q_z, q_{V_1}, q_T, q_{x_{\text{SEI}}}) \\
&= \begin{cases} \text{diag}(1\text{e}5, 1\text{e}3, 1\text{e}3, 0), & \text{not pressure-constrained} \\ \text{diag}(1\text{e}5, 1\text{e}3, 1\text{e}3, 1\text{e}6), & \text{pressure-constrained} \end{cases} \\
\bar{W} &= \begin{cases} 0, & \text{not pressure-constrained} \\ 1\text{e}4, & \text{pressure-constrained} \end{cases} \\
\gamma &= 1\text{e}3 \\
\gamma_y &= \begin{cases} 1\text{e} - 6, & \text{not pressure-constrained} \\ 1\text{e}3, & \text{pressure-constrained} \end{cases}
\end{aligned} \tag{2.46}$$

Initially, the large penalty on SOC error dictates the discharge behavior, incentivizing the controller to discharge at the maximum allowable C-rate until the temperature constraint is reached. In Scenario 1 with the representative nominal operating temperature limit, the control constraint is active for 74 s and discharges the cell down to 80% SOC before decreasing the current and discharging down to 60% in 13 minutes. In Scenarios 2 and 3, the control constraint was active for 149 s, and the higher temperature limit allowed the controller to discharge down to about 60% SOC before decreasing the current. In all cases, the controller eventually returns to discharging the cell with a current between 1 C and 2 C to obey the temperature or pressure constraint.

In Scenario 2, the maximum temperature constraint is increased to 80° C, which is at the lower end of the expected range for the onset of SEI decomposition. Although the discharge down to 60% SOC is four times faster, the cell reached the true critical pressure after 14 minutes, illustrating that increasing the temperature constraint while only considering temperature can unintentionally lead to venting, which introduces additional safety hazards.

In Scenario 3 with high x_{SEI} and pressure penalties and a soft output constraint on

pressure, the cell temperature peaked at 74° C before decaying due to the pressure constraint. The pressure constraint is slightly violated after 747 s and peaks at 1 kPa above the constraint before recovering. For reference, when $N = 45$, the run time is halved, but the pressure constraint was violated and continued to grow to 14 kPa above the constraint by the end of the 20-minute discharge. If this controller were to be used in real-time, a more conservative maximum pressure limit should be set below the expected critical pressure of the cell. To follow the pressure constraint, the controller needs to balance the pressure contributions from P_{sat} by decreasing temperature through current as SEI decomposes and P_{CO_2} increases. This suggests that additional cooling can be leveraged to discharge the cell faster.

Looking at the trade-off between increasing the temperature limit and discharge time, discharging a fully-charged cell under Scenarios 2 and 3 decreased the SOC to 60% in about 2.5 mins, while Scenario 1 took about 13 minutes. At the end of the 20-minute discharge, the cell SOCs were at 49%, 15%, and 25%SOC for Scenarios 1-3, respectively.

2.9 Summary

This work looked at how to extend an EqCM with parameters extracted from characterization testing within normal operating limits to capture high C-rate discharge behavior. This was coupled with a lumped thermal model to capture the peak temperature. As a first attempt, this works reasonably well in representing the bulk ESC current and voltage decay and the peak temperature. In the end, the combined model was able to predict venting for the fully-charged cells within 20 s of it occurring in the experiment. To more accurately capture the key safety metrics, greater accuracy in the modeled current may be needed by including additional dependencies, such as a C-rate dependency for the diffusion-related parameters. Finally, additional parameterization for the SEI decomposition reaction parameters should be considered to better reflect the gas generation.

The combined multiphysics model was applied to a fast discharge scenario to better understand how the normal operating limits can be pushed to respond to a detected thermal event in a battery system with an emergency discharge. We show that an NMPC scheme can be used to quickly discharge a cell without causing venting or introducing additional safety hazards if SEI decomposition and pressure are considered. These simulation results illustrate two main points. First, by increasing the maximum temperature limit, the discharge time down to a mid-SOC range, 60% SOC in this case, can be shortened significantly. Second, although increasing the temperature limit can provide a fast discharge, without considering the gas generation and internal cell pressure, the cell may vent and introduce flammable electrolyte to a hot environment. Although the discharge is slightly slower with an additional

pressure constraint, the cell did not vent, ultimately achieving a safe and fast discharge.

CHAPTER 3

Extending a Physics-based Electrochemical Model from Normal Operation to High C-rate Discharge and Venting

3.1 Introduction

Previous works have coupled an electrical equivalent circuit model (EqCM), but not a physics-based electrochemical model (ECM), with a thermal and venting model to capture Ohmic heat generation and venting during a short circuit. This includes the model presented in Chapter 2. However, the ESC model assumes that the cell discharge is mass-transport limited and cannot predict the transition between a hard ESC and normal operation, since these were the only tests the empirical EqCM was parameterized on. Alternatively, the EqCM can be parameterized using ESC data from an extensive design of experiments with more complex, empirical parameter functions; however, this can be resource intensive to develop [49]. A different approach is to use a more predictive physics-based model and extend the electrochemical model from normal to high C-rate operation using the same set of parameters.

For modeling ESCs, the high C-rates observed at low resistances can cause a cell to operate in a diffusion-limited regime, leading to numerical instability in physics-based models [52, 65]. Previous studies used a pseudo-2D physics-based, Doyle-Fuller-Newman (DFN) model by introducing a limiting current or concentration with a pre-exponential factor to the Butler-Volmer equation [52, 65]. Mao et al. [65] introduced a pre-exponential factor to the Butler-Volmer equation to incorporate a limiting current density, which Rheinfeld et al. [52] related to limiting concentrations and substantiated with experimental validation. For single-layer pouch cells (<60 mAh) with different negative electrodes and initial SOC under quasi-isothermal conditions (<1° C), they demonstrated that the DFN model described the observed changes in current magnitude and heat generation rate when a 0 V short was

applied, with peak currents reaching up to 828 C [66]. Although the DFN model can be accurate at high C-rates, its large number of states and stiff system equations make the model computationally demanding to solve [67]. Because these are too complex and impractical for online parameter tuning, detection, and control, we propose the use of a reduced-order ECM, such as the single-particle model with electrolyte (SPMe), to balance the trade-offs between model complexity and predictive capability [67].

In this work, we extend the work from the previous chapter by introducing an SPMe-based multiphysics model that can be parameterized using a limited number of experiments and address the challenges of previous empirical ESC modeling. The contributions of this work include

- Parameterizing concentration-dependent diffusion for an SPMe to replicate the step-like current and voltage behavior during diffusion-limited discharge
- Parameterizing the frequency factor for SEI decomposition using the mechanical venting model with expansion data
- Coupling a physics-based ECM with a thermal and venting model to capture the diffusion-limited electrical behavior, temperature rise, and vent timing for cells at high initial SOCs.

3.2 Multiphysics model

The simulations are implemented using the open-source Python Battery Mathematical Modeling framework (PyBaMM version 22.8) [68]. The submodels are nondimensionalized, and simulations are solved with the CasADi solver. Previously, Mohtat et al. [69] and Pannala et al. [60] developed a parameter set in PyBaMM to model reversible expansion from Li intercalation and irreversible expansion from degradation, respectively, for cells from the same manufacturing batch, which was also leveraged for this work to provide a nominal electrochemical model. An overview of the different submodels and their input-output relationships is provided in Fig. 3.1.

3.3 Single particle model with electrolyte

The single-particle model with electrolyte (SPMe) is a reduced-order electrochemical model of the DFN model that assumes a uniform current density across the electrode with electrolyte dynamics that improves the model fidelity under higher current operation compared

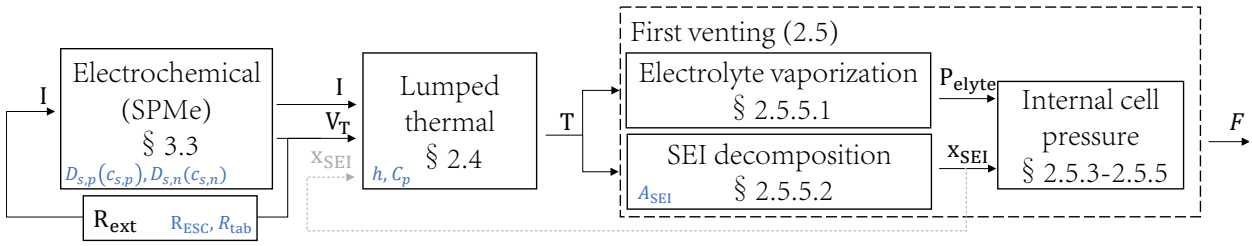


Figure 3.1: Diagram of submodel relationships and the parameters identified. SEI decomposition heating (grey) is not considered during parameterization but is included in the combined model. I is current; V_{T} is terminal voltage; x_{SEI} is the mole ratio of SEI to negative active material; P_{elyte} is electrolyte saturation pressure, and F is the cell expansion force. The parameters listed in blue are identified for the corresponding submodel.

to a single-particle model without electrolyte. At the particle surface, the current density, $j_{\mathrm{Li,k}}$, is the volume-averaged applied current for the negative and positive electrodes. Assuming each particle in an electrode behaves identically, each electrode is represented by a single particle. This model is typically used for currents <10 C [67, 70], but previous work has shown that the diffusion-limited discharge behavior can be captured by the reduced-order model as well [8]. The relevant findings are summarized here. A brief description of the SPMe model equations is provided in the supplementary material in Section B.1. More information about the asymptotic derivation of the SPMe and its implementation in PyBaMM can be found in Marquis et al 2019 [67] and Sulzer et al 2021 [68].

3.3.1 Solid diffusion coefficient parameterization

ESC modeling work by Rheinfeld et al. observed that accounting for the concentration-dependence of solid phase diffusion improved the model prediction accuracy during the initial transition phases using values from the literature which required half-cell testing [52, 71]. Instead, to parameterize the concentration dependence nondestructively, the diffusion coefficients for both electrodes were simultaneously fitted for each pulse of the 2 C pulse test, spanning the full range of SOC. A vector of scalars $\Gamma = [\gamma_{\mathrm{p}}, \gamma_{\mathrm{n}}]$ were fitted using the DFO-LS solver [72], where each γ_k is used to scale the nominal, constant electrode solid diffusion coefficient, $D_{\mathrm{s,k,0}}$ for $k \in n, p$, from the Mohtat et al. [69] parameter set in PyBaMM. The solid diffusion coefficient is then $D_{\mathrm{s,k}} = \gamma_{\mathrm{k}} D_{\mathrm{s,k,0}}$ for $\mathrm{k} \in \mathrm{n}, \mathrm{p}$. The following cost function was minimized to find Γ,

$$\begin{aligned}\Gamma^{\text{opt}} =&[\gamma_{\text{n}}^{\text{opt}}, \gamma_{\text{p}}^{\text{opt}}] \\ =&\arg\min_{\Gamma} \sum (\tilde{V}_T - V_{\text{T}}(\text{SOC}_0, \Gamma))^2 \\ &\text{subject to: } 0.1 \leq \Gamma \leq 10,\end{aligned} \tag{3.1}$$

where $\tilde{V}$ is the measured voltage during the relaxation period after the discharge pulse, and V_{T} is the modeled terminal voltage. At the start of each pulse, the initial SOC, SOC_0, was calculated from the data by Coulomb counting and was used to initialize the model assuming that the cell was at equilibrium. For the optimization, γ_n and γ_p were both initialized to 1 to give the nominal diffusion coefficient. Fig. 3.2 shows an example comparing the pulse simulation results with the nominal values and with the resulting fits.

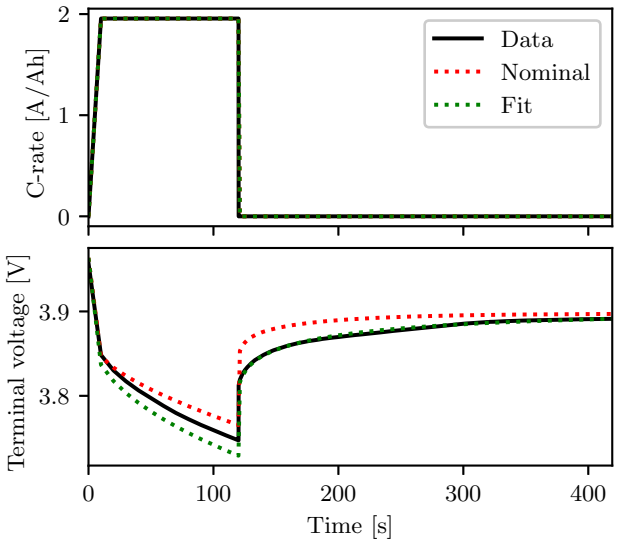


Figure 3.2: Example simulation from fitting electrode diffusion coefficients for a 2C pulse at $\text{SOC}_0 = 0.73$. Terminal voltage error is minimized during the rest period by solving Eq. 3.1.

The resulting γ_{k} values for all pulses were fitted with quadratic and linear polynomial fits for the positive and negative diffusion coefficients, respectively, as seen in Fig. 3.3 using the SOC at the end of the pulse. The voltage RMSE for each pulse ranged from 5 mV to 45 mV, except for the last pulse. At the 10% SOC pulse, the error was 136 mV, about three times larger than the next largest error, potentially due to insufficient rest duration or higher sensitivity to U_{eq} errors at low SOC [67]. In addition, γ_{n} at 38% and 45% SOC were fitted to be 9.86 and were considered outliers and omitted.

The full pulse test simulation in Fig. 3.4 shows that adding concentration-dependent solid-phase diffusion improved the nominal model accuracy, specifically in the mid-SOC range,

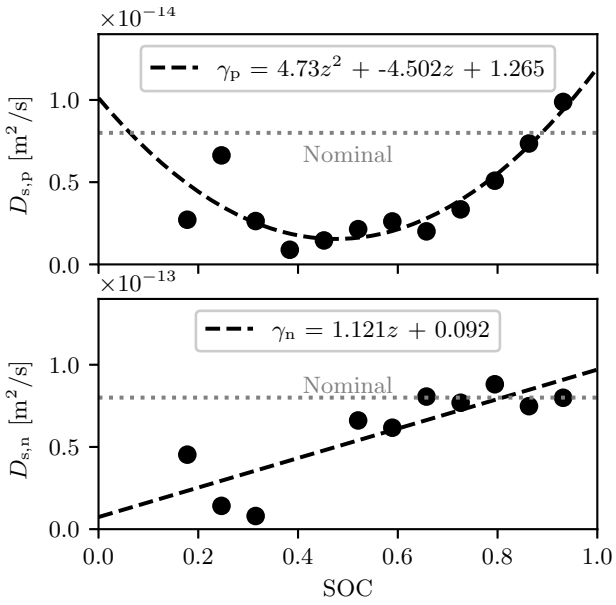


Figure 3.3: Diffusion coefficients fitted from the 2C pulse test where $D_{\mathrm{s,n}} = \gamma_n D_{\mathrm{s,n,0}}$ and $D_{\mathrm{s,p}} = \gamma_p D_{\mathrm{s,p,0}}$, where z is SOC.

and reduced the voltage RMSE by 45% from 23.1 mV to 12.6 mV. However, the model with concentration-dependent diffusion also reached the minimum voltage before it could complete the last pulse.

To incorporate concentration-dependent diffusion with the SPMe, SOC is converted to stoichiometry using

$$z = \frac{x_{\mathrm{Li}} - x_{\mathrm{Li,0}}}{x_{\mathrm{Li,100}} - x_{\mathrm{Li,0}}} = \frac{y_{\mathrm{Li,0}} - y_{\mathrm{Li}}}{y_{\mathrm{Li,0}} - y_{\mathrm{Li,100}}}, \tag{3.2}$$

where $x_{\mathrm{Li}} = c_{\mathrm{s,n}}/c_{\mathrm{s,n}}^{\mathrm{max}}$ in $\mathrm{Li}_{x_{\mathrm{Li}}}\mathrm{C}_6$ and $y_{\mathrm{Li}} = c_{\mathrm{s,p}}/c_{\mathrm{s,p}}^{\mathrm{max}}$ in $\mathrm{Li}_{y_{\mathrm{Li}}}\mathrm{N}_{0.33}\mathrm{M}_{0.33}\mathrm{C}_{0.33}\mathrm{O}_2$. The $x_{\mathrm{Li,0}}$ and $x_{\mathrm{Li,100}}$ correspond to the stoichiometry window in the negative electrode at 0% and 100% SOC, and similarly for $y_{\mathrm{Li,0}}$ and $y_{\mathrm{Li,100}}$ for the positive electrode. The concentration in the solid active material is $c_{\mathrm{s,k}}$ with a maximum of $c_{\mathrm{s,k}}^{\mathrm{max}}$ for k ∈ n,p.

3.3.2 Extending the nominal SPMe for an ESC

Under high C-rates like those seen in a low-resistance ESC, diffusion-limited transport can cause numerical stability issues in typical ECM. This occurs in the DFN when the solid particle surface concentration depletes or saturates (i.e. $c_{\mathrm{s,k}}^{\mathrm{surf}} \to 0, c_{\mathrm{s,k}}^{\mathrm{max}}$) or the electrolyte concentration depletes (i.e. $c_{\mathrm{e,k}} \to 0$) causing the exchange current density ($i_{0,\mathrm{k}}$) to approach 0 [52, 65].

$$i_{0,\mathrm{k}} = k_{0,\mathrm{k}}(c_{\mathrm{s,k}}^{\mathrm{surf}})^{1/2}(c_{\mathrm{s,k}}^{\mathrm{max}} - c_{\mathrm{s,k}}^{\mathrm{surf}})(c_{\mathrm{e,k}})^{1/2}, \quad \mathrm{k} \in \mathrm{n,p} \tag{3.3}$$

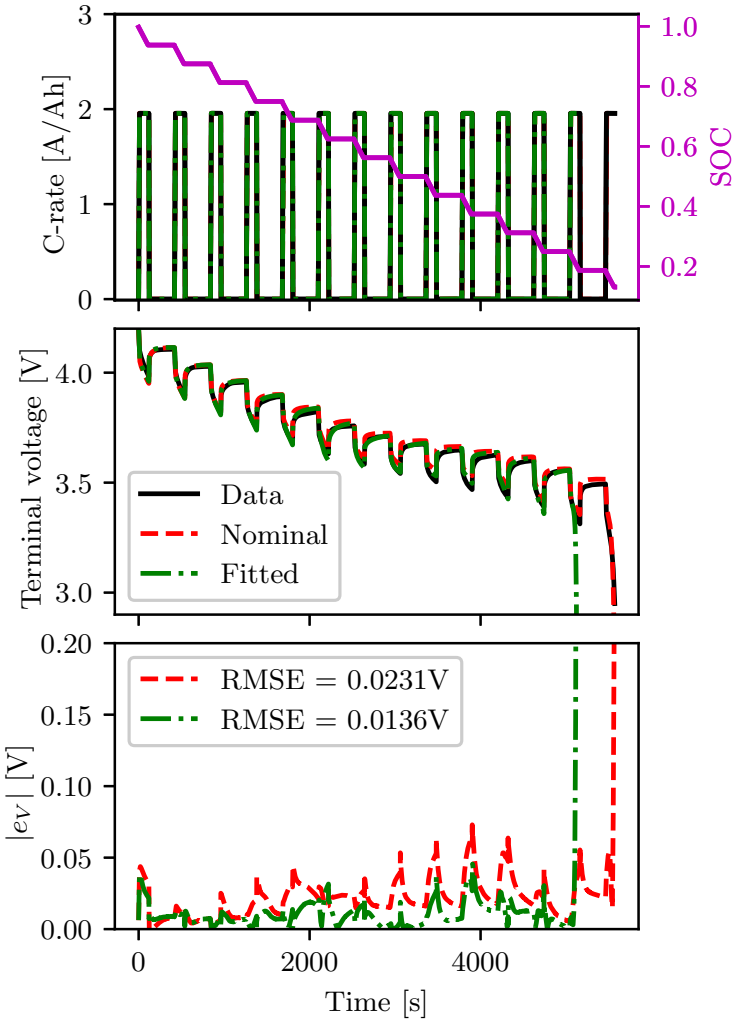


Figure 3.4: 2C pulse test validation with constant and fitted diffusion coefficients where e_V is the voltage error. Adapted from [8]

where $k_{0,\mathrm{k}}$ is the reaction rate constant. This can similarly be observed in the SPMe with the electrode-averaged exchange current density ($\bar{i}_{0,\mathrm{k}}$), defined as

$$\bar{i}_{0,\mathrm{n}} = \frac{1}{L_\mathrm{n}} \int_0^{L_\mathrm{n}} i_{0,\mathrm{n}} \mathrm{d}x, \quad \bar{i}_{0,\mathrm{p}} = \frac{1}{L_\mathrm{p}} \int_{L-L_\mathrm{p}}^{L} i_{0,\mathrm{p}} \mathrm{d}x, \tag{3.4}$$

where L is the cell thickness, and L_n and L_p are the negative and positive electrode thicknesses, respectively. When solving for the Butler-Volmer equation for the reaction overpotential ($\eta_{r,\mathrm{k}}$), $\eta_{r,\mathrm{k}}$ approaches $\pm\infty$,

$$\eta_{r,\mathrm{k}} = \frac{2RT}{F} \sinh^{-1}\left(\frac{i_\mathrm{k}}{\bar{i}_{0,\mathrm{k}}}\right) \quad \mathrm{k} \in \mathrm{n,p}. \tag{3.5}$$

Faraday's constant is F, and i_k is the volume-averaged current density. For more details about the model, a summary of the SPMe equations is provided in Section B.1 of the supplementary material.

The numerical stability issues have previously been addressed for the DFN by adding a pre-exponential factor, representing a limiting current density or limiting concentration [52, 65]. However, the model equations still need to be solved numerically and simultaneously which is computationally expensive.

Instead, we consider the analytical solution and follow the approach in PyBaMM to improve model robustness, namely using minimum and maximum operations to limit the concentrations such that $c_{\mathrm{s,k}} \in (\texttt{tol},\ 1\text{-}\texttt{tol})$ and $c_{\mathrm{e,k}} \in (\texttt{tol},\ \infty)$, where `tol` is the solver tolerance of 1E-8 [68]. This allows the SPMe equations to be solved under diffusion-limited discharge to retain the improvements in computational complexity of the reduced-order model.

The ESC is applied by using Ohm's law and adding an algebraic equation for constant resistance operation, such that

$$R_\mathrm{ext} = R_\mathrm{ESC} + R_\mathrm{tab} = \frac{V_T}{I}, \tag{3.6}$$

where R_ext is the total external circuit resistance; R_ESC is the external short circuit resistance, and R_tab is a series tabbing resistance between the cell current collectors and voltage measurement.

The R_ESC and R_tab for each cell were tuned to match the initial current and voltage drop. The tuned resistances and initial current and voltage errors are summarized in Table 3.1.

Table 3.1: Summary of fitted R_{ESC}, R_{tab}, initial current error (ΔI_0) and initial voltage error ($\Delta V_{\text{T},0}$) for each cell

Cell	R_{ESC} [mΩ]	R_{tab} [mΩ]	ΔI_0 [A]	$\Delta V_{\text{T},0}$ [V]
100A	6.7	6.8	-0.39	-0.016
100B	4.0	4.9	0.45	0.008
75	6.7	7.9	-0.49	-0.026
50	6.8	6.9	0.09	-0.016

3.3.3 Effect of concentration-dependent diffusion

Applying an ESC to the SPMe, concentration-dependent diffusion allows the model to better predict the initial current and voltage decay as illustrated by three simulation scenarios in Fig. 3.5:

1. Constant D_p and D_n
2. Concentration-dependent $D_{\text{p}}(c_{\text{s,p}})$
3. Concentration-dependent $D_{\text{p}}(c_{\text{s,p}})$ and $D_{\text{n}}(c_{\text{s,n}})$

Scenario 1 is a baseline with constant diffusion. When concentration-dependent diffusion is incorporated, the predicted timing and magnitude of the transition between induced current-voltage steps improve. From the current and voltage data, we also define three distinct transitions between the current-voltage steps and examine the cause of each using the SPMe. The corresponding spatial evolution of limiting concentrations during the first two transition points are show in Fig. 3.6.

Initially, the cell discharges at 50 C until the first mass transport limitation is reached at 2.7 s, where $c_{e,p}$ at the positive current collector is depleted causing a transition to Region 1. Both the electrolyte concentration overpotential and the Butler-Volmer (BV) reaction overpotential in the positive electrode increase, causing the current to drop (Fig. 3.6). All simulation scenarios capture this transition since it is determined by electrolyte properties that are identical across scenarios.

Around 20 s, $c_{\text{s,p}}^{\text{surf}}$ continues to increase and begins to saturate near a stoichiometry of 0.9 and enter the highly non-linear region of the U_{p}, significantly increasing the positive particle concentration overpotential. Meanwhile, a temporary magnitude decrease in $D_{\text{s,p}}$ at the particle surface allowed the $c_{\text{e,p}}$ to recover and a reduction in the electrolyte concentration overpotential. The transition is appropriately captured when concentration-dependent $D_{s,p}$ is incorporated in Scenario 2.

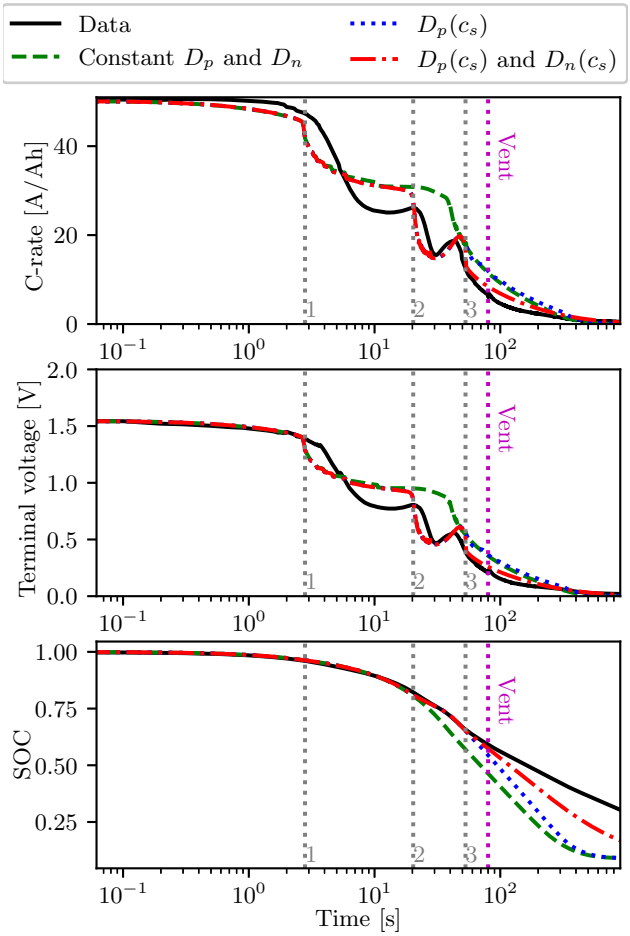


Figure 3.5: Effect of concentration-dependent diffusion [8]. ESC simulation with Cell 100A. Transitions are marked based on the simulation with concentration-dependent diffusion (red).

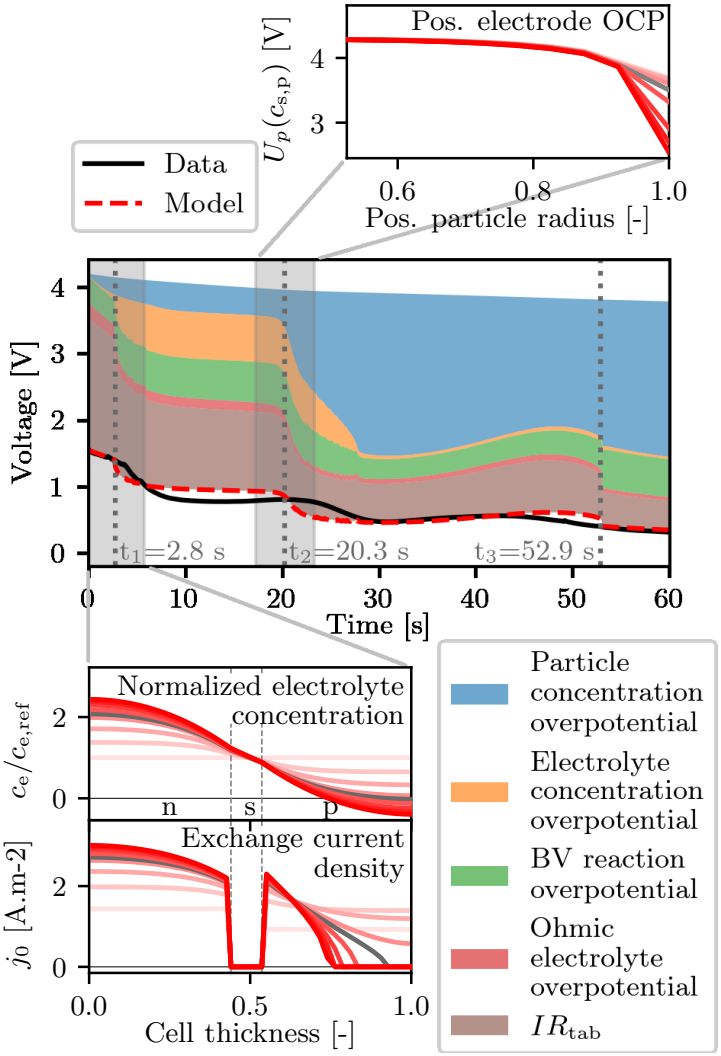


Figure 3.6: Temporal evolution of voltage overpotentials and spatial evolution of limiting concentrations during the transition points. The first transition is caused by concentration depletion in the electrolyte of the positive electrode. The second is due to increasing positive particle concentration overpotential from the steep decrease in U_p at high stoichiometric. Further definitions and equations are provided in Section B.1.

Finally, at 53.3 s, $c_{s,n}^{surf}$ depletes and approaches 0 and the negative electrode reaction overpotential increases, defining Region 3, which is only captured when concentration-dependent $D_{s,n}$ is incorporated in Scenario 3.

The causes of the transitions predicted from the SPMe are similar to those reported by Rheinfeld et al. which used a DFN model, but the order in which they occur differs [52]. In their work, the first transition occurred due to $c_{s,p}^{surf} \rightarrow c_{s,p}^{max}$ soon followed by $c_{e,p} \rightarrow 0$ at the positive current collector. This contrasts with the current work where the solid positive particle concentration does not saturate at $c_{s,p}^{max}$ and leads to an increase in solid concentration overpotential due to the nonlinearity at of U_p at high stoichiometries. The overpotentials reported in their work were also largely dominated by BV reaction overpotentials. This may partly be due to the more aggressive ESC implementation, where Rheinfeld et al. applied a 0 V short to achieve C-rates about a magnitude larger (about <800 C) than in these experiments (about <80 C) [66]. Additionally, the limitation from $c_{s,n}^{surf} \rightarrow 0$ occurs much later in their work; however, this can be attributed to underpredicted $D_{s,n}$ in this work at low SOC.

3.4 SEI decomposition parameterization

Before coupling the lumped thermal model and pouch venting models like in the previous EqCM-based multiphysics model, the SEI decomposition parameters will be revisited to better understand model error propagation in the coupled model. In Chapter 2 Section 2.5, the pouch venting submodel was introduced, which included gas generation from SEI decomposition. The earlier combined model results overpredicted the gas pressure and gas generation, which may be more reasonably attributed to a mismatch in the SEI decomposition parameters rather than those for electrolyte vaporization.

From the SEI decomposition reaction parameters, the frequency factor, A_{SEI} from Eq. 2.41 was selected as the fitting parameter for the expansion data and was informed by prior work. Borner et al. [44] showed that the reaction onset temperature is aging pathway-dependent, but the relationship between aging and SEI decomposition has yet to be attributed to specific model parameters. Additionally, MacNeil et al. found through accelerated rate calorimetry testing that E_{SEI} was consistent across different types of carbon electrode-electrolyte combinations, while A_{SEI} varied by two orders of magnitude and is strongly dependent on reaction surface area, supporting it being used as a fitting parameter [73]. Alternatively, the initial relative amount of SEI, $x_{SEI,0}$, can also be fitted or estimated through aging models by relating it to the loss of Li inventory due to SEI growth [60]. To minimize the number of fitting parameters, we only fit A_{SEI} for $x_{SEI,0}$ fixed and equal to the value from Coman et al.,

which comes from experiments using freshly formed SEI from the first charge [40, 58, 59, 74].

To fit A_{SEI}, an optimization problem was formulated to find a scalar (γ_A) for the nominal literature value ($A_{\text{SEI,0}}$), such that $A_{\text{SEI}}^{\text{opt}} = \gamma_A^{\text{opt}} A_{\text{SEI,0}}$. The cost function using mean-squared error is

$$\begin{aligned} \gamma_A^{\text{opt}} =& \arg\min_{\gamma_A} \frac{1}{N} \sum_{i=1}^{N} \left(\Delta\tilde{\sigma} - \Delta\sigma(\tilde{T}, \gamma_A) \right)^2 . \\ & \text{subject to: } 0 < \gamma_A \leq 1, \end{aligned} \tag{3.7}$$

where the model input is the measured cell temperature data, $\tilde{T}$; $\Delta\tilde{\sigma}$ is the expansion stress calculated from data with Eq. 2.1; and the modeled $\Delta\sigma$ is calculated from the venting model. The lower and upper bounds on γ_A were determined to ensure that SEI will decompose ($0 < \gamma_A$) and that the SEI for these calendar-aged cells is at least as thermally stable as the SEI from the first charge ($\gamma_A \leq 1$) [58, 59, 75]. For the fully-charged cells, the expansion data was fit up to when the cell vented, while the other cells were fit to the entire data. To fit the $\Delta\sigma$ for Cell100B, the temperature data was linearly interpolated where data was missing. The minimization problem was solved using a Derivative-Free Optimizer for Least-Squares (DFO-LS) solver [72].

Table 3.2: Summary of fitted A_{SEI} and venting model $\Delta\sigma$ prediction error for three values of A_{SEI}. Error metrics from simulation results with A_{SEI} equal to the literature value, value fitted to the cell, and value fitted to Cell 100A ($A_{\text{SEI}}^{\text{100A}}$) are presented. The error metrics include root-mean-squared error of Δ_σ ($\text{RMSE}_{\Delta\sigma}$) and error in venting timing (Δt_{vent}). $\text{RMSE}_{\Delta\sigma}$ is calculated for the time before venting occurs in simulation. The fit for Cell 100B used interpolated temperature data where data was missing.

	Coman et al 2017 $A_{\text{SEI,0}} = 1.67 \times 10^{15}$ s^{-1}		Fitted A_{SEI} ($\times 10^{15}$)			A_{SEI} from Cell 100A $A_{\text{SEI}}^{\text{100A}} = 0.132 \times 10^{15}$ s^{-1}	
Cell	$\text{RMSE}_{\Delta\sigma}$ [kPa]	Δt_{vent} [s]	A_{SEI} [s^{-1}]	$\text{RMSE}_{\Delta\sigma}$ [kPa]	Δt_{vent} [s]	$\text{RMSE}_{\Delta\sigma}$ [kPa]	Δt_{vent} [s]
100A	4.54	-26.1	0.132	2.10	-2.8	2.10	-2.8
100B	6.06	-13.8	0.398	4.42	-3.50	9.35	2.3
75	8.25	–	0.076	2.06	–	14.5	–
50	9.05	–	0.095	2.01	–	6.54	–

3.4.1 SEI decomposition parameterization results

For each cell, the SEI decomposition reaction frequency factor, A_{SEI} was fitted by solving Eq. 3.7. Error metrics from simulation results of each cell with A_{SEI} equal to the literature

value from [40] ($A_{\text{SEI},0}$), fitted value, and fitted Cell 100A value ($A_{\text{SEI}}^{\text{100A}}$) are presented in Table 3.2. The error metrics include root-mean-squared error of $\Delta\sigma$ ($\text{RMSE}_{\Delta\sigma}$) and error in venting timing (Δt_{vent}). Note that the simulation results shown in Fig. 3.7 represent the case where there is no error in cell temperature propagating from the thermal model and cases with ±2.2 °C bias error to illustrate the sensitivity of $\Delta\sigma$ to temperature.

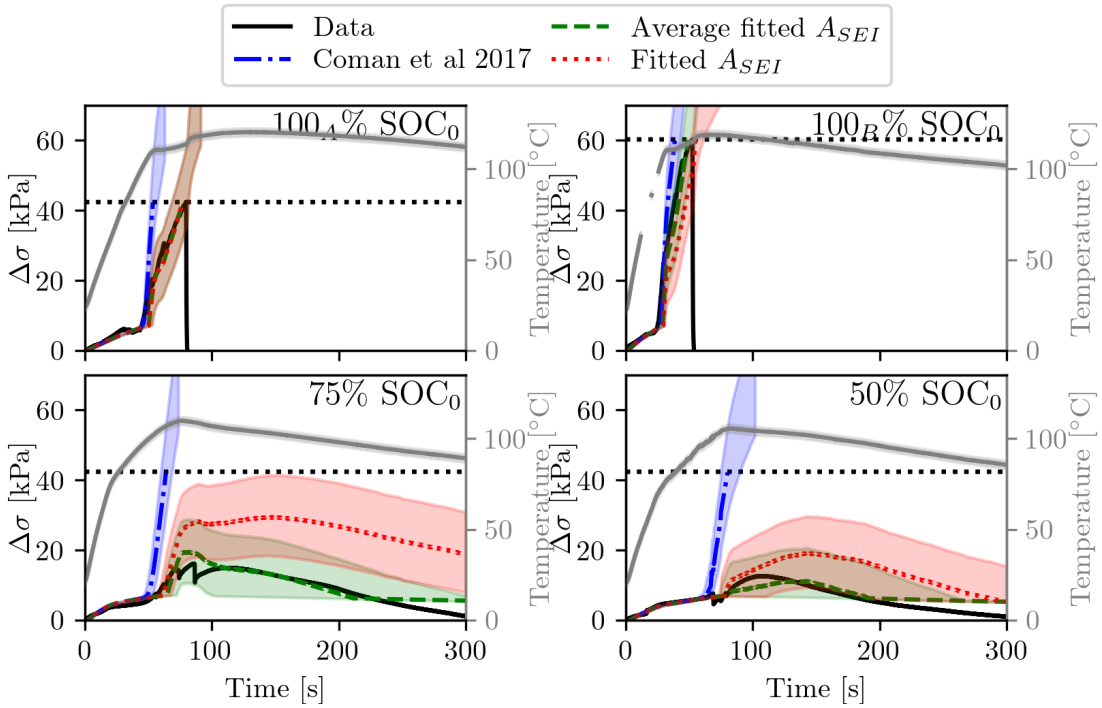


Figure 3.7: Result of tuning A_{SEI} using measured temperature with ±2.2 °C measurement bias error (right axis) and applying the literature value from Coman et al 2017 (blue), the cell's fitted value (green), and using the fitted value from Cell 100A (red)

Coman et al. 2017 used an A_{SEI} of 1.67×10^{15} s^{-1}, while the fitted values were consistently about a magnitude less and varied by about half a magnitude across all cells, leading to significantly different venting predictions. Using the literature value, the model predicts that all of the cells will vent, despite only the 100% SOC$_0$ cells venting in the experiment. In comparison, simulations using the fitted A_{SEI} and $A_{\text{SEI}}^{\text{100A}}$ correctly predict that venting only occurs in the fully-charged cells. However, the model overestimates the expansion of Cell 50 and Cell 75 since the $A_{\text{SEI}}^{\text{100A}}$ is almost twice as large.

Across all cells, the venting model predicts the evolution of expansion stress better with the fitted and $A_{\text{SEI}}^{\text{100A}}$ than with the literature value across multiple metrics. In general, $\text{RMSE}_{\Delta\sigma}$, $e_{\Delta\sigma}^{\max}$, and Δt_{vent} decrease from using the literature A_{SEI} to $A_{\text{SEI}}^{\text{100A}}$ to the fitted A_{SEI}. Note that $\text{RMSE}_{\Delta\sigma}$ is calculated for the time before venting occurs in simulation.

In all cases, Δt_{vent} is predicted conservatively except for the case with Cell 100B using the $A_{\text{SEI}}^{100\text{A}}$, where the model predicts venting 2.3 s after it occurs in the experiment.

According to these simulations, up to 6% of the initial SEI decomposed during the ESC, suggesting that negative electrode active material was not reexposed to the electrolyte, so we assume the next high-temperature exothermic reaction, SEI regeneration [22, 76], did not occur. However, it is possible that higher core temperatures can contribute to faster SEI decomposition and anode-electrolyte reaction locally.

If the temperature input is from a thermal model instead of from the data, the error from the preceding model will propagate. To illustrate the impact of temperature error, Cai et al 2021 found that when the thermocouple accuracy (±2.2 °C) was applied as a measurement bias error in the worst-case scenario, the vent timing could vary by as much as 12 s. The simulations here show similar results and also show that predicting maximum expansion stress at high temperatures is significantly more sensitive than at low temperatures, illustrated best in the partially charged cells. A ±2.2 °C error at room temperature gives a $\Delta\sigma$ range of less than 0.5 kPa, while that at peak temperature results in a range of 24 and 21 kPa for Cells 75 and 50, respectively, using the average $A_{\text{SEI}}^{100\text{A}}$. This reduces to 18 and 14 kPa using the fitted A_{SEI}. The large range in peak $\Delta\sigma$ highlights the importance of thermal model accuracy.

3.5 Results and discussion

The reduced-order models are coupled as in Fig. 3.1 by using the current and voltage loss from the SPMe to capture the heat generation input for the thermal model, then using the cell temperature from the thermal model as the input for the venting model to capture cell expansion. The only bidirectional coupling considered in these simulations is between the venting and thermal models, where the SEI decomposition heating is included as a source of heat generation. To summarize the parameters that were previously fitted for this model, R_{ESC}, R_{tab}, h, C_p, and A_{SEI} were fitted for each cell, while $D_{s,n}$ and $D_{s,n}$ were only fitted for Cell 100A. However, the simulation results shown in Fig. 3.8 for all four cells use one set of parameters with h, C_p, and A_{SEI} parameters from Cell 100A. Tables B.1 and B.2 in the supplemental material summarize the parameters used.

Overall, there are two main sources of error to consider in these simulation results: parameter mismatch and model error propagation. The model results with data input are shown as a baseline to illustrate the effect of parameter mismatch in the case of Cells 100B, 75, and 50. Comparatively, the model results using modeled inputs add the effect of model error propagation. Model errors are reported in Table 3.3, including the errors in final SOC ($\Delta\text{SOC}_{\text{f}}$),

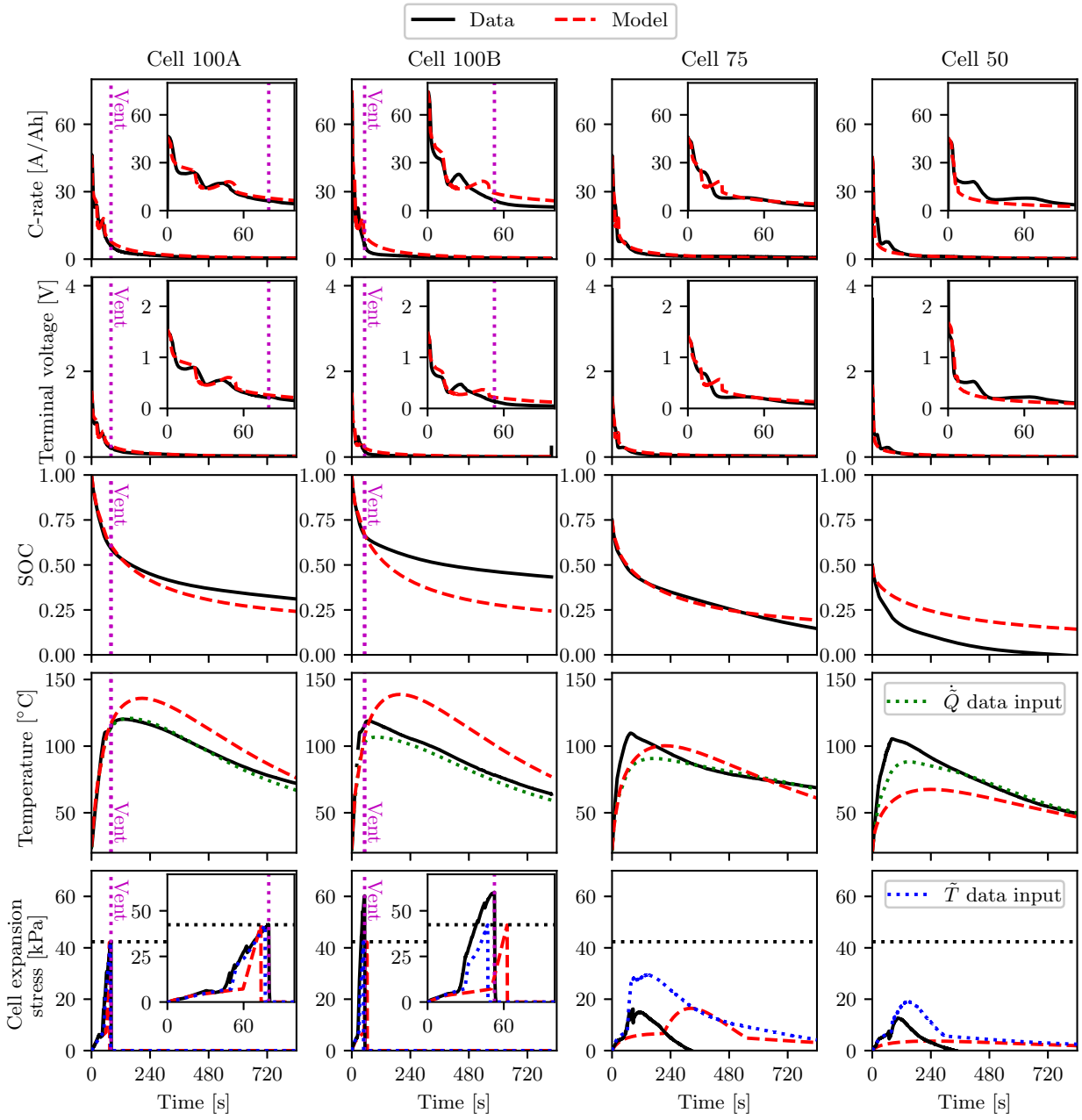


Figure 3.8: Combined multiphysics model simulation for a 15-min ESC with parameters from fitting Cell 100A. Submodel results with data inputs are shown to isolate the effect of parameter mismatch. The parameters that were fitted for each cell were R_{ESC}, R_{tab}, h, C_p, and A_{sei} with $D_{s,n}$ and $D_{s,n}$ only fitted for Cell 100A. The h, C_p, A_{sei}, $D_{s,n}$, and $D_{s,n}$ fitted for Cell 100A were used to simulate all SOCs.

maximum temperature ($\Delta T_{\max}$), and maximum cell expansion stress ($e_{\Delta\sigma}^{\max}$). RMSEs are calculated for the 15-minute simulation or until venting occurs in the simulation. To be conservative, we will assume that the venting threshold is the lower of the two experimental values, as in that from Cell 100A.

In general, the combined model was able to predict whether a cell would generate gas and vent. For Cells 100A and 100B, the model predicted venting about 6 s early and 10 s late, respectively. The model also predicted that Cell 75 would generate gas without venting, which is consistent with the data. The gas generation was delayed, which can be attributed to the propagated error in temperature. For Cell 50, the model did not predict expansion from gas generation due to the significantly underpredicted temperature.

Table 3.3: Summary of combined electrochemical-thermal-venting model simulation errors. $\Delta\text{SOC}_\text{f}$ is the error in the final SOC. $\Delta T_{\max}$ and $e_{\Delta\sigma}^{\max}$ are the errors in the maximum temperature and maximum cell expansion stress, respectively. All RMSEs are calculated for the 15-minute period. The exceptions are Cells 100A and 100B which vented, so the RMSE_σ is calculated until the simulation vents.

Cell	$\Delta\text{SOC}_\text{f}$	$\Delta T_{\max}$ [°C]	$e_{\Delta\sigma}^{\max}$ [kPa]	Δt_{vent} [s]	RMSE_I [A/Ah]	RMSE_V [V]	RMSE_T [°C]	$\text{RMSE}_{\Delta\sigma}$ [kPa]
100A	-0.07	15.6	–	-6.1	1.17	0.04	13.5	6.97
100B	-0.19	20.0	–	10.1	2.27	0.05	23.9	26.7
75	0.06	-9.5	0.28	–	1.28	0.05	9.2	0.73
50	0.15	-38.0	-8.93	–	1.67	0.04	19.9	2.33

Additionally, the fitted $D_{s,k}(c_{s,k})$ functions parameterized for Cell 100A qualitatively describe the transition between diffusion-limited regimes in the other cells. The timing of the transitions deviates more for the lower initial SOC cells which may be attributed to a few issues including operating in the low-SOC region of the $D_{s,k}(c_{s,k})$ curves where the values were extrapolated and increased sensitivity to errors in the OCV function [67]. The transitions also shift later which may be an issue with the stoichiometric window used to convert SOC to concentration and could be addressed through apriori differential voltage or differential capacity analysis [77].

The error across the different signals can partially be attributed to mismatched parameters, model error propagation, and unmodeled couplings. However, the impact of parameter mismatch may be less important considering that the qualitative conclusions drawn from the temperature and expansion stress in the simulation with data input agree with the experimental data. We still observe a large increase in temperature without triggering the next stage of decomposition reactions and gas generation for all cells with only the fully-charged cells venting.

However, the over-predicted discharge current and subsequently overpredicted temperature for Cells 100A and 100B may be explained by the increase in unmodeled resistance from electrolyte dryout after venting. At high temperatures, loss of liquid electrolyte through vaporization and venting can be thought of as a type of electrolyte dryout, which is a mechanism for resistance growth during LIB degradation due to the loss of ionic contact increasing charge transfer resistance [78]. Interpreting SOC error as an accumulated current error, the sudden growth in SOC error and overpredicted current after venting would both be indicative of unmodeled electrolyte dryout.

Also, recall that the electrochemical parameters in this work were treated as temperature-independent to avoid unrealistic discharge behavior under abnormally high temperatures, which included Arrhenius dependencies for parameters like diffusivity and conductivity that would effectively reduce the internal impedance during discharge. This may also partly explain why the SPMe largely underpredicts the discharge current for Cell 50 which also discharged at a lower average temperature than the other cells.

Across all cells, the reduced-order multiphysics model was able to capture many of the safety-relevant metrics laid out in Tables 2.1 and 3.3 to predict early short circuit abuse behavior and hazards. While there is room for improvement, the model can still be used for control design and implementation for battery safety applications.

3.6 Summary

This work shows that a reduced-order electrochemical model, initially parameterized for normal operation, can be adapted to model the electrochemical, thermal, and venting behavior during an ESC. A total of seven parameters were fitted with data to predict the first venting timing with A_{SEI}, peak temperature with h and C_p (in Chapter 2), and diffusion-limited electrical behavior with R_{ESC}, R_{tab}, $D_{\mathrm{s,p}}$, and $D_{\mathrm{s,n}}$.

When the models are coupled and used to simulate the ESC of all cells at different initial SOC with a single parameter set, the combined multiphysics model qualitatively captures the fast temperature rise, gas generation, and venting, where the vent timing predicted within almost 10 s before it occurs in the experiment. The model can also predict the cell SOC within 6% SOC for the fully-charged until the cell vents and 75% SOC cell for the 15-minute discharge. However, the model error propagation from over- and under-predicted discharge currents and temperatures for the fully-charged cells and 50% SOC cell, respectively, suggest that further improvements in model accuracy can be made by introducing additional couplings between the venting, thermal, and electrochemical models with some loss in parameterizability, which is left as future work.

CHAPTER 4

Pouch Venting Model Global Sensitivity Analysis for Fresh and Aged Cells

4.1 Introduction

Expansion force measurements for early detection are being explored for prismatic and pouch cells because of the high signal-to-noise ratio and fast detection speed. Additionally, these cell formats are stacked mechanically in series, allowing for efficient monitoring with fewer sensors, improving cost-effectiveness. However, ensuring the reliability of force-based sensing and algorithms throughout their lifespan is also necessary. Because direct testing is resource-intensive, modeling can be used to provide initial insights.

While previous studies have developed cell gas generation, expansion, and venting models, further research is needed to understand how these models and the physical systems they represent are influenced by factors such as aging, environmental changes, and uncertainties in model parameters. For prismatic cells, Ayayda et al. developed a model that captured the evolution of the thermal and internal gas pressure and validated it against experiments in which a gas pressure sensor was inserted into the cell through the seal pin, but the model does not capture the expansion force [79]. Chen et al. developed a three-dimensional thermomechanical numerical model of a prismatic cell that captures the internal gas pressure, expansion force, and deformation and showed that increasing preload leads to higher internal gas pressures and earlier vent timing [80]. While the model has high fidelity, it is also computationally complex with almost 200,000 nodes and over 120,000 elements. For pouch cells, Cai et al. developed a zero-dimensional model that captures the gas generation, expansion force, and vent timing under fixed displacement conditions, similar to those seen in application (e.g., electric vehicle packs)[27]. The computational efficiency allows the zero-dimensional model to be used in more complex control algorithms [81, 82].

In this study, a two-stage global sensitivity analysis is performed to first identify parameters that significantly influence the cell expansion force and then quantify the impact of

these parameters. Parameter sensitivity is considered across different temperatures, using an external short circuit (ESC) temperature profile, and age by adjusting parameter ranges based on existing literature. Lastly, long-term implications for real-world systems are examined by simulating the impact across the range of the key parameters. The contributions of this study include

- Identifying influential parameters and quantifying the effect of their uncertainty on cell expansion force across temperature for fresh and aged cells
- Discussing the implications of aging for force-based early thermal runaway detection and control.

4.2 Global sensitivity analysis

The global sensitivity analysis is based on a two-tiered approach. First, the Morris Method is used to help identify the most influential parameters and decrease the number of parameters of interest for the subsequent analysis. Then, the Sobol analysis, which is a variance-based sensitivity analysis, is used to quantify the sensitivity of the identified parameters at different stages of cell expansion and vent timing. The analyses were performed using the Sensitivity Analysis Library (`SALib`) [83, 84].

Sensitivity analyses are performed for fresh and aged cells by adjusting the parameter ranges to evaluate the effect of aging on venting. For a fresh cell, we use a 10% uncertainty in all parameters, assuming that this captures realistic to worst-case scenarios given prior cell and fixture material characterization testing and accounting for manufacturing variability. For an aged cell, the parameter ranges of degradation-dependent parameters, including those related to SEI decomposition and preload compression, are adjusted according to values reported in the literature. The parameters included in the sensitivity analysis are listed in Table 4.1 along with the nominal values and any change in the parameter ranges between the fresh and aged cell cases.

4.2.1 Morris method

First, a qualitative global sensitivity analysis is used to identify the most influential parameters for cell expansion stress and vent timing using the Morris method [83, 84, 85]. The Morris method (MM), or Method of Elementary Effects, is a preliminary analysis for screening model parameters by providing qualitative insight into parameter influence with relatively few model evaluations. Additionally, the results can help justify model simplifications for improved computational efficiency.

The MM is based on a one-at-a-time (OAT) approach, but uses trajectory design to explore a discretized parameter space more efficiently. The discretized parameter space is defined by the number of levels (n_l) used to span the range of each parameter, $x_k \in [x_k^{\min}, x_k^{\max}]$ for $k \in 1, 2, ..., N_p$, where N_p is the total number of parameters. The distance between the levels is $\delta = (x_k^{\max} - x_k^{\min})/(n_l - 1)$, where a parameter perturbation (Δ) is defined as an integer multiple of δ.

Trajectory design is then used to explore the parameter space, where the total number of trajectories in a trajectory design is N. Starting from a randomized base set of parameters, each step along a trajectory perturbs one additional parameter, where each parameter is only perturbed once per trajectory. The total number of model evaluations for a trajectory, including the base set of parameters, is $N_p + 1$.

Then, the influence of each parameter is quantified by calculating the elementary effect (EE) at each step of each trajectory and the overall statistics for the corresponding distribution of EEs for each parameter across all trajectories. The EE of the k-th parameter is calculated as

$$EE_k = \frac{1}{\Delta}\big[f(x_1, x_2, ..., x_k + \Delta, ...x_n) - f(x_1, x_2, ..., x_n)\big]. \tag{4.1}$$

For the resulting distribution of EE_k, the mean magnitude, μ_k^*, captures the overall influence without considering the direction. The standard deviation (σ_k) quantifies the variability and indicates potential non-linearities and parameter interactions. These metrics are calculated as

$$\mu_k^* = \sum_{n=1}^{N} \left| \frac{EE_k^{(n)}(x_k)}{N} \right| \tag{4.2}$$

$$\sigma_k = \sqrt{\sum_{n=1}^{N} \frac{(EE_k^{(n)}(x_k) - \mu_k)^2}{N}}. \tag{4.3}$$

In the MM analysis in this work, the parameter space is discretized using $n_l = 20$, so $\delta = 0.053$, or about 5.3% of the total parameter range. The number of trajectories is $N = 100$ for a total of $N(N_p+1) = 2{,}600$ simulations. By comparing the relative magnitudes of μ_k^* and σ_k between parameters, the most influential parameters are identified and included in the following more thorough variance-based sensitivity analysis.

Table 4.1: Overview of venting model parameters included in the sensitivity studies. Parameter ranges used for fresh cell analysis are assumed to be ±10% of the nominal. Parameter ranges not listed for aged cell analysis are the same as for the fresh cell.

Param.	Description	Unit	Nominal value	Aged cell range	References
P_0	Initial cell compression stress	kPa	151	(20, 80)	[28, 86]*
$V_{h,0}$	Initial head space volume	m^3	6.65×10^{-6}	-	[27]
$L_{f,0}$	Initial foam sheet thickness	mm	2.4	-	[27]
$E_{f,0}$	Nominal Young's modulus of the foam sheet	kPa	190	-	[27]
k_{E_f}	Thermal coefficient of stiffness of the foam sheet	kPa/K	0-2.8	-	Assumed
$L_{c,s,0}$	Initial cell thickness	mm	5.5	(4.95, 5.51)	[28, 87]
E_c	Young's modulus of the cell	MPa	247	(200, 300)	[88]
α	Thermal expansion coefficient of the cell	μm/K	1.1	-	[27]
m_{an}	Mass of the negative electrode active material	g	19.1	-	[27]
A_{SEI}	Frequency factor for SEI decomposition	s^{-1}	1.32×10^{14}	$(2.42\times10^{11}, 1.67\times10^{15})$	[40, 46]
$E_{a,\text{SEI}}$	Activation energy for SEI decomposition	J	2.24×10^{-19}	$(1.73, 2.24)\times10^{-19}$	[40, 46]
$x_{\text{SEI},0}$	Initial fraction of Li in SEI	-	0.15	(0.14, 0.45)	[40, 60]

* Full-range approximately scaled by cell thickness from Xu et al. [86].

4.2.2 Sobol method

The Sobol method is a variance-based global sensitivity analysis used to quantify the contribution of each input parameter and their interactions to the variance in model output, making it well-suited for models with non-linear and interdependent relationships. By identifying which parameters cause the most total uncertainty, the Sobol method can be used to guide future work to improve overall model prediction accuracy. More details about the algorithm and implementation in `SAlib` are available in [83, 84, 89, 90] but are summarized here.

Compared to the Morris method, Sobol's method provides a comprehensive understanding of input influences by decomposing the model output variance into a sum of partial variances that include the contributions from individual input parameters and their interactions [89, 90]. It considers that the model function f decomposes into a sum of contributions

$$\begin{aligned} y = & f(x|\mathbf{p}) = f_0 + \sum_{i=1}^{N_p} f_i(x|p_i) \\ & + \sum_i \sum_{i<j} \big[f_{i,j}(x|p_i, p_j) + \cdots \\ & + f_{1,2,\cdots,N_p}(x|p_1, \cdots, p_{N_p}) \big], \end{aligned} \tag{4.4}$$

where y is the model output (i.e., cell expansion stress), x is the time-dependent model input (i.e., cell temperature), and $\mathbf{p} = \{p_1, p_2, \ldots, p_{N_p}\}$ are the model parameters.

By construction, the output variance can also be decomposed as a sum of partial variances attributable to each parameter and their interactions, such that

$$\mathrm{var}(y) = \sum_{i=1} V_i + \sum_i \sum_{i<j} V_{i,j} + \cdots + V_{1,2,\ldots,k}, \tag{4.5}$$

where

$$\begin{aligned} V_i &= \mathrm{var}(E(y|_{p_i})) \\ V_{i,j} &= \mathrm{var}(E(y|_{p_i,p_j})) - V_i - V_j \\ V_{\theta \subseteq \mathbf{p}} &= \mathrm{var}(E(y|_\theta)) - \sum_\theta V_\theta. \end{aligned}$$

The first-order effects are V_i, second-order effects are $V_{i,j}$, and so on with V_θ where $\theta \subseteq \mathbf{p}$ for higher-order effects. The corresponding sensitivity indices, or Sobol indices, are calculated

as a ratio of the partial variance to the output variance

$$S_\theta = \frac{V_\theta}{\text{var}(y)}. \tag{4.6}$$

The first-order indices, S_i, measure the direct contribution of each parameter without interactions to the output variance. Second-order indices, $S_{i,j}$, and higher-order indices measure the interactions between parameters. For this work, we only consider second-order indices. The total Sobol index reflect the overall parameter influence, including all interactions, and is calculated as

$$S_i^{\text{total}} = \frac{\text{var}(y) - \text{var}(E(y|_{p_{-1}}))}{\text{var}(y)} \tag{4.7}$$

$$= \frac{E(\text{var}(y|_{p_{-1}}))}{\text{var}(y)}, \tag{4.8}$$

where $V(E(y|_{x_{-i}}))$ is the total contribution of non-x_{-i} terms to the output variance. As an example with $N_p = 3$, $S_1^{\text{total}} = S_1 + S_{1,2} + S_{1,3} + S_{1,2,3}$.

The Saltelli quasi-random sampling was used for sampling the parameter space for Monte Carlo simulations. A total of $N(2N_p + 2) = 12,288$ simulations were run, where $N_p = 5$ and $N = 2^{10}$.

4.3 Results and discussion

Identifying the key parameters that influence the uncertainty of the modeling output and understanding their long-term implications for detection and control can provide insights for future investigations. Global sensitivity analysis addresses the former, while comparing simulation results across individual key parameters addresses the latter.

4.3.1 Global sensitivity analysis

For the sensitivity analysis, we can consider both cell expansion stress and vent timing as outputs, where the former is time-varying. Additionally, we examine the temperature-dependence of the model sensitivity for the given external short circuit temperature profile due to the strong non-linearity in gas generation at high temperatures.

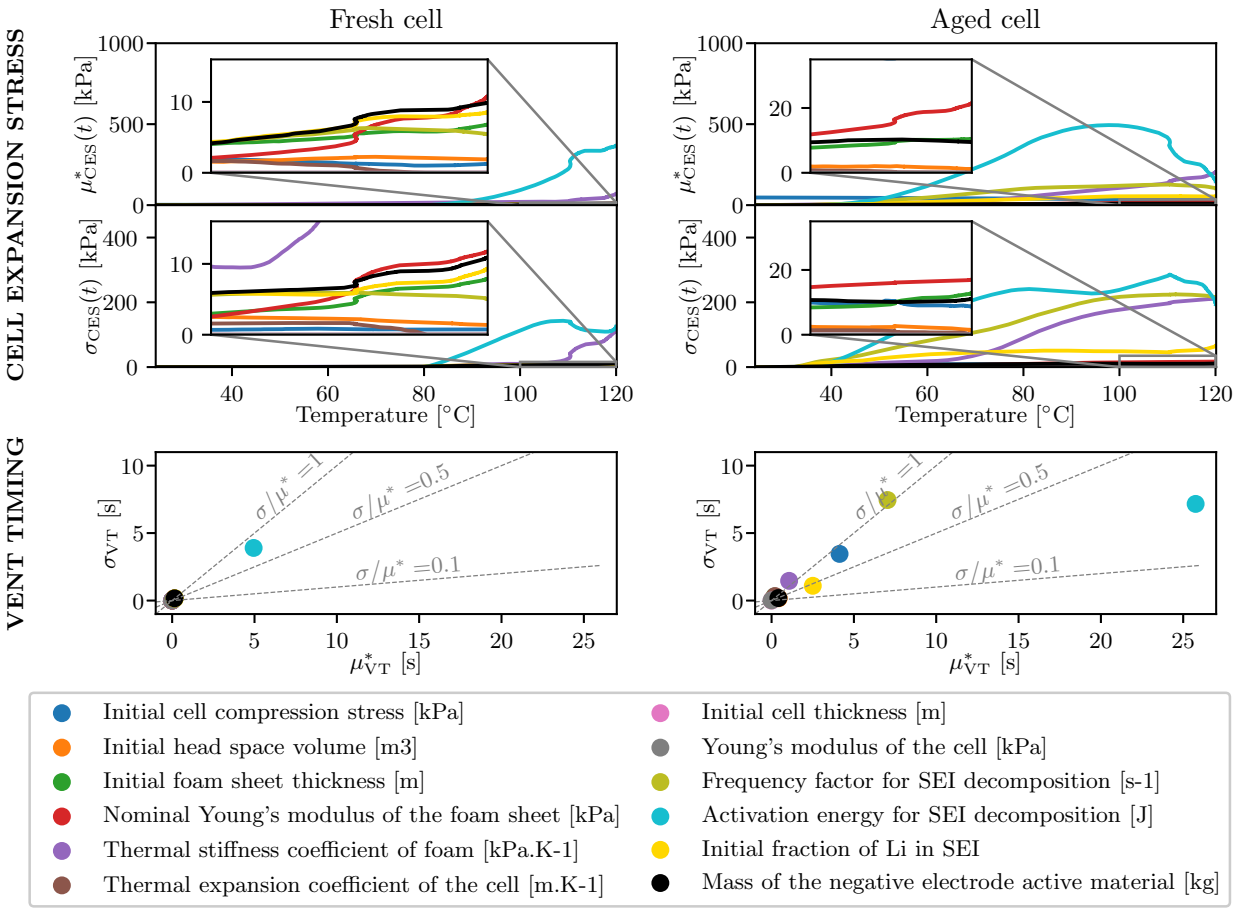


Figure 4.1: Morris method sensitivity analysis for cell expansion stress (top) and vent timing (bottom) for a fresh cell and an aged cell.

4.3.1.1 Morris parameter screening

From the Morris analysis, the non-influential parameters can be identified based on the corresponding values of μ_k^* and σ_k for each parameter k. Fig. 4.1 illustrates the results of the Morris analysis. For the purposes of this study, the influential parameters are those that affect the cell expansion stress by more than 20 kPa ($\mu^*_{\mathrm{CES},k}$ or $\sigma^*_{\mathrm{CES},k}$ >20 kPa) or vent timing by more than 5 s ($\mu^*_{\mathrm{VT},k}$ or $\sigma^*_{\mathrm{VT},k}$ >5 s), assuming $P_{\mathrm{crit}} = 57$ kPa. Using this criterion, two influential parameters were identified for the fresh cell (i.e., $E_{a,\mathrm{SEI}}$ and k_{E_f}), and five influential parameters were identified for the aged cell (i.e, $E_{a,\mathrm{SEI}}$, σ_0, A_{SEI}, $x_{\mathrm{SEI},0}$, and k_{E_f}). In this case, the influential parameters, except σ_0, show a large influence at high temperatures above 60 ° C. All other parameters are considered non-influential, including $E_c \to \infty$, for example, justifying the rigid cell stack assumption from Cai et al. [27].

4.3.1.2 Sobol variance-based sensitivity

The Sobol analysis quantified the sensitivity by attributing the variance in cell expansion stress to uncertainty in each influential parameter (i.e, $E_{a,\mathrm{SEI}}$, σ_0, A_{SEI}, $x_{\mathrm{SEI},0}$, and k_{E_f}). Fig. 4.1 shows the results of the Sobol analysis, including the 95% prediction interval for cell expansion stress and the Sobol indices. Similar to the Morris analysis, the Sobol analysis indicates that SEI decomposition parameters have a significant impact on cell expansion behavior at high temperatures, whereas initial cell compression stress has the most significant influence at low temperatures.

In general, the variability in cell expansion stress increases with temperature, as indicated by the widening range of the 95% prediction interval (Fig. 4.1). As expected, the fresh cell shows less variability in cell expansion stress than the aged cell at the same temperatures. For the fresh cell, the output uncertainty can largely be accounted for by the uncertainty of three of the five influential parameters. These are σ_0, k_{E_f}, and $E_{a,\mathrm{SEI}}$ that dominate at low ($T \leq 40°\mathrm{C}$), intermediate ($40°\mathrm{C} < T \leq 100°\mathrm{C}$), and high ($T > 100°\mathrm{C}$) temperatures, respectively. In contrast, for the aged cell, the variability in cell expansion stress is predominantly determined by uncertainty in σ_0 when $T < 40°\mathrm{C}$. Above 40°C, the influence of σ_0 decays and transitions to mainly $E_{a,\mathrm{SEI}}$ with smaller contributions from A_{SEI} and k_{E_f}. Furthermore, parameter interactions become more significant at high temperatures for the aged cell, primarily due to $E_{a,\mathrm{SEI}}$ with smaller contributions from $x_{\mathrm{SEI},0}$ and A_{SEI}.

4.3.2 Modeled implications for force-based detection and control

Many previous studies suggest that force-based detection is a good indicator for early thermal runaway detection [21, 91, 92, 93, 94, 95]; however, there is limited discussion of the

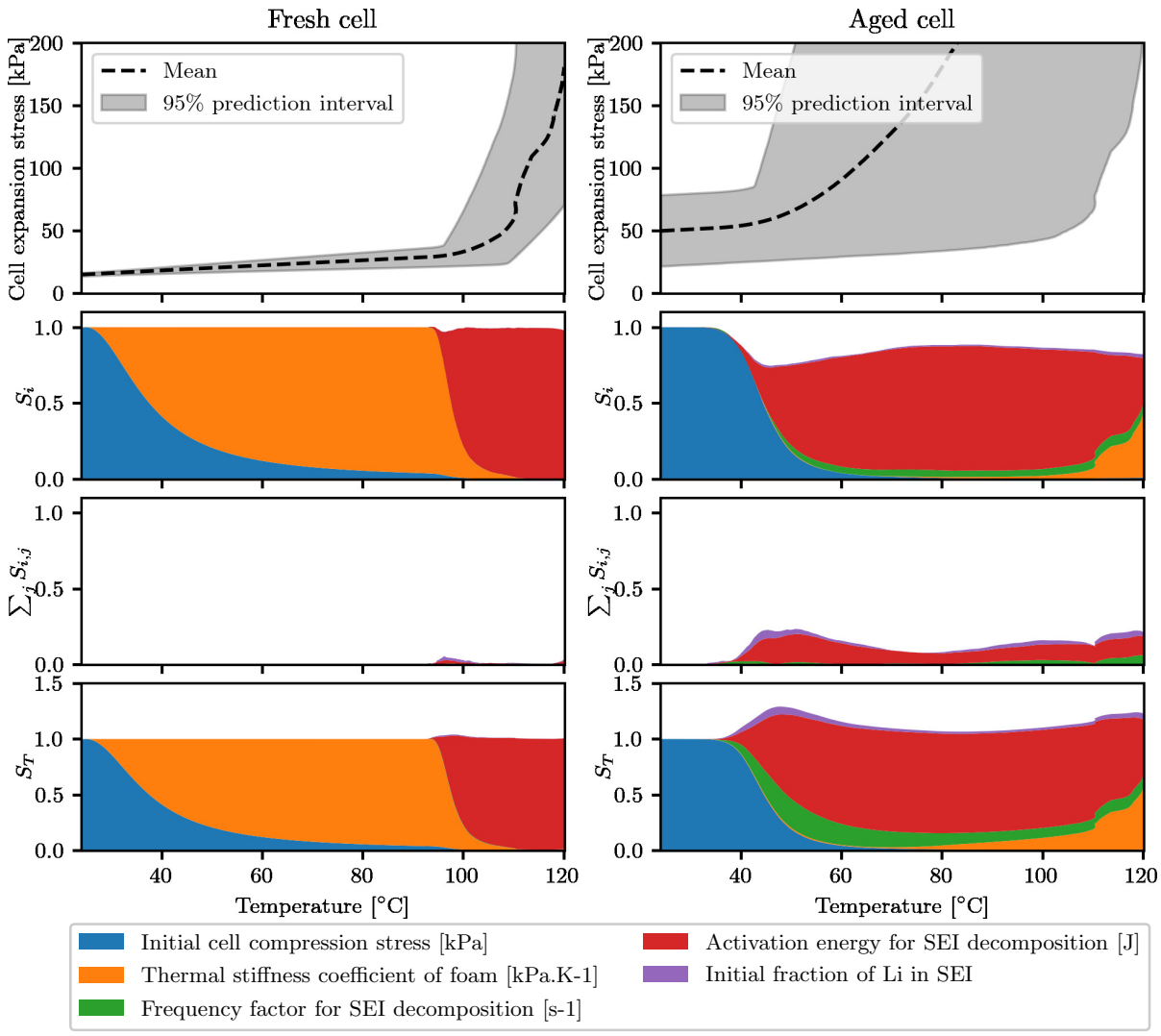


Figure 4.2: Sobol indices for cell expansion stress (top) and vent timing (bottom) for a fresh cell and an aged cell.

effectiveness of force-based detection as batteries age. Similarly, discussions about the use of feedback with measured expansion force during a controlled, fast discharge to mitigate failure hazards rely on the observability of gas expansion to prevent first venting [81]. Using the venting model, we can examine some of the long-term challenges of implementing force-based detection and control by qualitatively examining the effect of the most sensitive parameters.

4.3.2.1 Impact of preload pressure

Irreversible expansion in LIB cells can significantly increase the effective preload pressure before failure as the cells age. Overall, there are two notable effects shown in Fig. 4.3: earlier vent timing and decreased observability of the gas expansion stage. Previous studies experimentally investigated the effect of preload pressure on prismatic cells and observed similar behaviors [80, 91]. Although prismatic cells are a more rigid form factor compared to pouch cells, their geometric similarities offer useful comparisons.

By increasing the initial preload force, σ_0, in the model, we see that the expansion force profile shifts to higher pressures. At the same time, venting shifts to earlier times due to Boyle's Law, where the increased preload pressure suppresses the gas volume expansion and increases the internal gas pressure. This relationship is represented by Eqs. 2.37 and 2.38, assuming that the gas generation rates are independent of P_{gas}. Earlier vent timing with increased preload was also observed experimentally in prismatic cells by Chen et al. [80]. They also observed earlier gas generation, potentially due to increased thermal conductivity at higher preload pressures, which is a thermal-mechanical coupling not captured in this work.

Furthermore, the model suggests that an increase in preload leads to a decrease in the observability of the gas expansion stage and, ultimately, first venting up until the preload exceeds the critical pressure ($\sigma_0 > P_{\text{crit}}$) when it can no longer be observed. For the case where the preload is less than the critical pressure ($\sigma_0 < P_{\text{crit}}$), experimental data from Li et al. illustrate the initial decrease in observability with increasing preload in the overheating tests of prismatic cells [91]. However, for cells with considerably lower critical venting pressures such as pouch cells, the case where $\sigma_0 > P_{\text{crit}}$ and only the solid expansion stress is observable becomes more relevant. In the latter case, gas generation still occurs and gas pressure still increases, but venting will occur before the gas pressure can overcome the compression from the solid expansion stress, making it unobservable.

Overall, the results of the pouch venting model coupled with previous experimental results of the prismatic cell suggest that the expansion force may not be a reliable early thermal runaway indicator at high preload pressures. Although this study highlights the case for

aged cells, high preload pressures can also occur when a large number of cells are stacked mechanically in series and has implications for the effectiveness of expansion force-based detection with battery module and system design.

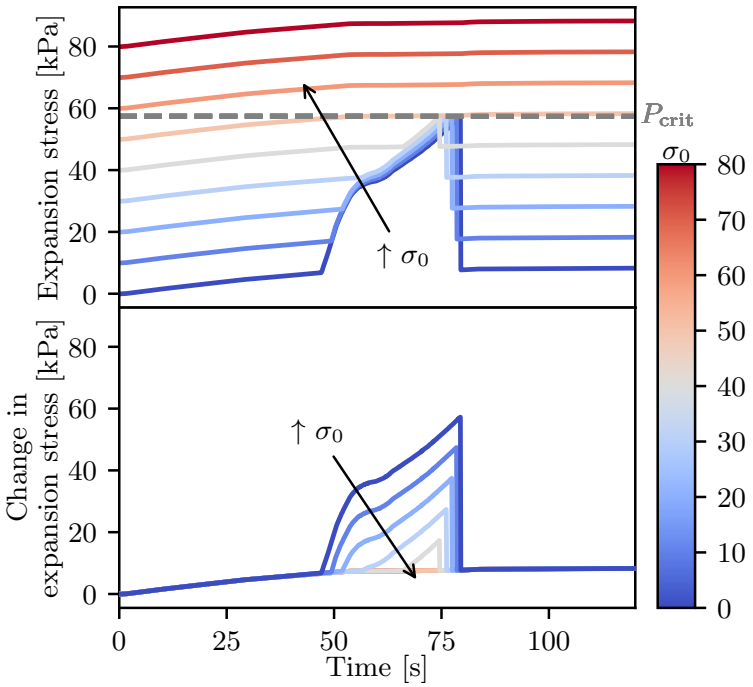


Figure 4.3: Effect of increasing preload pressure according to the venting model. As the preload pressure increases, the drop in expansion force becomes less observable. After the stress due to solid expansion surpasses the critical venting pressure, venting is unobservable.

4.3.2.2 Impact of foam sheet stiffness with temperature

The uncertainty in the temperature dependence of the foam sheet stiffness accounts for a significant portion of the uncertainty in the expansion force at intermediate temperatures for the fresh cell, but is overshadowed by uncertainties in other parameters in the aged cell. The effect of k_{E_f} is shown in Fig. 4.4. The model suggests that increasing k_{E_f} can effectively increase the observability of abnormal temperatures through solid expansion, as shown in Eq. 2.28, leading to earlier detection. However, similar to the previous case with high preload pressures, gas expansion and venting will become more difficult to detect using force-based detection.

4.3.2.3 Impact of SEI decomposition parameters

The strong influence of $E_{a,\text{SEI}}$ and A_{SEI} in aged cells, along with $x_{\text{SEI},0}$ parameter interactions, highlights the importance of exploring their parameterization in future work, but we can

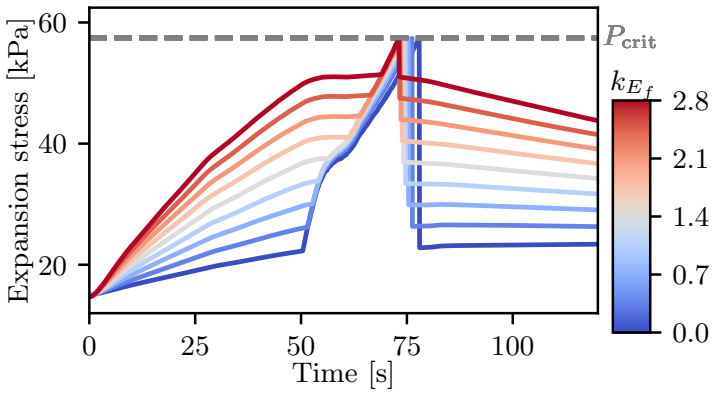


Figure 4.4: Increased temperature-dependence of foam stiffness improves observability of solid expansion stress

first use the model to help understand their effect on cell expansion. Fig. 4.5 illustrates the individual effect of each of the SEI decomposition parameters for the parameter ranges used to simulate the fresh and aged cases. The increasing influence due to uncertainty in $x_{\text{SEI},0}$, A_{SEI}, and $E_{a,\text{SEI}}$, in that order, is reflected in the widening range of cell expansion stress and vent timing.

As the cell ages, each parameter can ultimately advance (i.e., $E_{a,\text{SEI}}$ and $x_{\text{SEI},0}$) or delay (i.e., A_{SEI}) venting compared to the fresh cell. In the case where there is Li plating, $E_{a,\text{SEI}}$ decreases, reflecting the decrease in the thermal stability of SEI [46]. This leads to earlier SEI decomposition and gas generation at lower temperatures, which is captured in the cell expansion behavior by an earlier transition to the gas expansion stage. However, previous work also suggests that high temperature aging can lead to improved SEI thermal stability [44], but the Arrhenius reaction parameters have not been quantified and therefore not considered here. In contrast, A_{SEI} mainly affects the reaction rate and therefore the expansion rate during the gas expansion stage. Previous studies suggest that A_{SEI} depends on the surface area and the aging pathway [46, 73]. Compared across multiple studies, A_{SEI} may be lower in aged cells than in fresh cells, but A_{SEI} has not been characterized for fresh and aged cells in the same dataset, making this evolution not definitive [28, 40, 46]. Ultimately, these issues and uncertainties highlight the parameterization issues to be addressed in future investigations.

4.4 Summary

In summary, this chapter highlights the importance of understanding how aging impacts early thermal failure behaviors to ensure the reliability of force-based control algorithms.

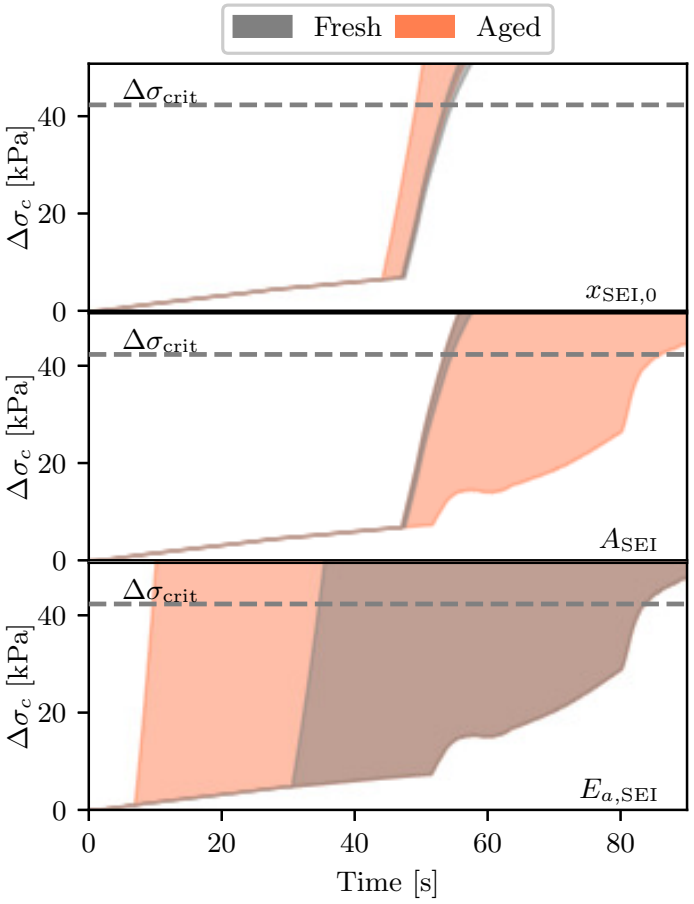


Figure 4.5: Example of uncertainty in $x_{\text{SEI},0}$, A_{SEI}, and $E_{a,\text{SEI}}$, respectively, for fresh and aged cells, where $\Delta\sigma_{\text{crit}} = P_{\text{crit}} - \sigma_0$.

A global sensitivity analysis was performed to identify key parameters, showing that the uncertainty of the parameters related to the preload, the SEI decomposition reaction, and the temperature dependence of the foam stiffness are most influential for cell expansion force across different temperatures and ages.

Furthermore, by exercising the model across the influential parameters, we observed several trends that may provide insights into long-term challenges associated with implementing force-based control algorithms. First, increasing preload pressure decreases the observability of expansion due to gas generation, where relatively low critical venting pressures may obscure it entirely. However, by choosing a foam material, or other compliance-providing material, with stronger temperature-dependent stiffness, the sensitivity of expansion force to temperature is expected to increase, potentially allowing for earlier detection due to solid expansion. Lastly, the large variability in aging-dependent SEI decomposition and associated gas generation highlights the need for future studies to investigate the relationship between cell degradation and SEI decomposition parameterization.

CHAPTER 5

Inhomogeneity-aware State-of-Health Estimation for Bounding Li Consumption from SEI growth in Aged Cells

5.1 Introduction

To explore the parameterization of the influential lithium-ion battery (LIB) pouch cell venting model parameters from Chapter 4 in-situ without battery abuse tests, we consider using state-of-health (SOH) diagnostics. Specifically, this approach can inform the initial parameters related to solid-electrolyte interphase (SEI) quantity and thermal stability before failure occurs in aged cells. However, to provide more robust SOH diagnostics for cells with high capacity loss, inhomogeneity should be considered.

The inhomogeneity of LIBs directly impacts the performance, lifetime, and safety of batteries by accelerating degradation [96, 97]. Inhomogeneity in LIBs generally refers to non-uniform distributions of materials, properties, and operating conditions caused by a variety of factors from both manufacturing and degradation, where this work focuses on the latter [97]. Within a cell, these lead to an inhomogeneous distribution in active lithium, current density, or capacity that can be observed in bulk through voltage measurements [98, 99]. In extreme cases, it can lead to increased safety risks by creating conditions that lead to battery abuse, including localized overheating, overcharging, and internal short circuits, increasing the risk of thermal runaway.

By characterizing and monitoring LIB inhomogeneity, battery management strategies can be developed to mitigate performance loss and safety risks, especially for aged cells. Although previous research has already shown that inhomogeneity can be characterized and attributed to multiple degradation mechanisms, there is limited discussion of the evolution of inhomogeneity itself with respect to temperature and how its relationship to other degradation modes can provide additional insight into the underlying degradation mechanisms.

Previous studies using differential voltage analysis (DVA) attribute the smoothing of differential voltage (DV) features in aged cells, originating from active material phase transitions, to increased inhomogeneity. Coupled with in-situ and postmortem analyses, the heights of the peaks were correlated with the temporal evolution and spatial distributions of state-of-charge (SOC), Li plating, and cover layer growth [98, 100, 101, 102]. Unlike correlational studies, Sieg et al. connected coin cells composed of electrode materials from a degraded cell in a parallel array to directly show that inhomogeneous lithium distributions lead to DV peak smoothing behavior [103].

By coupling DVA algorithms, which identify degradation modes such as loss of lithium inventory (LLI) and loss of active material (LAM), with electrode models that capture distributions of lithium or electrode capacity, previous work demonstrated that inhomogeneity can be characterized along with typical degradation modes as cells age. Fath et al. modeled a linear distribution of LLI and fitted the slope for cells aged under different cycling conditions, including combinations of EV and C-rate profiles and SOC windows at 25°C, with up to 20% capacity loss [103, 104]. The algorithm was used in follow-up modeling work to characterize cells aged at temperatures of 30 °C and 50 °C, where the researchers attributed inhomogeneity to SEI growth and model error to Li plating [105, 106]. Alternatively, the multi-species, multi-reaction (MSMR) model can directly model a lithium distribution and attribute capacity loss to specific insertion reactions to capture peak smoothing behavior [107]; however, it becomes difficult to interpret the evolution of more than 30 parameters. Kirst et al. developed a method that merges the two approaches [99]. They used the MSMR model with bi-level optimization to characterize cells with graphite and silicon-graphite blend anodes. Cell inhomogeneity was captured by a normal distribution of the electrode capacities for each electrode. The algorithm required fitting five local parameters for graphite anode cells throughout life and three global parameters per phase transition (18 total global parameters) to model the underlying OCPs. The validation included a graphite anode cell cycled at 25°C to about 10% capacity loss with <5 mV voltage RMSE throughout life. Although these studies indicate that inhomogeneity increases with age, they offer limited analysis of its growth, especially at different aging temperatures, and have only begun to explore its potential to provide insights into the underlying degradation mechanisms.

In this study, we consider inhomogeneity as another degradation mode and characterize it using a DVA algorithm augmented with a Gaussian negative electrode capacity distribution model for cells aged under different conditions. We then show that characterizing the evolution of inhomogeneity can provide a more comprehensive understanding of the dominant degradation mechanisms. The contributions of this work include the following:

- Quantification of inhomogeneity for cells aged under a range of C-rates and tempera-

tures down to at most 50% capacity loss

- Analysis of inhomogeneity growth relative to other degradation metrics to provide insights into previously observed degradation mechanisms
- Relating degradation modes to early failure behavior through SEI decomposition parameters
- Error comparison between DVA with and without modeling inhomogeneity to justify the increased model complexity through the reduction of DV model error as cells age.

For the remainder of this chapter, Section 5.2 details the cell aging conditions. Section 5.3 and 5.4 describe the full cell open-circuit voltage (OCV) model and parameter fitting algorithm. Section 5.5 presents the results of the characterization, discusses trends in aging conditions and degradation metrics, and provides an error comparison between a standard DVA algorithm with and without modeling inhomogeneity.

5.2 Cell aging experiments

A total of 41 NMC622/G pouch cells with a nominal capacity of 2.5 Ah were aged under various calendar and cycle aging conditions. The cells were manufactured at the University of Michigan Battery Lab (UMBL) and formed using three C/10 cycles followed by a reference performance test (RPT). All cells were placed in a constant-pressure, spring-loaded fixture set to 5 PSI (34.5 kPa) with a T-type thermocouple and an inductive proximity sensor to measure expansion [108]. The aging conditions are summarized in Table 5.1 along with the number of cells aged under each condition.

The cells were aged at three different temperatures, i.e., cold (0°C), room (about 25°C), or hot (45°C). Cells aged at 0°C and 45°C were cycled using Neware CT-4008Tn-5V6A-S1 cyclers and MHW-200 thermal chambers, while cells aged at 25°C were cycled at room temperature using an Arbin BT2000 cycler. Calendar-aged cells were aged at voltages of 3.5, 3.8, and 4.1 V at room temperature, corresponding to 15, 50, and 90% SOC_f, respectively, where SOC is relative to the nominal, fresh cell capacity (SOC_f). Additionally, cells were calendar-aged at 4.1 V at cold and hot temperatures.

Cycle-aged cells were aged under different C-rate profiles down to different capacity-based state-of-health (SOH) conditions. Most cycles are full constant-current constant-voltage (CCCV) cycles with an operating voltage window of 3.0 V (0% SOC) to 4.2 V (100% SOC). The CC phases are either at C/3 or 2C with a CV phase only at the top of charge using a cutoff current of C/20. The intracycle profiles use a combination of the two C-rates to mimic

Table 5.1: Overview of test conditions

Cell IDs	Number of cells	Temperature [°C]	Aging type	Aging Profile	End SOH [Ah/Ah %]
52, 60, 69	3	25	CYC	C/3	85
76, 89, 93	3	25	CYC	C/3	70
61, 63, 66	3	25	CYC	C/3	50
50, 62, 67	3	25	CYC	2C	70
53, 58	2	25	CYC	IC	70
70, 86	2	25	CYC	ID	70
77	1	25	CAL	4.1 V (90% SOC)	-
59	1	25	CAL	3.8 V (50% SOC)	-
56	1	25	CAL	3.5 V (15% SOC)	-
94, 97	2	0	CYC	C/3	85
45, 51, 87	3	0	CYC	C/3	70
39, 54, 65	3	0	CYC	C/3	50
42, 91	3	0	CYC	2C	70
72	1	0	CAL	4.1 V (90% SOC)	-
33, 36	2	45	CYC	C/3	85
46, 57, 78	3	45	CYC	C/3	70
47, 84, 85	3	45	CYC	C/3	50
41, 88	3	45	CYC	2C	70
48	1	45	CAL	4.1 V (90% SOC)	-

a simplified drive cycle and a fast charging profile on discharge and charge, respectively. The intracycle discharge (ID) consists of a repeated sequence of 2-min 2C discharge, 8-min C/3 discharge, and 1-min rest until the low voltage limit is reached, followed by a C/3 CCCV charge. The intracycle charge (IC) consists of a 2C CC charge to 4.2 V (no CV) and a C/3 CCCV to 4.2 V, followed by a C/3 discharge. Cycle aging cells continued to cycle until they reached 85, 70, or 50% SOH, defined by the C/20 charge capacity, after which they continued to rest and calendar age at the prescribed temperature at 3.3 V.

5.2.1 Reference performance tests

Reference performance tests (RPT) were conducted at 25° C, or room temperature, to characterize cell capacity and resistance during aging. Cycle aging cells had an RPT every 50, 100, or 150 cycles, while calendar aging cells had an RPT approximately every 1-2 months. An RPT consisted of a C/3 CCCV charge, a hybrid pulse power characterization (HPPC) discharge, a C/20 CCCV charge, and a C/20 CC discharge. For the C/20 charge, the cutoff current was C/50. For this work, the capacity measured during the C/20 charge is reported as the aged cell capacity, C.

In each RPT, the SOC-dependent Ohmic resistance function, $R_s(z)$, was characterized from the HPPC. The HPPC consisted of repeating the following sequence until the minimum voltage limit of 2.8 V was reached: 1 hr discharge at 0.2 A (ΔSOC = 8% w.r.t. the nominal capacity); 15-min rest; 10 s charge pulse at 2 A; 5-min rest; 10 s discharge pulse at 2 A; and 5-min rest. Data during the pulses were recorded at a 10 Hz rate and 1 Hz otherwise. At each pulse, the short-duration Ohmic resistance, ($R_{0.4\text{s}}$) was calculated by using Ohm's Law, where the voltage difference ($\Delta V_{0.4\text{s}}$) was calculated using the average of the last four data points immediately before and after the pulse started. Similarly, the 10-second pulse resistance ($R_{10\text{s}}$) was calculated using the voltage difference for the entire pulse ($\Delta V_{10\text{s}}$) using the average of the last four data points before the pulse started and at the end of the 10 s pulse. These are illustrated in Fig. 5.1. The resistance at each pulse is then calculated as

$$R_s = R_{0.4\text{s}} = \frac{\Delta V_{0.4\text{s}}}{I_{\text{pulse}}} \quad \text{and} \quad R_{10\text{s}} = \frac{\Delta V_{10\text{s}}}{I_{\text{pulse}}} \tag{5.1}$$

where I_{pulse} is the pulse current.

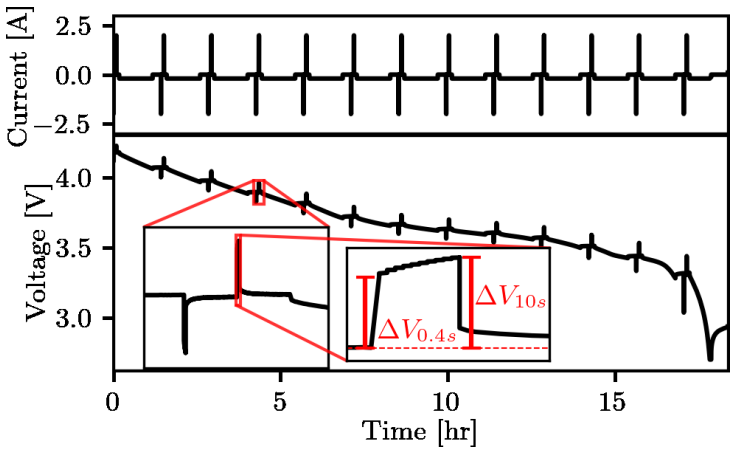


Figure 5.1: HPPC current and voltage profiles used to calculate $R_s = R_{0.4\text{s}}$ and $R_{10\text{s}}$. Each charge and discharge pulse is 10 s long at 2 A

5.2.2 Electrode open-circuit potential characterization

Coin cell half-cells were made for similar cells from a different manufacturing batch and used to characterize the OCP of the electrodes. The half-cell potentials for the positive and negative electrodes measured from a C/70 charge and discharge test were averaged and used as the electrode OCPs for this work.

5.3 Open-circuit voltage model

This section will summarize the full-cell open-circuit voltage (OCV) model, show that modeling electrode inhomogeneity can capture the peak smoothing effect for each electrode, and relate the parameters to the degradation modes.

5.3.1 Full-cell OCV model

Li-ion batteries with a lithium metal oxide ($LiMO_2$) PE and a graphite (C_6) NE will have intercalation reactions described by

$$\mathrm{Li_xC_6} \underset{\text{charge}}{\overset{\text{discharge}}{\rightleftharpoons}} x\mathrm{Li^+} + x\mathrm{e^-} + \mathrm{C_6}$$
$$\mathrm{Li_yMO_2} + (1-y)\mathrm{Li^+} + (1-y)\mathrm{e^-} \underset{\text{charge}}{\overset{\text{discharge}}{\rightleftharpoons}} \mathrm{LiMO_2},$$

where $x, y \in [0, 1]$ are the negative and positive electrode stoichiometries, respectively. The electrode utilization windows are defined as $x \in [x_0, x_{100}]$ and $y \in [y_{100}, y_0]$, where the subscripts 100 and 0 correspond to stoichiometries at 100% SOC and 0% SOC. The modeled cell OCV (V_{ocv}) is then calculated from the difference between the positive and negative electrode OCP, U_p and U_n, by

$$V_{\text{ocv}}(Q) = U_p(y) - U_n(x) \tag{5.2}$$

where

$$x = x_0 + \frac{Q}{C_n}, \qquad y = y_0 - \frac{Q}{C_p}. \tag{5.3}$$

The charge of the cell is Q, and the positive and negative cell capacities are C_p and C_n, respectively.

The nominal set of fitted parameters for the OCV model are

$$\theta_{\text{DVA}} = [C_n, x_0, C_p, y_0]. \tag{5.4}$$

Given θ_{DVA}, the upper bounds of the utilization windows are calculated as

$$x_{100} = x_0 + \frac{C}{C_n}, \qquad y_{100} = y_0 - \frac{C}{C_p}, \tag{5.5}$$

where the full cell capacity is C.

5.3.2 LLI and LAM degradation modes

The OCV model parameters, θ_{DVA}, can be used to quantify and track the main degradation modes, including Li inventory loss (LLI), loss of active material in the NE ($\mathrm{LAM_{NE}}$), and loss of active material in the PE ($\mathrm{LAM_{PE}}$) as well as the stoichiometric windows [109].

LLI captures the loss of cyclable Li from degradation mechanisms such as solid-electrolyte interphase (SEI) growth and Li plating. The total number of moles of intercalated lithium in both electrodes is calculated as

$$n_{\mathrm{Li}} = \frac{3600}{F}(x_0 C_p + y_0 C_n). \tag{5.6}$$

LLI is then defined relative to the fresh cell as

$$\mathrm{LLI} = 1 - \frac{n_{\mathrm{LI}}^{\mathrm{aged}}}{n_{\mathrm{LI}}^{\mathrm{fresh}}}. \tag{5.7}$$

LAM captures the loss of electrode mass available for Li intercalation due to degradation mechanisms such as particle cracking and loss of electrical contact. Similarly, LAM is defined relative to the fresh cell for the positive and negative electrodes, respectively, as

$$\mathrm{LAM}_p = 1 - \frac{C_p^{\mathrm{aged}}}{C_p^{\mathrm{fresh}}}, \quad \mathrm{LAM}_n = 1 - \frac{C_n^{\mathrm{aged}}}{C_n^{\mathrm{fresh}}}. \tag{5.8}$$

5.3.3 Modeling inhomogeneity in aged electrode OCP

To model the OCV for an aged cell, the OCP for an aged electrode, specifically the negative electrode, is used by incorporating inhomogeneity. In this work, we use a Gaussian distribution of electrode capacities (or equivalently LAM) to describe inhomogeneity and capture the peak smoothing effect observed in aged cells. Although previous work used linear distributions, their selection was based on sorting experimentally-derived LLI and was unable to explain regions with observed plating in subsequent post-mortem analysis [104, 105]. Our distribution selection is based on other works that describe inhomogeneity through Gaussian or binomial distributions, including work by Muller et al., which quantified the microstructural inhomogeneity of electrode properties with 3D imaging (i.e. porosity, tortuosity, particle size, and surface area) [23, 99, 100, 110]. We also only used a distribution to describe inhomogeneities within the NE and not the PE. When both were included, the parameter trajectories were overall noisier without a notable reduction in either voltage or DV error, suggesting that the model was overfitted to the data. For further details about the derivation of the aged electrode OCP model, we refer the reader to Kirst et al. [99] but

summarize the algorithmically relevant concepts here.

To build the model, we consider a global NE composed of a distribution of local NE components, each with corresponding capacities and OCPs. Within the electrode, the distribution of local negative electrode capacities, c_n, is described by a Gaussian probability density function

$$\begin{aligned} f_n(c_n) &= \mathcal{N}(c_n|\mu = C_n, \sigma = \sigma_{C_n}) \\ &= \frac{1}{\sigma_{C_n} \cdot \sqrt{2\Pi}} \exp\left[-\frac{1}{2}\left(\frac{c_n - C_n}{\sigma_{C_n}}\right)^2\right], \end{aligned} \tag{5.9}$$

where the mean capacity of the global NE is C_n. The corresponding standard deviation is σ_{C_n}, which we use to characterize inhomogeneity.

Averaged over the entire electrode, the global aged NE OCP is calculated as

$$U_n(x) = \int_{-\infty}^{\infty} f_n(c_n|\mu = C_n, \sigma = \sigma_{C_n}) U_n^0(x(Q)|_{c_n}) dc_n. \tag{5.10}$$

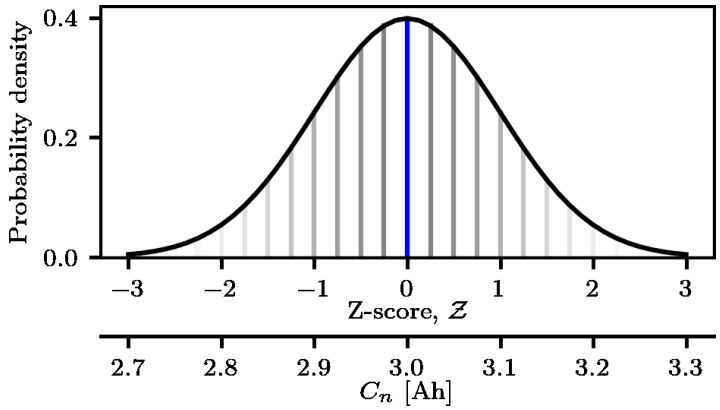
where $U_n^0(x(Q)|_{c_n})$ is the local electrode potential from Eq. 5.3 and U_n^0 is the fresh NE OCP.

Rather than simulating a continuous distribution of nonlinear functions, we discretize the Gaussian distribution within the z-score domain, $\mathcal{Z} \in [\mathcal{Z}_{\min}, \mathcal{Z}_{\max}]$ at intervals of $\Delta\mathcal{Z}$, to establish a representative subset of $c_{n,z}$. We then compute the corresponding $U_{n,z}^0(x(Q)|_{c_{n,z}})$ at each point and perform a weighted average over the entire distribution to represent the electrode. This is described by

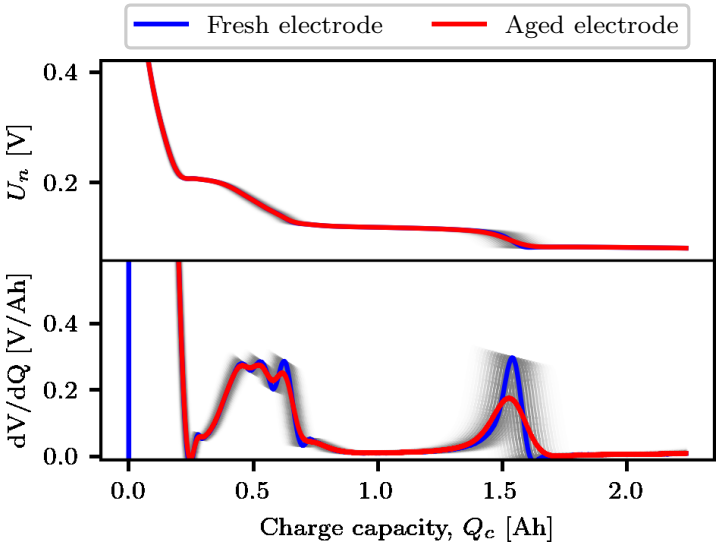
$$\begin{aligned} &U_n(x) = \frac{1}{\sum_i w_z} \sum_i w_z U_{n,z}^0(x(Q)|_{c_{n,z}}), \\ &\text{where} \\ &\qquad c_{n,z} = C_n + (\mathcal{Z}_{\min} + i\Delta\mathcal{Z})\sigma_{C_n} \\ &\qquad w_z = f_n(c_{n,z}). \end{aligned} \tag{5.11}$$

This process is illustrated for the negative electrode in Fig. 5.2 using $\mu = C_n = 3$ Ah and $\sigma_{C_n} = 0.1$ Ah. For $\mathcal{Z} \in [-3, 3]$ and $\Delta\mathcal{Z} = 0.25$, each $c_{n,z}$ and corresponding $U_{n,z}^0(x|c_{n,z})$ are plotted in grey in Figs. 5.2a and 5.2b, respectively, where the opacity is proportional to w_z. The resulting aged U_n with inhomogeneity is plotted in red. Compared to U_n^{fresh} (blue), note that the graphite peaks in the aged U_n are less pronounced, reproducing the DV peak smoothing.

Combined with Eq. 5.2, the relationship between the cell OCV, electrode OCPs, and



(a) Negative electrode capacity distribution from Eq. 5.9 with a mean capacity of $C_{n,0} = 3.0$ Ah and standard deviation of $\sigma_{C_n} = 0.1$ Ah



(b) Negative electrode OCP $U_n(Q_c)$ and corresponding differential potential $\frac{dU_n(C_n)}{dQ}$ without (blue) and with inhomogeneity (red).

Figure 5.2: Constructed aged negative electrode OCP. Assuming a normal distribution of C_n, $U_n(C_n)$ is calculated for each representative electrode over a range of z-scores in $\mathcal{N}(C_n, \sigma_{C_n})$ (grey), then a weighted average is calculated to model an aged electrode with inhomogeneity (red) where the weights are proportional to $f_n(C_{n,z})$ from Eq. 5.9. The opacity of each $c_{n,z}$ and $U_{n,z}^{\text{fresh}}(x|_{c_{n,z}})$ reflect the z-score and contribution to the inhomogeneous U_n. For comparison, the U_n^{fresh} is plotted in blue.

fitting parameters are then summarized by

$$V_{\text{ocv}}(Q) = U_p(y(Q)|_{C_p,y_0}) - U_n(x(Q)|_{C_n,x_0})|_{\sigma_{C_n}}, \tag{5.12}$$

where the only fitting parameter added to the original θ_{DVA} is the inhomogeneity of NE capacity, σ_{C_n}.

5.4 Model parameterization

The aged OCV model is parameterized at each RPT by first preprocessing the C/20 charge voltage data to approximate the thermodynamic OCV. Only the C/20 charge curve, and not the discharge curve, is considered since the peaks in the discharge curve are more susceptible to non-degradation-related factors [111]. Then, an optimization problem is formulated to find the set of model parameters that minimizes the error in voltage and differential voltage signals.

5.4.1 Data preprocessing

Before parameterizing the model, the voltage data is preprocessed to improve the data quality. First, a Savitzky–Golay filter with an equivalent window length of about 50 mins, or 4% SOC at a C-rate of C/20, is used to improve the signal-to-noise ratio in the measured voltage data, preserve the shape of the peaks, and calculate the derivatives of the signals. Then, a resistance correction is applied to better approximate the thermodynamic OCV. Here, we use the 10-second resistance at 50% SOC ($R_{10s}(z = 0.5)$) from the HPPC charge pulses to apply a constant offset. The processed voltage data used for fitting is then

$$V_{\text{data}} = \tilde{V}_{\text{data}} - I_{\text{data}} R_{10s}(z = 0.5), \tag{5.13}$$

where $\tilde{V}_{\text{data}}$ is the measured voltage; I_{data} is the measured current; and V_{data} is the filtered, resistance-corrected voltage.

5.4.2 Defining the optimization problem

To parameterize the model, an optimization problem is defined to find the set of parameters that minimizes the error in both the voltage and the differential voltage between the model and the data.The complete set of fitting parameters is

$$\theta = [C_n, x_0, C_p, y_0, \sigma_{C_n}]. \tag{5.14}$$

The `minimize` function from the SciPy Python package was used to solve the optimization problem with a Sequential Least Squares Programming (SLSQP) solver and a tolerance of

$1e^{-8}$ [112]. The objective function is the sum of the root mean square error (RMSE) of the voltage (RMSE_V) and the differential voltage (RMSE_{dVdQ}). Two inequality constraints are added to ensure that the stoichiometric values at x_{100} and y_{100} are valid. The optimization problem is then defined as

$$\begin{aligned}
\min_{\theta} \quad & J = \text{RMSE}_V + \text{RMSE}_{dVdQ} \\
& = \sqrt{\sum (V_{\text{model}}(\theta) - V_{\text{data}})^2} + \\
& \sqrt{\sum \left[\left(\frac{dV(\theta)}{dQ} \right)_{\text{model}} - \left(\frac{dV}{dQ} \right)_{\text{data}} \right]^2} \\
\text{subject to} \quad & \\
& \theta_{\text{lb}} \leq \theta \leq \theta_{\text{ub}} \\
& 0 < x_0 + \frac{C}{C_n} < 1 \\
& 0 < y_0 - \frac{C}{C_p} < 1.
\end{aligned} \tag{5.15}$$

To avoid biasing the objective function, we avoid calculating RMSE_{dVdQ} at low SOC and high SOC where the strong nonlinear behavior in U_n dominates. The SOC window is empirically determined by the DV features. Only when fitting the parameters, the RMSE_{dVdQ} is calculated for the SOC window corresponding to where $\left(\frac{dV}{dQ}\right)_{\text{data}}$ is between the maximum and minimum values of the highest peak and lowest trough, as illustrated in Fig. 5.3. This resulted in a low SOC cutoff ranging between about 5-15% SOC as the cells age and a high SOC cutoff above 95% SOC. If the peaks cannot be identified, then a default SOC window of 5-95% SOC is used. All subsequent RMSE_V and RMSE_{dVdQ} values reported in this study use the full SOC window.

5.4.2.1 Initial conditions

The initial guess (θ_0) for the model parameters at all RPTs after the first depend on the fitted parameters and model error of the previous RPT. The upper bounds (θ_{ub}) and lower bounds (θ_{lb}) of all but σ_{C_n} do not. At the beginning of life (BOL), the initial guess is θ_0^{BOL}. After the first RPT, initial guesses for RPT k for k$\in \{2, 3, 4...\}$ are equal to the fitted parameters of the last RPT $\theta_0^{\text{k}-1}$ with low error ($\text{RMSE}_V < 20$ mV or $\text{RMSE}_{dVdQ} < 200$ mV/Ah). The error thresholds were empirically determined to ignore RPTs with incomplete or corrupted DV data.

To refine the initial estimates for the negative electrode parameters, the DV peaks originating from U_n are leveraged by identifying approximate locations in Q, as illustrated in

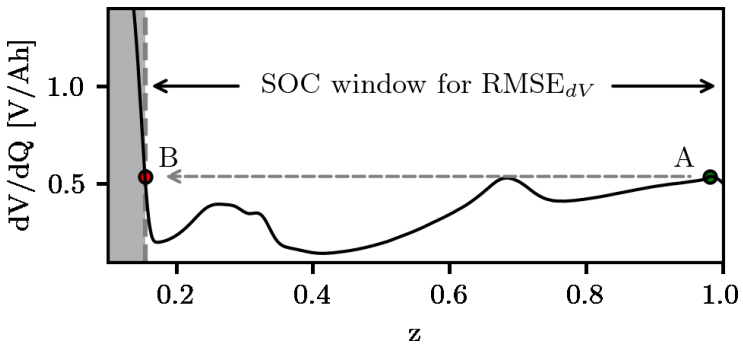


Figure 5.3: Parameterization SOC window for calculating RMSE$_{dV\,dQ}$ (Eq. 5.15). The location of the next highest peak in the data (Point A) determines the threshold and corresponding minimum SOC (Point B). In this example, data in the shaded low SOC region is ignored.

Fig. 5.4 [109]. If there are identifiable peaks in the full cell DV data that can be matched to the corresponding peaks for the fresh NE, then we can estimate the NE model parameters as

$$\hat{C}_n = \frac{\hat{Q}_b - \hat{Q}_a}{\hat{x}_b - \hat{x}_a}, \quad \hat{x}_0 = \hat{x}_b - \frac{\hat{Q}_b}{\hat{C}_n} \tag{5.16}$$

where the pairs ($\hat{x}_a$, $\hat{Q}_a$) and ($\hat{x}_b$, $\hat{Q}_a$) are the locations of the peaks in the respective DV curves corresponding to the graphite phase stage 2 transition and stage 3L, respectively [113, 114]. However, if the peaks become too difficult to identify as the cells age, the fitted NE parameters from the previous RPT are used as initial conditions.

5.4.2.2 Parameter bounds

The lower and upper bounds are mostly static except for the lower bound on σ_{Cn}. This is used to avoid deviating to less optimal and transient local minima as the cell ages. We assume that the change in σ_{Cn} between RPTs is captured within these constraints. The bounds and initial guess at BOL are summarized in Table 5.2.

5.5 Results and discussion

The experimental and modeling results are summarized below.

5.5.1 Experimental results

The degradation patterns are similar to those previously reported for capacity loss and resistance growth with respect to temperature and C-rate [97]. Additionally, within each

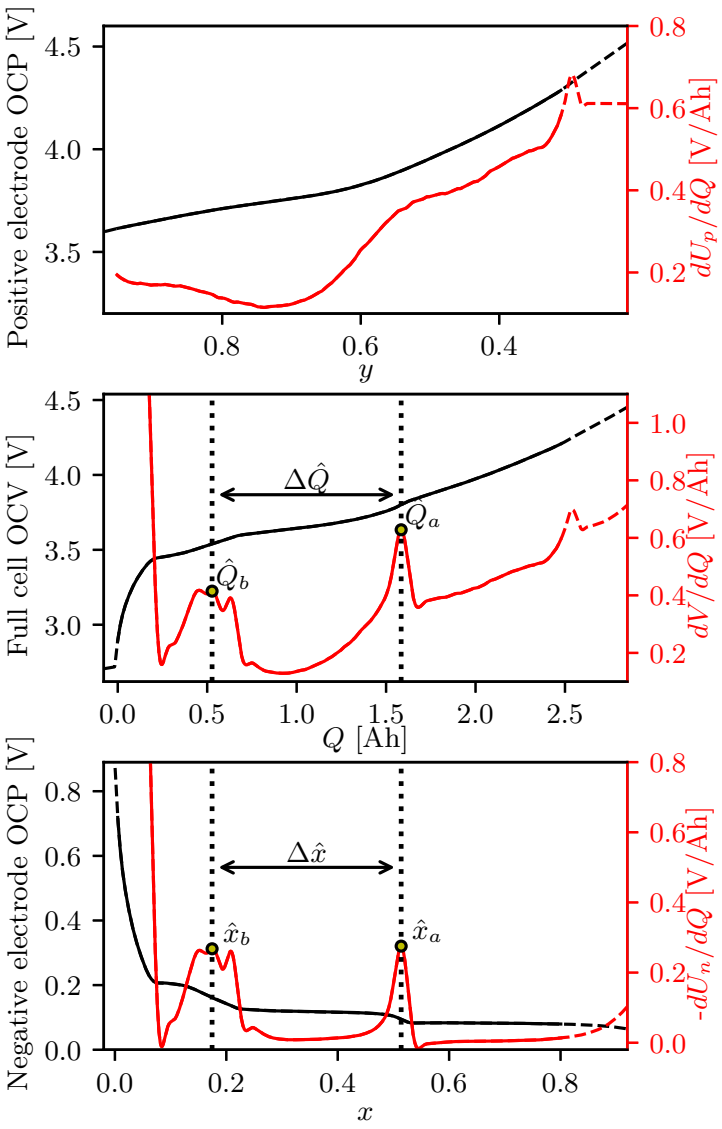


Figure 5.4: The peaks observed in the full cell DV are attributed to $\frac{dU_n}{dQ}$ and are used to initialize negative electrode parameters. The voltage (black) and DV (red) signals for the PE (top), full cell (middle), and NE (bottom) are plotted to illustrate the alignment of the transition peaks.

Table 5.2: Summary of initial conditions, upper bounds, and lower bounds for model parameterization

Parameter	θ_0^{BOL}	$\theta_{\text{lb}}^{\text{min}}$	$\theta_{\text{ub}}^{\text{max}}$
C_n [Ah]	3	1	5
x_0	0	0	1
C_p [Ah]	4	1	5
y_0	1	0	1
σ_{C_n} [Ah]	0	$\max(0, 0.5\sigma_{C_n}^{k-1})$	1

set of cycling conditions, the aging trajectories of each cell agree well with each other. To compare capacity retention across different cycling conditions, we use equivalent full cycle (EFC), which is calculated as the sum of the charge and discharge Ah throughput normalized to the nominal capacity of 2.5 Ah. Furthermore, $R_s(z = 0.5)$ is calculated with respect to the aged cell capacity and is used to represent and track resistance growth, as shown in Fig. 5.5.

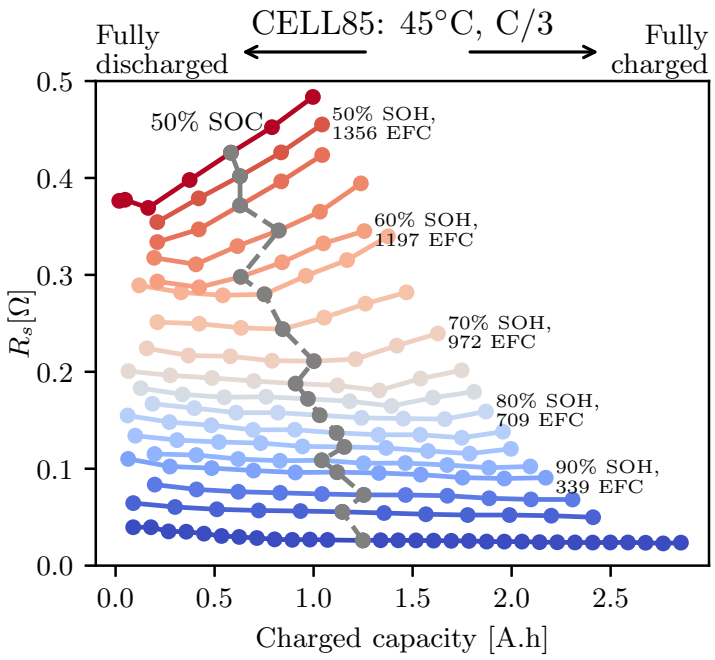


Figure 5.5: Evolution of R_s charge pulse resistance versus Q with degradation

The capacity loss and resistance growth trajectories are shown in Fig. 5.6a for all cells. Calendar-aged cells are plotted using an axes scaling of 4 C/3 cycles per day. In the BOL, the initial cell capacities were between 2.51-2.55 Ah, or <2% above the designed nominal

capacity (Q_{nom}) before aging.

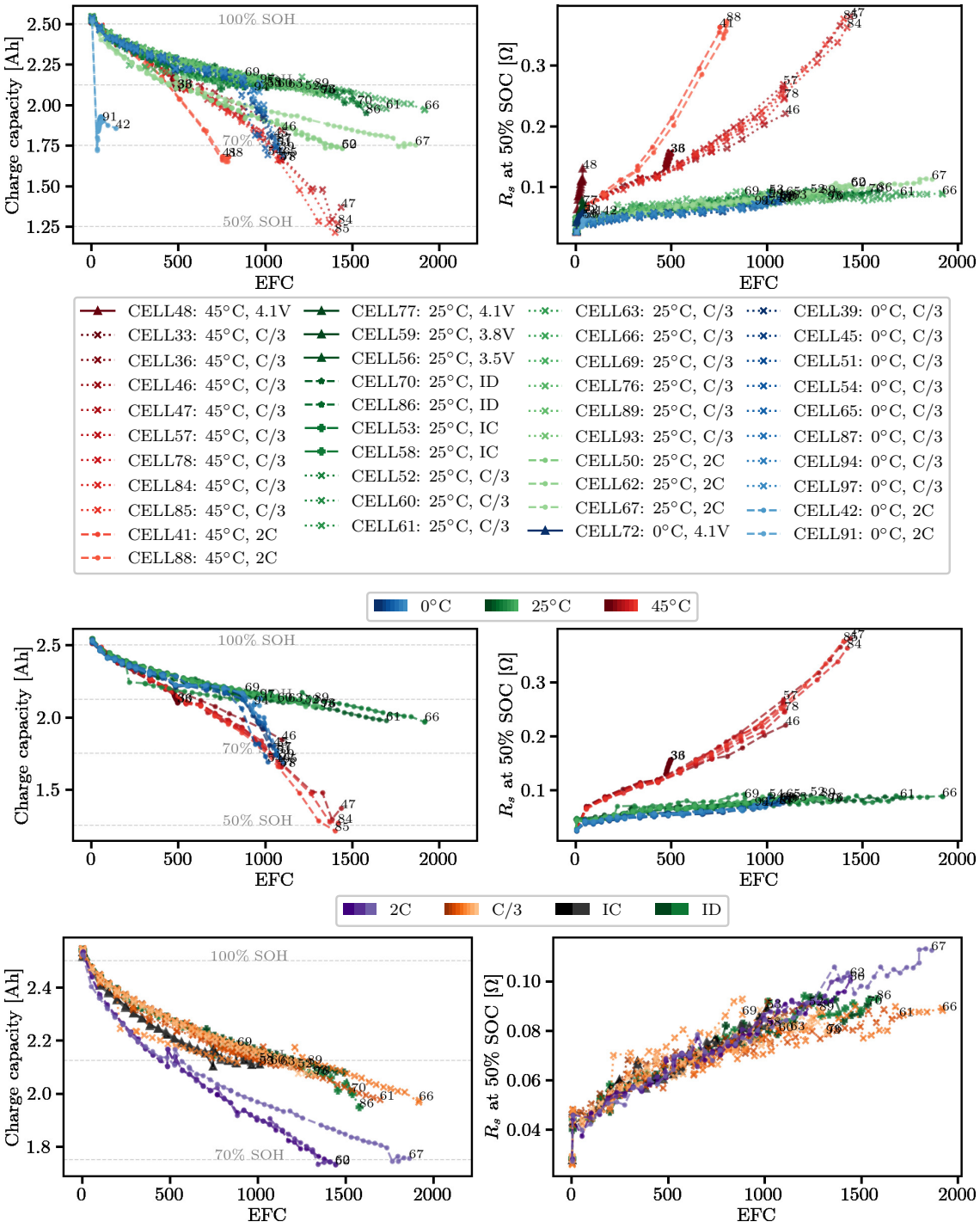


Figure 5.6: Capacity loss (left) and resistance growth (right) for (a) cycle-aged cells, (b) only C/3 cycle-aged cells to show the effect of temperature, and (c) only RT-aged cells to show the effect of C-rate. The $R_{0.4s}$ at 50% SOC, where SOC is calculated relative to the aged cell.

To examine the effect of temperature, the capacity loss and resistance growth trajectories are compared for the C/3-cycled cells (Fig. 5.6b). Overall, cold- and hot-temperature cells had the fastest capacity loss, but the "knee" behavior in capacity retention are notably different. The "knee" describes a transition to a faster or accelerated degradation rate, suggesting a shift in the dominant degradation mechanism [97]. Specifically, the trajectory of the cold-temperature cells shows a very sudden onset of the knee, whereas the hot-temperature cells show a more gradual one. Due to the sudden knee in the cold-temperature cells, both cold- and hot-temperature cells reach 70% SOH after similar Ah throughput, 1000±50 EFC and 1050±50 EFC, respectively. Before the knee, the capacity and resistance trajectories between the cold- and room-temperature cells are almost indistinguishable. Similar trends were observed in resistance growth. Cells aged at 45°C had the most resistance growth overall, where at 70% SOH these cells developed more than twice the internal resistance of the cells cycling at lower temperatures. Between cold- and room-temperature cells, resistance growth is comparable even after the knee occurs in cold-temperature cells.

To examine the effects of cycling at different C-rates and calendar aging at different voltages, the trajectories of capacity loss and resistance growth are compared for cells cycled at 25°C (Fig. 5.6c). The patterns in both are consistent with the literature. Overall, cycling at more aggressive C-rates leads to faster capacity loss. Comparing the C/3 cells and ID cells which spent 20% of the time during discharge at 2C, the trajectories are very similar in both capacity and resistance. However for the IC cell, the trajectory begins to diverge from the C/3 trajectory early on towards that for the 2C cells, but reconverges. This behavior can be explained by a gradual decrease in the time spent at 2C during charging as the internal resistance of the cells increase. For calendar aging cells, spending time at higher voltages leads to faster capacity loss and resistance growth. However, the difference is larger between the cells aged at 4.1 V (Cell 77) and 3.8 V (Cell 59) than between 3.8 V (Cell 59) and 4.5 V (Cell 56).

In general, cells cycled at 2C experienced the fastest capacity loss at each temperature; however, cells cycled at 2C and 0°C experienced extremely rapid capacity loss, reaching 70% SOH within 50 cycles. This is likely due to severe Li plating [97]. Afterwards, they continued to rest and calendar age at the prescribed temperature with occasional RPTs leading to capacity recovery. Cell 42 restarted cycling after resting for 2 years, while Cell 91 continued to rest to recover more of the initial capacity loss. After restarting cycling at 2C, the capacity of Cell 42 continued to decrease but at a much slower rate than during the initial cycling. For both cells, the internal resistance continued to increase even as the capacity recovered.

5.5.2 Characterization and modeling results

To better understand the underlying mechanisms that drive the capacity loss and resistance growth behaviors, we first validate that the parameterized model can capture the expected DV behavior for aged cells. Then, we use the model to characterize the degradation modes across aging conditions.

Qualitative and quantitative comparisons of the measured and modeled DV curves show that, in general, the model is able to capture the evolution of the peak smoothing behavior for aged cells, even after the peak corresponding to the Stage 2 transition, or high-SOC peak, in the DV is no longer observable in the data. Using one of the most aged cells as an example, the modeled and measured voltage and DV signals for Cell 85 (45°C, C/3) are plotted in Fig. 5.7 for select RPTs ranging from fresh to 50% SOH. As the cell ages, the DV peak smoothing behavior can be seen in both the high-SOC peak and the set of peaks corresponding to the Stage 2L-4L transitions, or low-SOC peaks, where they both show general trends of decreasing height and increasing width with age. In addition, the low-SOC peaks gradually blend into a single monolithic. Simultaneously, the high-SOC peak continues to decay until it is no longer observable, which is after about 70% SOH for Cell 85. For reference, the model errors are at most 5 mV for RMSE_{V} and 17 mV/Ah for RMSE_{dV}.

The dominant degradation mode for all cells was LAM_{NE} and LLI, followed by LAM_{PE}. Fig. 5.8 shows the fitted degradation modes for cycle-aged cells. Throughout the cycle life of all cells, the model errors remained low for both RMSE_{V} and $\text{RMSE}_{\text{dVdQ}}$, indicating that the model was able to accurately capture the evolution of OCV and DV as the cells aged. However, for hot-temperature, 2C-aged cells, C_p began to increase after approximately 15% capacity loss, leading to a decrease in LAM_{PE} that may not be physical. Although RMSE_{V} remains low, the large increase in $\text{RMSE}_{\text{dVdQ}}$ suggests a potential limitation that should be investigated further.

To examine the effect of temperature, the evolution of degradation modes and inhomogeneity are compared for the C/3-cycled cells (Fig. 5.8a). Initially, cold- and room-temperature cells show very similar sublinear trajectories across all degradation modes, while hot-temperature cells show a faster, more linear degradation trajectory. When the knee occurs, cold-temperature cells exhibited a marked increase in LLI, inhomogeneity, and LAM_{NE}, as opposed to the hot-temperature cells which experienced a more gradual acceleration of these degradation modes after about 1000 EFCs. Furthermore, while room- and cold-temperature cells had similar trajectories in almost all degradation metrics before the knee, cold-temperature cells developed twice the inhomogeneity in the same number of EFCs compared to room-temperature cells. For cold and hot cells, RMSE_{V} and $\text{RMSE}_{d}VdQ$ both increase toward the EOL, but the errors generally remain low. In all except for the cold,

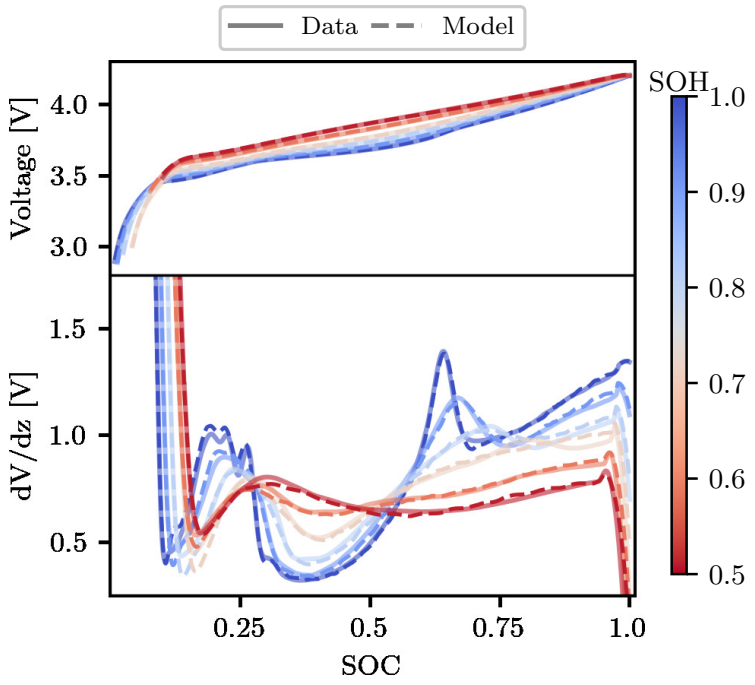


Figure 5.7: Comparison of measured and modeled voltage and differential voltage of Cell 85 (45°C, C/3) from fresh to 50% SOH

2C-cycled cells, σ_{C_n}, LLI, and LAM_{NE} increase simultaneously.

Furthermore, the effect of C-rates can be compared for cells cycled at room-temperature. In general, similar trends are observed for LLI and LAM_{NE} as for full cell capacity. Cycling at higher C-rates leads to faster degradation of both. The trajectories for IC-cycled cells eventually converge with C/3-cycled cells as the 2C-charge portion of the protocol decreases with continued cycling. LAM_{NE} and σ_{C_n} do not show appreciable differences between the C-rate conditions.

5.5.3 Temperature-dependence of inhomogeneity growth

Inhomogeneity trajectories are expected to differ with temperature because the underlying degradation mechanisms do. To better interpret inhomogeneity growth, we can look at the temperature dependence between C/3-aged cells with respect to other LLI, LAM, and resistance growth. These relationships are plotted in Fig. 5.9. In general, the trends support the presence of previously reported degradation mechanisms observed in the literature for cells cycled under comparable aging conditions.

For the cold, C/3-aged cells, the sudden onset of inhomogeneity growth for a relatively small amount of Li ($\Delta\text{LLI} = 0.04$), as shown in Fig. 5.9a, suggests the onset of inhomogeneous

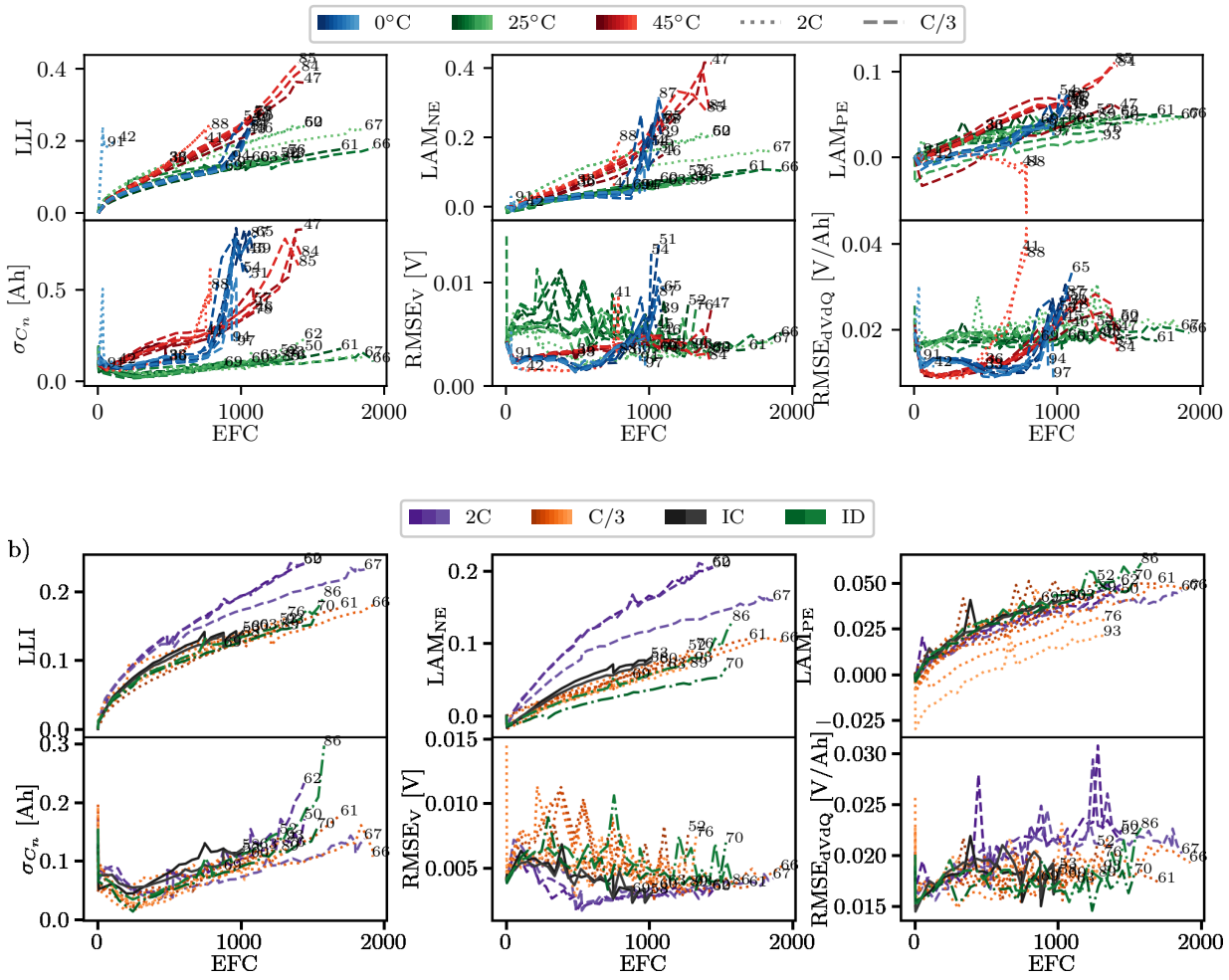


Figure 5.8: Parameterized degradation modes for all cycle-aged cells for (a) C/3 and 2C cycle-aged cells to show the effect of temperature and (b) only room-temperature cells to show the effect of C-rate.

Li plating and corresponds to the knee in capacity. This is consistent with previous works that attribute accelerated degradation and inhomogeneity growth to Li plating [96, 102, 104, 110]. This onset of plating is simultaneously accompanied by $\mathrm{LAM_{NE}}$ ($\Delta\mathrm{LAM_{NE}} = 0.1$) with a negligible change to $\mathrm{LAM_{PE}}$ and R_s (Figs. 5.9b-5.9d). After the sharp increase, more LLI, $\mathrm{LAM_{NE}}$, and $\mathrm{LAM_{PE}}$ occur without a distinct change in inhomogeneity. The results suggests that a subset experience mild recovery in σ_{C_n} but not LLI, while others see continued growth at a rate comparable to before the knee.

For the hot, C/3-aged cells, the knee occurs more gradually. In this case, we suspect Li plating may have occurred due to electrode saturation, which occurs during charging when all accessible intercalation sites in the NE are occupied, causing excess lithium to plate

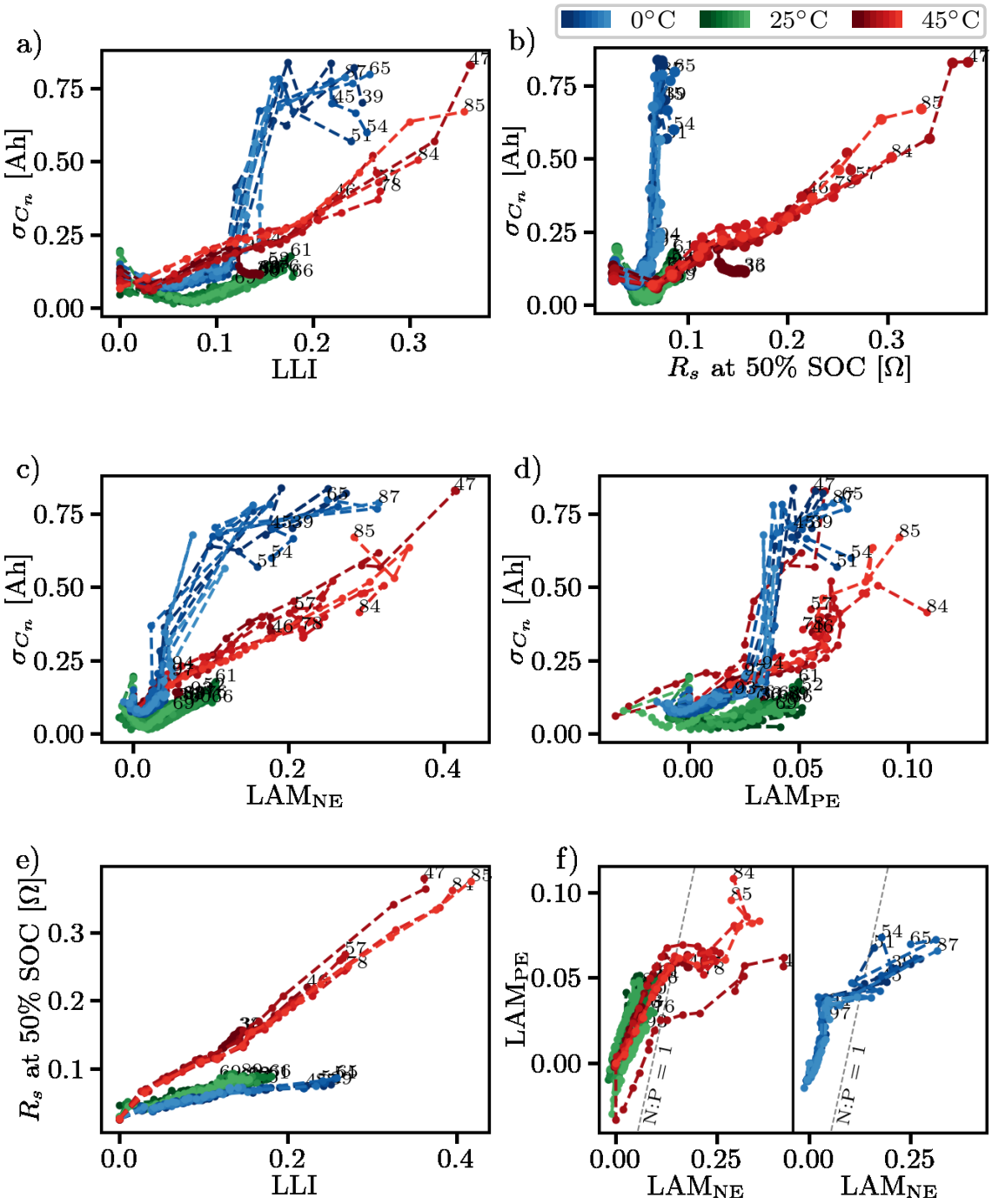


Figure 5.9: Relationships between σ_{C_n}, R_s, LAM, and LLI for C/3 cycle aging cells show distinct trajectories for cold- and hot-temperature cells.

on the surface instead of being intercalated into the anode structure. Electrode saturation causes rate-independent lithium plating and a subsequent knee [97]. This can occur when the ratio of NE and PE capacity, or N:P ratio, is less than one (Fig. 5.9f), leading to faster

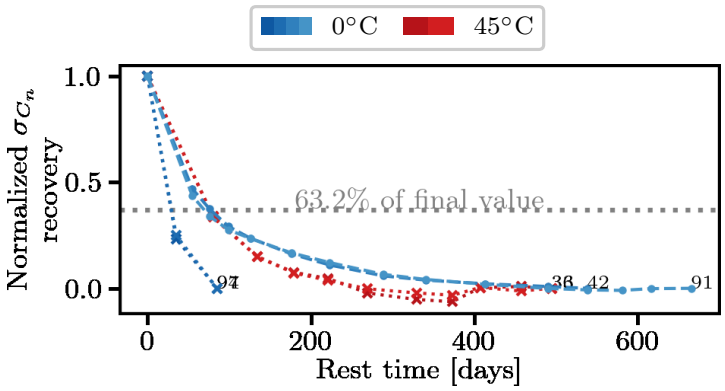


Figure 5.10: Recovery of inhomogeneity while resting after cycling. Values of σ_{C_n} are normalized between the last RPT before resting and the last available RPT, assuming the process is at quasi-steady state.

LAM_{NE} than LAM_{PE}. The LAM_{NE}: LLI ratio is another metric previously identified to show electrode saturation [115]. Accelerated LAM_{NE} also occurs in cold-temperature cells, but much earlier before the crossover. However, unlike cold-temperature cells, the change in σ_{C_n} due to plating is effectively unobservable due to a more persistent and dominant mechanism. This may be due to other more dominant mechanisms that are exacerbated at higher temperatures, lead to higher Ohmic resistances, and asymmetrically favor the NE. These may include SEI growth and electrolyte decomposition that can lead to pore clogging and growth of the cover layer, as previously observed [97, 116, 117].

Focusing on inhomogeneity, σ_{C_n} generally increases with the number of EFCs but can decrease for a couple of reasons. Recovery of inhomogeneity may partially result from reintercalation of plated lithium in the graphite anode, with reported timescales ranging from <1 day to two weeks at room temperature [118]. This likely occurred in the cold, 2C-aged cells during the first two-week rest period, which saw a simultaneous 6-8% recovery of the LLI initially lost during the first 50 cycles. Inhomogeneity recovery can also occur due to the passive electrode effect, where lithium within the electrode can diffuse laterally over long timescales from passive electrode regions, including the anode overhang at the BOL or areas obstructed by a dense cover layer after cycling [119]. The passive electrode effect is slow because of long diffusion lengths. Assuming a first-order process and steady-state conditions in the last RPT, the time constant (τ) of the observed inhomogeneity recovery process is approximately 75 days for both hot- and cold-temperature cells, or 375 days to reach 99% saturation (5τ), which is more similar to the 120-300 days reported by Lewerenz et al. [120].

5.5.4 Relating degradation modes to SEI decomposition

We consider how the degradation modes characterized through the proposed SOH diagnostics algorithm can reduce the parameter uncertainty in the venting model discussed in Chapter 4. With a few assumptions, the LLI due to SEI can at least be bounded. Known causes of LLI include SEI growth, electrolyte decomposition, Li plating, and LLI due to LAM [101, 121]. This can be summarized as

$$\mathrm{LLI} = \mathrm{LLI}_{\mathrm{SEI}} + \mathrm{LLI}_{\mathrm{plating}} + \mathrm{LLI}_{\mathrm{LAM}}, \tag{5.17}$$

where for the purposes of this discussion, LLI that results from decomposition mechanisms that result in SEI-like products during aging is referred to as $\mathrm{LLI}_{\mathrm{SEI}}$ [96, 101, 121]. LLI due to Li plating is $\mathrm{LLI}_{\mathrm{plating}}$. LLI due to Li trapped in lost active material (e.g., particle cracking, delamination, cover layer growth, etc.) is $\mathrm{LLI}_{\mathrm{LAM}}$. Furthermore, $\mathrm{LLI}_{\mathrm{LAM}}$ can be calculated for the most extreme case assuming LAM occurs when the active material is full. The maximum contribution from $\mathrm{LLI}_{\mathrm{LAM}}$ can then be calculated as

$$\mathrm{LLI}_{\mathrm{LAM}}^{100} = x_{100}\mathrm{LAM}_{\mathrm{NE}} + y_0\mathrm{LAM}_{\mathrm{PE}}. \tag{5.18}$$

In the context of higher temperature SEI decomposition reactions, the initial state, $x_{\mathrm{SEI},0}$, representing the mole fraction of Li in the SEI to total negative electrode active material [74] can be calculated as

$$x_{\mathrm{SEI},0} = \mathrm{LLI}_{\mathrm{SEI}} + \mathrm{LLI}_{\mathrm{SEI}}^{0}, \tag{5.19}$$

where $\mathrm{LLI}_{\mathrm{SEI}}^{0}$ is the fraction of lithium consumed during formation at the end of the manufacturing process to develop the initial fresh cell SEI layer.

The parameter $x_{\mathrm{SEI},0}$ can then be bounded by assuming at most, all of the LLI is due to SEI. If $\mathrm{LLI}_{\mathrm{plating}} = 0$, which is a reasonable assumption for cell cycled at high temperature before accelerated degradation occurs, then

$$[(\mathrm{LLI} - (x_{100}\mathrm{LAM}_{\mathrm{NE}} + y_0\mathrm{LAM}_{\mathrm{PE}})] + \mathrm{LLI}_{\mathrm{SEI}}^{0} < x_{\mathrm{SEI},0} < \mathrm{LLI} + \mathrm{LLI}_{\mathrm{SEI}}^{0}. \tag{5.20}$$

While this is explicitly calculated for a limited case, more in-depth, physics-based modeling of the degradation mechanisms should be considered to separate the contribution from $\mathrm{LLI}_{\mathrm{SEI}}$ and $\mathrm{LLI}_{\mathrm{plating}}$ [60]. Furthermore, by modeling Li plating, the plating energy can be calculated to potentially predict the SEI decomposition kinetic parameters through experimentally derived correlations [46].

5.5.5 Comparing model complexity and performance

Using the same post-processed voltage data, we compare the model errors between this model and the next simplest model to justify the increase in model complexity wtih improved model performance. The model in this work (V+DV+σ) is compared to the conventional voltage fitting (VF) approach that only minimizes RMSE_V in the objective function (Eq. 5.15) and does not account for inhomogeneity ($\sigma_{C_n} = 0$). Additionally, we consider the case where both voltage and DV errors are minimized (V+DV) to control for the addition of RMSE_{dVdQ} and isolate the effect of modeling inhomogeneity.

In general, the algorithm introduced in this work maintains a consistently low error as cells age. This comes from comparing median error values across all RPTs where solutions are found by all three algorithms. RMSE_V and RMSE_{dVdQ} are plotted in Fig. 5.11, where each set of violins represents the errors of RPTs performed in the corresponding 10% capacity loss window. Initially, there is a noticeable trade-off between minimizing RMSE_V and RMSE_{dVdQ}. The median error and variability in RMSE_V are higher early in life for algorithms that account for RMSE_{dVdQ}, but the RMSE_{dVdQ} is also lower compared to that of VF. As cells age, all algorithms maintain a low median RMSE_V, but the median RMSE_{dVdQ} for the VF and V+DV algorithms increase threefold from about 20 mV/Ah to 60 mV/Ah after 30 % capacity loss, while that of the V+DV+σ algorithm remains at about 20 mV/Ah. In general, all three algorithms have relatively low voltage errors with almost all RMSE_V<10 mV throughout life.

5.6 Summary

In this study, we demonstrate how inhomogeneity can be considered as a distinct degradation mode by showing that it can be parameterized under a variety of aging conditions and is interpretable alongside other degradation modes. We show that coupling a DVA algorithm with a negative electrode OCP derived from a distribution of electrode capacity is capable of capturing the peak smoothing effect in aged cells with as much as 50% capacity loss. We then discuss the evolution of the degradation modes with respect to aging temperature and safety-related SEI decomposition parameters. Finally, we justified the increased model complexity by comparing the error in DV models with and without the inclusion of inhomogeneity, demonstrating a significant reduction in DV error as cells age. Although our analyses provide evidence to support the presence of specific degradation mechanisms, future postmortem teardown analyses and characterization tests are needed to verify the degradation mechanisms.

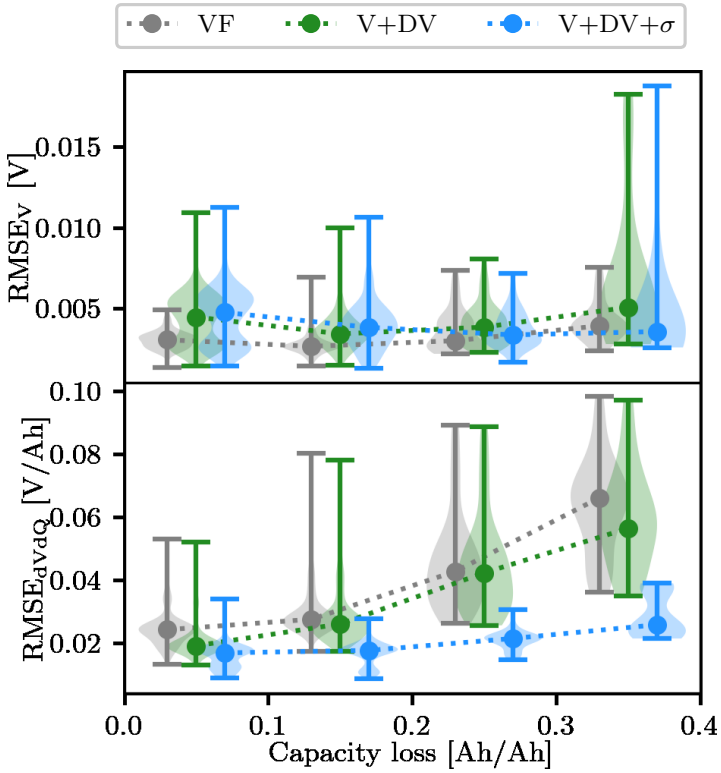


Figure 5.11: Comparison of error metrics across SOH to illustrate the impact of adding differential voltage error (V+DV) to the loss function and σ_k parameter to θ (V+DV+σ) compared to conventional voltage fitting (VF). Each set of violin plots represents the distribution of error across all cells within the respective 10% capacity loss window. The median of each distribution is indicated with a dot, while the bars indicate the extrema.

CHAPTER 6

Conclusion

6.1 Summary of contributions

With the widespread adoption of LIB systems, it is necessary to improve early failure detection, hazard mitigation, and prevention of fire reignition to manage TR and TR propagation. Although modeling can enable adaptive BMS algorithms to address these, their success relies on having models that can capture normal and early failure behaviors and depend on factors like model accuracy and computational complexity.

This dissertation addresses these challenges by highlighting the opportunity to adapt existing LIB models to predict battery behavior across a broader range of operation, from normal to early failure conditions, by augmenting them with minimal additional parameters and physics. In this context, control-oriented models can offer insight into long-term LIB behavior, be used to develop early detection with multi-modal sensor fusion and mitigation strategies, and improve related algorithms. This work develops two reduced-order multi-physics models to simulate the electrical, thermal, gas generation, and venting behaviors of LIB pouch cells under high temperature and high C-rate discharge conditions. Depending on the priority between computational efficiency and predictive capability to transition between normal and abnormal behavior, either the EqCM or SPMe can be used as the electrical model.

An electro-thermo-mechanical model was developed using an EqCM, adapted by incorporating two parameters to increase the time constant and capture the overall voltage decay during an ESC. These parameters were fitted with data from a single ESC experiment from one cell and validated on other cells at different initial SOC. The error in the final SOC after a 10-min ESC is at most 6.5% SOC. This model was also coupled with a zero-dimensional thermal model and a pouch venting model to simulate the rise in temperature and expansion force during an ESC, where the mechanical pouch venting model captures the two-stage expansion pressure from material expansion and gas generation. Then, a model predictive

controller was developed that can rapidly discharge a fully-charged cell down to 60% SOC in 2.5 mins before reducing the current to prevent venting. The simulation results indicate that incorporating pressure with high-temperature constraints enables a fast discharge while avoiding the increased fire hazards associated with first venting.

Then, to enable the transition between normal and abnormal electrical behavior, the electrical submodel was substituted for a reduced-order, physics-based SPMe. Initially parameterized from a prior aging study, the SPMe was adapted to include concentration-dependent diffusion parameters, which were parameterized using data from a characterization test under normal operation. This enabled the SPMe to capture the diffusion-limited discharge behavior during ESCs, whereas the EqCM only captured the overall decay after fitting additional parameters to the ESC data. This illustrated the improved predictive capability to transition between normal and abnormal behavior, but requires significantly more internal states depending on the spatial discretization compared to the two required by the EqCM. When integrated with thermal and pouch cell venting models, this multiphysics model was also able to predict whether gas expansion and venting would occur and predict venting within about 10 s of it occurring in experiments.

Following these model results, a global sensitivity analysis of the pouch cell venting model was presented to identify key parameters that affect cell expansion under various temperature and aging conditions. These were parameters related to preload, SEI decomposition, and thermal-dependence of foam stiffness. By varying these parameters, potential long-term challenges for expansion force-based algorithms were identified, including reduced gas expansion observability with increased preload pressure and the influence of temperature-dependent stiffness on sensitivity to abnormal active material thermal expansion, which were partially demonstrated in recent experimental studies with prismatic cells. The significant variability in expansion and vent timing due to aging-related uncertainty in the SEI decomposition reaction parameters underscores the need for further research into quantifying the relationship between cell degradation, i.e., modes and mechanisms that can be characterized during the lifetime, and their effect on SEI decomposition and gas generation.

The study considers cell inhomogeneity as an additional degradation mode that can be characterized by augmenting a DVA algorithm with a model of an aged cell's OCP. The study quantifies inhomogeneity in cells aged under various temperature and C-rate conditions with up to 50% capacity loss. The findings indicate that accounting for inhomogeneity significantly reduces error in DV as cells age and shows that inhomogeneity evolves differently in cells aged at different temperatures, despite similar cycling profiles. Cells cycled at cold temperatures experienced a sudden loss of capacity, LLI, and homogeneity. In contrast, cells cycled at high temperatures showed a faster but more consistent rate of loss in addition

to significant resistance growth. Characterizing inhomogeneity combined with other degradation modes offers deeper insights and corroborates previous findings about the causes of accelerated capacity loss. With a few assumptions, characterizing degradation modes can provide informed bounds on LLI due to SEI for the gas generation model. Future research on the connection between parameters identified through SOH diagnostics and those related to SEI quality and gas generation can enhance robust, aging-aware detection and mitigation strategies.

6.2 Future work and open challenges

The practical implementation of the LIB modeling work presented in this dissertation offers challenges and opportunities similar to those in adjacent areas of interest. These involve improving the field-parameterizability, scalability, and computational efficiency of LIB models for BMSs and sparse instrumentation in large systems.

6.2.1 Implementation of model-based algorithms for battery management systems

One key aspect is the ability to parameterize models during normal operation throughout life, which is important for developing accurate and adaptable detection and mitigation control algorithms. While there are still significant challenges, the capability is becoming increasingly feasible due to parallel advancements that will improve model accuracy and scalability:

- **Digital twins:** Having detailed, physics-based models can enable long-term tracking of deeper internal battery states to predict aging trajectories through SOH diagnostics with field data. This adaptability and insight can improve monitoring, control, and optimization of battery performance, leading to more effective and reliable BMS strategies.
- **Cloud and edge computing:** Advanced computing can improve the speed and efficiency of analyzing large data sets generated by LIB systems and processing model updates and predictions. Cloud computing provides access to extensive computational resources, while edge computing facilitates real-time data processing close to the source. Together, these can reduce the burden on onboard computers.

Once the nominal models are implemented in BMSs for standard model-based algorithms, such as SOC, SOH, and temperature estimation, implementing the parametric adaptations

(e.g. modified diffusion parameters in the EqCM and SPMe) and coupling the one-state pouch cell venting model becomes trivial. These may marginally decrease computational efficiency, if at all, while expanding the range of applications for the nominal models to include early failure detection and mitigation control. Future work may also consider implementing higher-dimensional thermal models to better model the thermal spatial distribution for large prismatic cells. For the pouch cells in the ESC experiments, the surface temperature measured at the edge of the pouch cell between the tabs was generally a few degrees lower than at the center (Appendix A). However, this will increase the computational demand, depending on the discretization.

6.2.2 Relating degradation pathways to failure behavior

To properly incorporate the effect of aging into a model of early failure behavior, we need to better understand how LIB failure behaviors are influenced by degradation mechanisms and how degradation mechanisms are captured by the parameters estimated during life (e.g., degradation modes). Although the passivation properties and composition of SEI are complex, the models presented here rely only on effective or lumped values related to their quantity (i.e. x_{SEI}) and quality (i.e. A_{SEI} and $E_{a,\text{SEI}}$) for thermal decomposition, making the gap more straightforward to address. One approach may be to rely on advanced physics-based degradation models that capture the evolution of long-timescale degradation states. Specifically, it can be used to provide more accurate estimates of the initial LLI due to SEI before failure occurs in aged cells. Furthermore, modeling and quantifying the Li plating energy can be used to potentially predict the SEI decomposition kinetic parameters through experimentally derived correlations [46].

Postmortem teardown analysis and imaging of the aged cells can be complementary by providing empirical evidence to validate the degradation mechanisms that were modeled and may help explain any discrepancies. In addition, it may also help provide more insight into trends in battery abuse tests related to, for example, exothermic heat generation, cell expansion, and gas composition at different stages. Future work may include combining these methodologies to thoroughly investigate and eventually model the relationship between degradation and failure behavior.

6.2.3 Instrumentation in large systems

The development of most novel BMS algorithms, including early detection and discharge mitigation, requires relevant temperature, gas, and expansion sensor measurements that are typically either sparse or non-existent in existing commercial systems. Thermocouples tend

to be fairly sparse in LIB systems as they are placed to monitor thermal gradients within the pack for general thermal management, resulting in low observability of individual cell temperature. Gas concentration sensors are used for BESSs and are being considered for commercial EVs, but are costly to integrate, and successful detection relies on location and air flow. Expansion force sensors are only relevant for prismatic and pouch cells, and instrumentation in large battery packs can be complex and costly. Overall, further development is needed to create economical and scalable sensors that can better balance safety with cost considerations. Meanwhile, future work should focus on improving control algorithms to enhance resource efficiency. This involves quantifying trade-offs and justifying the additional cost of sensors by demonstrating their contribution to long-term safety performance.

6.2.4 Early failure detection algorithms

Early detection algorithms facilitated by multiphysics modeling will be more responsive, accurate, and reliable than conventional static threshold-based detection methods by implementing model-based techniques, including multi-modal sensor fusion and adaptive thresholds [19, 21]. Multi-modal sensor fusion integrates data from different types of sensors, which will help improve detection accuracy by compensating for the weaknesses of individual sensors and provide a more comprehensive understanding of the status of LIB systems [19, 21, 94, 122]. For example, sensor fusion may involve weighted averaging of signals based on accuracy or reliability to account for sensing issues like cross-sensitivities, latency, or long-term drift. Using a model that captures electrical, thermal, and mechanical behavior, like the ones presented, can help determine uncertainty due to noisy sensor data or other factors and adjust the relative importance put on each signal.

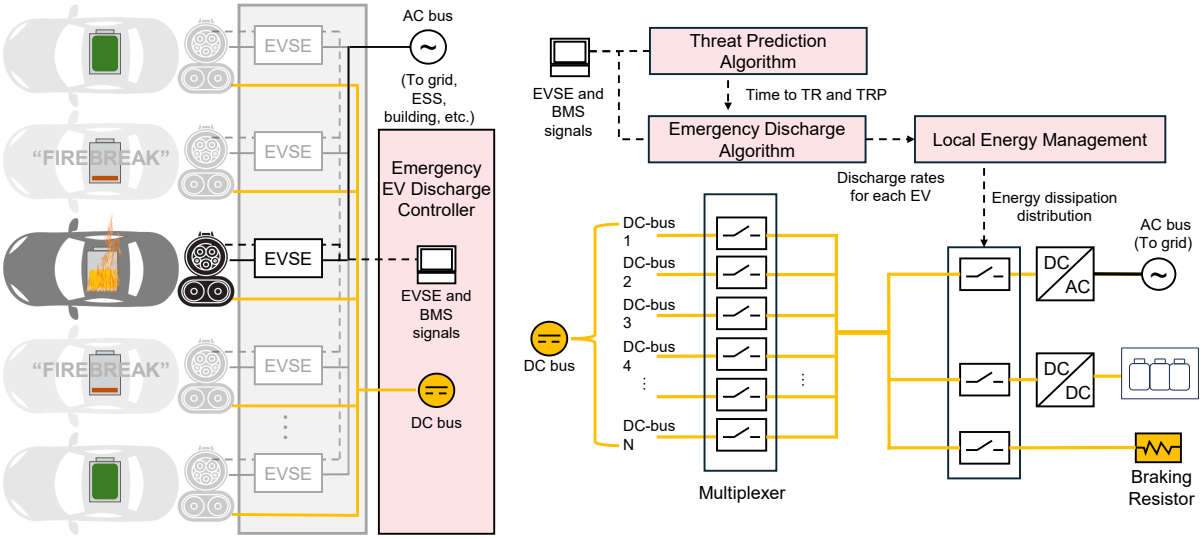
Meanwhile, adaptive thresholds respond to changes in the system environment or usage by incorporating real-time feedback with historical data to ensure that thresholds remain relevant under different operating conditions [21, 92]. Additionally, by combining models that capture both normal operation and abnormal behavior with rich data, such as with multi-modal sensing, state estimation techniques can potentially be used to detect abnormal behaviors that are not directly observable from raw sensor outputs alone. Beyond algorithm development, multiphysics modeling can help provide more comprehensive scenario testing to evaluate performance accuracy and robustness against common issues like model mismatch and noise.

6.2.5 Discharge mitigation and infrastructural requirements

Discharge mitigation can be used in a wide range of scenarios to reduce safety risks and hazards during emergency response, transportation, and storage. The discharge can also be performed at different rates depending on time constraints, the safety risks of evolving hazards, and the available infrastructure. At the lowest level, discharge of the order of a few hours within normal operating limits (<1 C) can be performed before transporting an undamaged LIB system or if potential hazards are forecasted. These situations include the planned replacement of aged or recalled EV packs; parking in SOC-restricted areas; and evacuation from natural disasters such as hurricanes, floods, and wildfires. Discharging faster (<4-6 C) can help delay TR propagation from external quickly evolving hazards, but may require operating beyond normal operating limits. This could apply, for example, if a fire (e.g. building, brush, or EV fire) breaks out in EV-dense areas like fleet depots or charging stations. The last and most difficult case is delaying or stopping TR propagation within the pack or system itself (<6-10 C). This requires discharging quickly before widespread damage to the electrical connections, sensors, and BMS occurs and would likely require additional pack and system design adaptations to enable this.

Implementing discharge mitigation at any level requires additional integrated controllers and communication capabilities between equipment to handle the potentially high currents, electrical loads, and safety risks involved. For EVs, developments in vehicle-to-grid (V2G) and fast charging technology will help enable high-power, bidirectional infrastructure upgrades. For example, depending on the situation, EVs may be able to leverage onboard and offboard electrical loads for energy dissipation if connected to a bidirectional charger (EVSE), as illustrated in Fig. 6.1. Offboard, charger-integrated loads may include stationary energy storage (e.g. battery or supercapacitor bank), building, (micro-)grid, dedicated braking resistor, or other physically distant vehicles. Onboard vehicle loads include those that can be powered by the high-voltage bus, e.g. battery thermal management, cabin HVAC, motors, etc.

While this dissertation focuses on addressing the modeling needs for developing early detection with multi-modal sensor fusion and discharge mitigation strategies, future work should develop these algorithms and assess their real-world applicability, thereby advancing the safety of lithium-ion battery systems.



(a) EVSE equipment integration

(b) Controller and hardware

Figure 6.1: Overview of emergency discharge with EVSEs

APPENDIX A

Pouch Cell Temperature Measurements

The pouch cell surface temperatures are measured at the edge between the tabs and at the center of the cell during the external short circuit tests, as illustrated in Fig. A.1. Although only the center surface temperature is considered in this work, both are plotted in Fig. A.2 to provide a better understanding of the unmodeled thermal gradient.

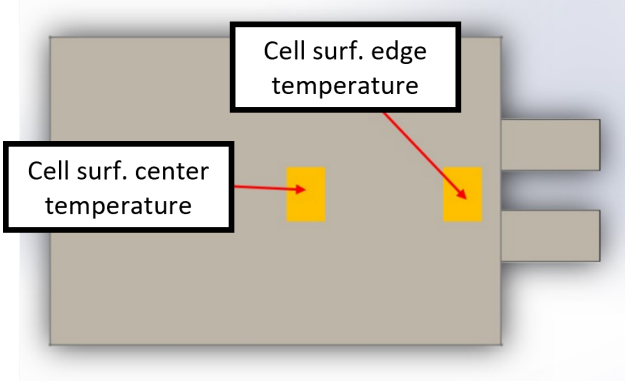


Figure A.1: Thermocouple placement on surface of pouch cell

During the initial temperature rise for each of the pouch cells, both measured temperatures follow each other closely before deviating near the peak and during the cooling phase after the current has largely decayed. At most, the largest temperature difference is 7 °C at the peak and 10 °C afterwards as the cell cools based on Cells 100A and 75, respectively.

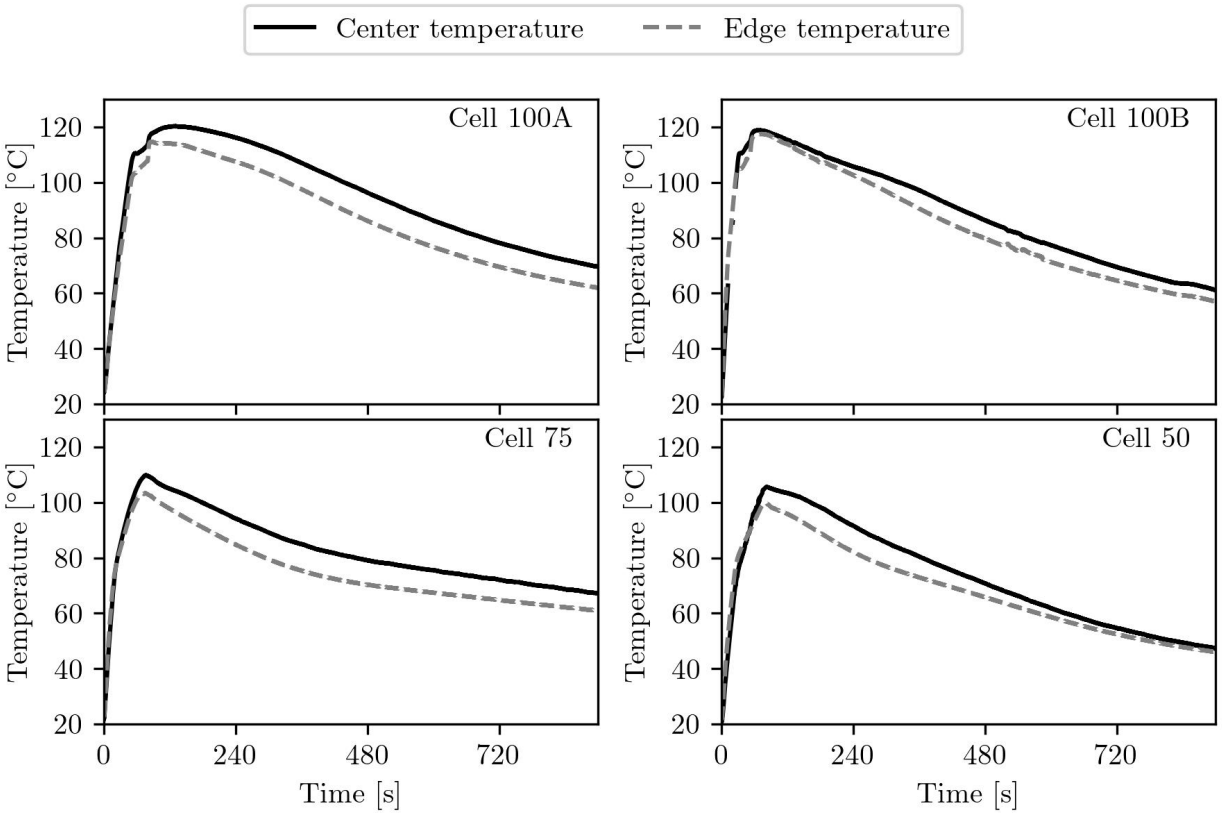


Figure A.2: Cell edge and center surface temperatures measured during the ESC experiments. The center surface temperature was used for model development in this work.

APPENDIX B

SPMe-based Multiphysics Model Equations and Parameters

B.1 Single Particle Model with electrolyte equations

The single-particle model with electrolyte (SPMe) is a reduced-order electrochemical model that assumes a uniform intercalation current density (i_k) across the electrode, such that

$$i_{\mathrm{k}} = \begin{cases} \frac{I}{a_{\mathrm{s,n}} L_{\mathrm{n}}}, & \mathrm{k} = \mathrm{n}, \\ -\frac{I}{a_{\mathrm{s,p}} L_{\mathrm{p}}}, & \mathrm{k} = \mathrm{p}, \end{cases} \tag{B.1}$$

where L_{k} is the thickness of the electrode. The surface area to volume ratio of the electrode active material is $a_{\mathrm{s,k}} = 3\epsilon_{\mathrm{s,k}}/R_{\mathrm{k}}$, where $\epsilon_{\mathrm{s,k}}$ is the electrode active material volume fraction, and R_{k} is the particle radius. Assuming each particle in an electrode behaves identically, each electrode is represented by a single particle.

Compared to the original single-particle model (SPM), retaining the electrolyte dynamics in the SPMe improves the model fidelity under higher current operation. Most of the equations are from Marquis et al. [67] with an additional concentration overpotential in the solid to match the voltage losses as updated in PyBaMM [68]. The negative electrode, separator, and positive electrode regions are denoted as k $\in$ n,s,p, respectively. A summary of the SPMe model parameters are provided in Table B.2.

B.1.1 Particle diffusion

Two spherical particle diffusion equations are used to capture the diffusion of lithium in the solid electrode particles, one for each electrode such that,

$$\frac{\partial c_{\mathrm{s,k}}}{\partial t}(r_{\mathrm{k}}, t) = -\frac{1}{r_{\mathrm{k}}^2}\frac{\partial}{\partial r_{\mathrm{k}}}\left(r_{\mathrm{k}}^2 N_{\mathrm{s,k}}\right), \tag{B.2}$$

$$N_{\mathrm{s,k}} = -D_{\mathrm{s,k}}(c_{\mathrm{s,k}})\frac{\partial c_{\mathrm{s,k}}}{\partial r_{\mathrm{k}}}, \quad \mathrm{k} \in \mathrm{n},\, \mathrm{p}. \tag{B.3}$$

In each representative particle, the concentration of lithium is $c_{\mathrm{s,k}}$, while the radial coordinate of the particle is $r_{\mathrm{k}} \in [0, R_{\mathrm{k}}]$. The flux in the solid particle within the region k is $N_{\mathrm{s,k}}$, and $D_{\mathrm{s,k}}$ is the solid diffusion coefficient for $\mathrm{k} \in \mathrm{n},\, \mathrm{p}$.

For the boundary conditions, there is a no-flux condition at the center and a molar flux of j_{k} at the surface. Additionally, the concentration in the particle is initially uniform. These boundary and initial conditions are expressed as

$$N_{\mathrm{s,k}}\big|_{r_{\mathrm{k}}=0} = 0, \quad \mathrm{k} \in \mathrm{n},\, \mathrm{p} \tag{B.4}$$

$$N_{\mathrm{s,k}}\big|_{r_{\mathrm{k}}=R_{\mathrm{k}}} = j_{\mathrm{k}} = \frac{i_{\mathrm{k}}}{F} \tag{B.5}$$

$$c_{\mathrm{s,k}}(r_{\mathrm{k}}, 0) = c_{\mathrm{s,k},0}, \quad \mathrm{k} \in \mathrm{n},\, \mathrm{p}, \tag{B.6}$$

where F is Faraday's constant and $c_{\mathrm{s,k},0}$ is the initial concentration in the electrode.

B.1.2 Electrolyte diffusion

For the liquid phase, the diffusion of Li^+ in the electrolyte is described by

$$\epsilon_{\mathrm{e,k}}\frac{\partial c_{\mathrm{e,k}}}{\partial t} = -\frac{\partial N_{\mathrm{e,k}}}{\partial x} + \begin{cases} \frac{I}{FL_{\mathrm{n}}}, & \mathrm{k} = \mathrm{n}, \\ 0, & \mathrm{k} = \mathrm{s}, \\ -\frac{I}{FL_{\mathrm{p}}}, & \mathrm{k} = \mathrm{p}, \end{cases} \tag{B.7}$$

where $c_{\mathrm{e,k}}$ is the concentration of Li^+ in the electrolyte, and ϵ_k is the electrolyte volume fraction. The flux of Li^+ in the electrolyte in region k is $N_{\mathrm{e,k}}$, which is given by

$$N_{\mathrm{e,k}} = -\epsilon_{\mathrm{k}}^{\mathrm{b}} D_{\mathrm{e}}\frac{\partial c_{\mathrm{e,k}}}{\partial x} + \begin{cases} \frac{xt^+I}{FL_{\mathrm{n}}}, & \mathrm{k} = \mathrm{n} \\ \frac{t^+I}{F}, & \mathrm{k} = \mathrm{s} \\ \frac{(L-x)t^+I}{FL_{\mathrm{p}}}, & \mathrm{k} = \mathrm{p} \end{cases} \tag{B.8}$$

where D_e is the electrolyte diffusion coefficient; $x \in [0, L]$ is the through-cell distance; and t^+ is the transference number.

Initially, the electrolyte concentration across the electrode is uniform. Additionally, there is a no-flux boundary condition at the current collectors, and $N_\mathrm{e,k}$ is subject to concentration and flux continuity at the separator-electrode interfaces. The boundary and initial conditions are then

$$N_\mathrm{e,n}\big|_{x=0} = 0, \quad N_\mathrm{e,p}\big|_{x=L} = 0, \tag{B.9}$$

$$c_\mathrm{e,n}\big|_{x=L_\mathrm{n}} = c_\mathrm{e,s}\big|_{x=L_\mathrm{n}}, \tag{B.10}$$

$$N_\mathrm{e,n}\big|_{x=L_\mathrm{n}} = N_\mathrm{e,s}\big|_{x=L_\mathrm{n}}, \tag{B.11}$$

$$c_\mathrm{e,s}\big|_{x=L-L_\mathrm{p}} = c_\mathrm{e,p}\big|_{x=L-L_\mathrm{p}}, \tag{B.12}$$

$$N_\mathrm{e,s}\big|_{x=L-L_\mathrm{p}} = N_\mathrm{e,p}\big|_{x=L-L_\mathrm{p}}, \tag{B.13}$$

$$c_\mathrm{e,k}(x, 0) = c_\mathrm{e}^\mathrm{typ}, \quad \mathrm{k} \in \mathrm{n,\ s,\ p.} \tag{B.14}$$

B.1.3 Terminal voltage

The terminal voltage is given by the equation

$$V_T = U_\mathrm{eq} + \eta_r + \eta_\mathrm{c,e} + \eta_\mathrm{c,s} + \Delta\Phi_\mathrm{e} + \Delta\Phi_\mathrm{s} - IR_\mathrm{tab}, \tag{B.15}$$

where U_eq is the open circuit voltage; η_r is the reaction overpotential; $\eta_\mathrm{c,e}$ and $\eta_\mathrm{c,s}$ are the concentration overpotentials in the electrolyte and particles, respectively; and $\Delta\Phi_\mathrm{e}$ and $\Delta\Phi_\mathrm{s}$ are the Ohmic losses in the electrolyte and solid, respectively. Additionally, IR_tab is included to account for the Ohmic loss from the contact resistance between the voltage clips and cell tabs.

The individual voltage components are further defined as

$$U_{\text{eq}} = U_{\text{p}}(c_{\text{s,p}}\big|_{r_{\text{p}}=R_{\text{p}}}) - U_{\text{n}}(c_{\text{s,n}}\big|_{r_{\text{n}}=R_{\text{n}}}), \tag{B.16}$$

$$\eta_r = \frac{-2RT}{F}\sinh^{-1}\left(\frac{I}{a_{\text{s,p}}\bar{i}_{0,\text{p}}L_{\text{p}}}\right) - \frac{-2RT}{F}\sinh^{-1}\left(\frac{I}{a_{\text{s,n}}\bar{i}_{0,\text{n}}L_{\text{n}}}\right), \tag{B.17}$$

$$\eta_{\text{c,e}} = \frac{2RT}{Fc_{\text{e}}^{\text{typ}}}(1-t^+)\left(\bar{c}_{\text{e,p}} - \bar{c}_{\text{e,n}}\right), \tag{B.18}$$

$$\eta_{\text{c,s}} = \left(U_{\text{p}}(c_{\text{s,p}}\big|_{r_{\text{p}}=R_{\text{p}}}) - U_{\text{p}}(\bar{c}_{\text{s,p}})\right) - \left(U_{\text{n}}(c_{\text{s,n}}\big|_{r_{\text{n}}=R_{\text{n}}}) - U_{\text{n}}(\bar{c}_{\text{s,n}}\right), \tag{B.19}$$

$$\bar{i}_{0,\text{n}} = \frac{1}{L_{\text{n}}}\int_0^{L_{\text{n}}} i_{0,\text{n}}\mathrm{d}x, \quad \bar{i}_{0,\text{p}} = \frac{1}{L_{\text{p}}}\int_{L-L_{\text{p}}}^{L} i_{0,\text{p}}\mathrm{d}x, \tag{B.20}$$

$$i_{0,\text{k}} = k_{0,\text{k}}(c_{\text{s,k}}^{\text{surf}})^{1/2}(c_{\text{s,k}}^{\text{max}} - c_{\text{s,k}}^{\text{surf}})^{1/2}(c_{\text{e,k}})^{1/2}, \tag{B.21}$$

$$\Delta\Phi_{\text{e}} = -\frac{I}{\kappa_{\text{e}}}\left(\frac{L_{\text{n}}}{3\epsilon_{\text{n}}^{\text{b}}} + \frac{L_{\text{s}}}{\epsilon_{\text{s}}^{\text{b}}} + \frac{L_{\text{p}}}{3\epsilon_{\text{p}}^{\text{b}}}\right), \tag{B.22}$$

$$\Delta\Phi_{\text{s}} = -\frac{I}{3}\left(\frac{L_{\text{p}}}{\sigma_{\text{p}}} + \frac{L_{\text{n}}}{\sigma_{\text{n}}}\right), \tag{B.23}$$

where

$$\bar{c}_{\text{e,n}} = \frac{1}{L_{\text{n}}}\int_0^{L_{\text{n}}} c_{\text{e,n}}\mathrm{d}x, \quad \bar{c}_{\text{e,p}} = \frac{1}{L_{\text{p}}}\int_{L-L_{\text{p}}}^{L} c_{\text{e,p}}\mathrm{d}x, \tag{B.24}$$

$$\bar{c}_{\text{s,n}} = \frac{3}{R_{\text{n}}^3}\int_0^{R_{\text{n}}} c_{\text{s,n}}r^2\mathrm{d}r, \quad \bar{c}_{\text{s,p}} = \frac{3}{R_{\text{p}}^3}\int_0^{R_{\text{p}}} c_{\text{s,p}}r^2\mathrm{d}r. \tag{B.25}$$

The electrode open-circuit potentials are U_{k}; $\bar{c}_{\text{e,k}}$ is the electrode-averaged Li^+ concentration in the electrolyte; and $\bar{c}_{\text{s,k}}$ is the average Li concentration in the particle. The Li concentration in the solid particle is $c_{\text{s,k}}^{\text{surf}} = c_{\text{s,k}}\big|_{r_{\text{k}}=R_{\text{k}}}$. The exchange current density and the electrode-averaged exchange current density are $i_{0,\text{k}}$ and $\bar{i}_{0,\text{k}}$, respectively, with a reaction rate constant of $k_{0,\text{k}}$. The solid and electrolyte conductivities are σ_{k} and κ_{e}, respectively, while the electrolyte volume fraction is ϵ_k for k $\in$ n,s,p. The Bruggeman coefficient is b; the universal gas constant is R, and cell temperature is T.

Table B.1: Summary of venting and thermal model parameters

Model	Parameter	Value	Unit	Description	Source
Electrolyte vaporization	y_{EC}	0.3	-	Volume fraction of EC	[27]
	y_{DMC}	0.7	-	Volume fraction of DMC	[27]
	A_{EC}	6.4897	-	Antoine coefficient A for EC	[57]
	B_{EC}	1836.57	K	Antoine coefficient B for EC	[57]
	C_{EC}	-102.23	K	Antoine coefficient C for EC	[57]
	A_{DMC}	6.4338	-	Antoine coefficient A for DMC	[57]
	B_{DMC}	1413.0	K	Antoine coefficient B for DMC	[57]
	C_{DMC}	-44.25	K	Antoine coefficient C for DMC	[57]
SEI decomposition	A_{SEI}	1.32×10^{14}	s^{-1}	Frequency factor	Fitted
	E_{SEI}	2.24×10^{-19}	J	Reaction activation energy	[40]
	h_{SEI}	257	J/g	Enthalpy of reaction	[40]
	$x_{\mathrm{SEI},0}$	0.15	-	Initial mole fraction Li in SEI to C_6	[40]
	$M_{\mathrm{C_6}}$	72	g/mol	Molar mass of graphite	-
	m_{an}	19.1	g	Anode mass	[27]
	k_b	1.381×10^{-23}	$\mathrm{m^2kg/(s^2K)}$	Boltzmann's constant	-
Internal cell pressure	$V_{\mathrm{h},0}$	6.65×10^{-6}	m^3	Initial volume of headspace	Measured [27]
	A_{surf}	0.009	m^2	Cell-fixture contact surface area	Measured [27]
	L	2.4	mm	Thickness of two poron sheets	Measured [27]
	E	0.19	MPa	Young's modulus for poron sheets	Measured [27]
	α_{cell}	1.1	μm/K	Cell thermal expansion coefficient	[123]
	P_{atm}	101	kPa	Atmospheric pressure	-
	P_{crit}	158	kPa	Critical vent pressure	Measured [27]
	P_0	10-16	kPa	Initial fixture pre-load pressure	Measured [27]
Lumped thermal	m	0.130	kg	Mass of the cell	Calculated [69]
	C_{p}	2733	$\mathrm{J/(kg \cdot K)}$	Effective cell heat capacity	Fitted
	h	34.8	$\mathrm{W/(m^2\ K)}$	Effective heat transfer coefficient	Fitted
	A	255.5	mm^2	Cell surface area for cooling	Measured
	T_{amb}	294-298	K	Ambient temperature	Measured

Table B.2: Summary of SPMe parameters

Parameter	Neg.	Sep.	Pos.	Unit	Description	Source
L_{k}	62	12	67	μm	Electrode thickness	[69]
ϵ_{k}	0.3	0.4	0.3	-	Electrolyte volume fraction	[69]
R_{k}	10	-	3.5	μm	Particle radius	[69]
$D_{\mathrm{s,k,0}}$	8.0×10^{-14}	-	8.0×10^{-15}	m^2/s	Nominal solid diffusivity	[60, 69]
σ_{k}	100	-	100	S/m	Solid conductivity	[69]
$c_{\mathrm{s,k}}^{\mathrm{max}}$	28746	-	35380	$\mathrm{mol{\cdot}m^{-3}}$	Maximum concentration in the solid	[69]
$k_{0,\mathrm{k}}$	4.244×10^{-6}	-	4.824×10^{-6}	$\mathrm{Am^{-2}(m^3mol)^{-1.5}}$	Reaction rate constant	[69]
$c_{\mathrm{e}}^{\mathrm{typ}}$	1000			$\mathrm{mol{\cdot}m^{-3}}$	Typical electrolyte concentration	[69]
D_{e}	5.35×10^{-10}			m^2/s	Electrolyte diffusivity	[69]
κ_{e}	1.3			S/m	Electrolyte conductivity	[69]
F	96485			C/mol	Faraday's constant	-
R	8.314			J/(mol K)	Universal gas constant	-
T	298.15			K	Temperature	[67]
b	1.5			-	Bruggeman coefficient	[69]
t^+	0.38			-	Transference number	[69]
$x_{\mathrm{Li,0}}$	0			-	Negative electrode stoichiometry at 0%SOC	Fitted
$x_{\mathrm{Li,100}}$	0.8321			-	Negative electrode stoichiometry at 100%SOC	Fitted
$y_{\mathrm{Li,0}}$	0.837			-	Positive electrode stoichiometry at 0%SOC	Fitted
$y_{\mathrm{Li,100}}$	0.034			-	Positive electrode stoichiometry at 100%SOC	Fitted
R_{tab}	5-8			mΩ	Series tabbing resistance	Fitted
R_{ESC}	4-7			mΩ	External short circuit resistance	Fitted

Table B.3: SPMe open circuit potential and active material diffusivity

Parameter	Function	Unit	Description	Source
$U_{\mathrm{n}}(x_{\mathrm{Li}})$	$0.063 + 0.8\exp(-75(x_{\mathrm{Li}} + 0.007))$ $- 0.0120\tanh(\frac{x_{\mathrm{Li}} - 0.127}{0.016}) - 0.0118\tanh(\frac{x_{\mathrm{Li}} - 0.155}{0.016})$ $- 0.0035\tanh(\frac{x_{\mathrm{Li}} - 0.220}{0.020}) - 0.0095\tanh(\frac{x_{\mathrm{Li}} - 0.190}{0.013})$ $- 0.0145\tanh(\frac{x_{\mathrm{Li}} - 0.490}{0.020}) - 0.0800\tanh(\frac{x_{\mathrm{Li}} - 1.030}{0.055})$	V	Negative electrode OCP	[69]
$U_{\mathrm{p}}(y_{\mathrm{Li}})$	$4.3452 - 1.6518y_{\mathrm{Li}} + 1.6225y_{\mathrm{Li}}^2 - 2.0843y_{\mathrm{Li}}^3 + 3.5146y_{\mathrm{Li}}^4$ $- 2.2166y_{\mathrm{Li}}^5 - 0.5623\exp(109.451y_{\mathrm{Li}} - 100.006)$	V	Positive electrode OCP	[69]
$D_{\mathrm{s,n}}(z)$	$D_{s,n,0}(1.12070451z + 0.09209274)$	m^2/s	Negative electrode solid diffusivity	Fitted [8]
$D_{\mathrm{s,p}}(z)$	$D_{s,p,0}(4.7302281z^2 - 4.5023245z + 1.26466141)$	m^2/s	Positive electrode solid diffusivity	Fitted [8]

BIBLIOGRAPHY

[1] UL. Lithium-ion Battery Incident Reporting. https://www.ul.com/insights/lithium-ion-battery-incident-reporting. [Accessed 04-04-2024].

[2] Electric vehicle outlook 2023. https://about.bnef.com/electric-vehicle-outlook/. [Accessed 04-04-2024].

[3] Lithium ion battery market is moving into surge mode. https://interactanalysis.com/insight/lithium-ion-battery-market-is-moving-into-surge-mode/. [Accessed 04-04-2024].

[4] NTSB. Safety risks to emergency responders from lithium-ion battery fires in electric vehicles. Technical report, NTSB, 2020.

[5] Eric Rask, Craig Pavlich, Kevin Stutenberg, Michael Duoba, Glenn Keller, et al. Stranded energy assessment techniques and tools. Technical report, National Highway Traffic Safety Administration, 2020.

[6] William S. Schoonover. Safety advisory notice for the transportation of lithium batteries for disposal or recycling, May 2022.

[7] Peyman Mohtat. *Advanced Diagnostics for Lithium-ion Batteries: Decoding the Information in Electrode Swelling*. PhD thesis, University of Michigan, Ann Arbor, 2021.

[8] Vivian Tran, Jason B Siegel, and Anna G Stefanopoulou. Single particle model with electrolyte for simulating diffusion-limited dynamics during an external short in li-ion batteries. *IFAC-PapersOnLine*, 2023.

[9] IEA. Global ev outlook 2020, June 2020.

[10] IEA, April 2023.

[11] Energy storage investments boom as battery costs halve in the next decade, Jul 2019.

[12] Peiyi Sun, Roeland Bisschop, Huichang Niu, and Xinyan Huang. A review of battery fires in electric vehicles. *Fire technology*, pages 1–50, 2020.

[13] Haavard R Boehmer, Michael S Klassen, and Stephen M Olenick. Modern vehicle hazards in parking structures and vehicle carriers, July 2020.

[14] International Association of Fire and Rescue Services. Up to 150 000 liters of water needed to put out a fire in an electric car, 2022. [Online; accessed 18-May-2025].

[15] Austrailian Government Department of Defense. 04.11 what is ev fire reignition?, 2021. [Online; accessed 18-May-2025].

[16] Jesse Roman. Stranded energy, Jan 2020.

[17] Price, Jane and Cheung, Ivan. Safety risks to emergency responders from lithium-ion battery fires in electric vehicles: Prevalence of electric vehicle battery fires. Technical report, National Transportation Safety Board, 2018.

[18] James Shaw-Stewart, Anna Alvarez-Reguera, Agata Greszta, James Marco, Maryam Masood, Rob Sommerville, and Emma Kendrick. Aqueous solution discharge of cylindrical lithium-ion cells. *Sustainable Materials and Technologies*, 22:e00110, 2019.

[19] Depeng Kong, Hongpeng Lv, Ping Ping, and Gongquan Wang. A review of early warning methods of thermal runaway of lithium ion batteries. *Journal of Energy Storage*, 64:107073, 2023.

[20] Ting Cai, Puneet Valecha, Vivian Tran, Brian Engle, Anna Stefanopoulou, and Jason Siegel. Detection of li-ion battery failure and venting with carbon dioxide sensors. *eTransportation*, 7:100100, 2021.

[21] Ting Cai, Peyman Mohtat, Anna G Stefanopoulou, and Jason B Siegel. Li-ion battery fault detection in large packs using force and gas sensors. *IFAC-PapersOnLine*, 53(2):12491–12496, 2020.

[22] Xuning Feng, Siqi Zheng, Dongsheng Ren, Xiangming He, Li Wang, Hao Cui, Xiang Liu, Changyong Jin, Fangshu Zhang, Chengshan Xu, et al. Investigating the thermal runaway mechanisms of lithium-ion batteries based on thermal analysis database. *Applied Energy*, 246:53–64, 2019.

[23] Simon Müller, Jens Eller, Martin Ebner, Chris Burns, Jeff Dahn, and Vanessa Wood. Quantifying inhomogeneity of lithium ion battery electrodes and its influence on electrochemical performance. *Journal of The Electrochemical Society*, 165(2):A339, 2018.

[24] Xuning Feng, Minggao Ouyang, Xiang Liu, Languang Lu, Yong Xia, and Xiangming He. Thermal runaway mechanism of lithium ion battery for electric vehicles: A review. *Energy Storage Materials*, 10:246–267, 2018.

[25] Paul T Coman, Stefan Mátéfi-Tempfli, Christian T Veje, and Ralph E White. Modeling vaporization, gas generation and venting in li-ion battery cells with a dimethyl carbonate electrolyte. *Journal of The Electrochemical Society*, 164(9):A1858–A1865, 2017.

[26] Michael Lammer, Alexander Königseder, and Viktor Hacker. Holistic methodology for characterisation of the thermally induced failure of commercially available 18650 lithium ion cells. *RSC advances*, 7(39):24425–24429, 2017.

[27] Ting Cai, Vivian Tran, Anna G Stefanopoulou, and Jason B Siegel. Modeling li-ion battery first venting events before thermal runaway. *IFAC-PapersOnLine*, 54(20):528–533, 2021.

[28] Vivian Tran, Jason B Siegel, and Anna G Stefanopoulou. Extending a multiphysics li-ion battery model from normal operation to short circuit and venting. *Journal of The Electrochemical Society*, 171(6):060507, 2024.

[29] Paul T Coman, Stefan Mátéfi-Tempfli, Christian T Veje, and Ralph E White. Modeling vaporization, gas generation and venting in li-ion battery cells with a dimethyl carbonate electrolyte. *Journal of The Electrochemical Society*, 164(9):A1858–A1865, 2017.

[30] Daniel H Doughty. Vehicle battery safety roadmap guidance. Technical report, National Renewable Energy Lab.(NREL), Golden, CO (United States), 2012.

[31] Hossein Maleki and Jason N Howard. Role of the cathode and anode in heat generation of li-ion cells as a function of state of charge. *Journal of Power Sources*, 137(1):117–127, 2004.

[32] JR Dahn, EW Fuller, M Obrovac, and U Von Sacken. Thermal stability of lixcoo2, lixnio2 and λ-mno2 and consequences for the safety of li-ion cells. *Solid State Ionics*, 69(3-4):265–270, 1994.

[33] Haotian Yan and Ofodike A Ezekoye. State of charge effects on active material elemental composition changes between pre-thermal-runaway and post-failure states for 8-1-1 nickel-manganese-cobalt 18650 cells. *Journal of Energy Storage*, 63:106974, 2023.

[34] Judith A. Jeevarajan et al. Battery hazards for large energy storage systems. *ACS Energy Letters*, 7(8):2725–2733, 2022.

[35] Andrey W Golubkov, Sebastian Scheikl, René Planteu, Gernot Voitic, Helmar Wiltsche, Christoph Stangl, Gisela Fauler, Alexander Thaler, and Viktor Hacker. Thermal runaway of commercial 18650 li-ion batteries with lfp and nca cathodes–impact of state of charge and overcharge. *Rsc Advances*, 5(70):57171–57186, 2015.

[36] Heather M Barkholtz, Yuliya Preger, Sergei Ivanov, Jill Langendorf, Loraine Torres-Castro, Joshua Lamb, Babu Chalamala, and Summer R Ferreira. Multi-scale thermal stability study of commercial lithium-ion batteries as a function of cathode chemistry and state-of-charge. *Journal of Power Sources*, 435:226777, 2019.

[37] Fengwei Jiang, Kai Liu, Zhirong Wang, Xuan Tong, and Linsheng Guo. Theoretical analysis of lithium-ion battery failure characteristics under different states of charge. *Fire and Materials*, 42(6):680–686, 2018.

[38] Tian Ying, She Yang, Wu Jiafeng, Chai Mu, and Huang Liansheng. Thermal runaway propagation characteristics of lithium-ion batteries with a non-uniform state of charge distribution. *Journal of Solid State Electrochemistry*, 27(8):2185–2197, 2023.

[39] Guobin Zhong, Huang Li, Chao Wang, Kaiqi Xu, and Qingsong Wang. Experimental analysis of thermal runaway propagation risk within 18650 lithium-ion battery modules. *Journal of The Electrochemical Society*, 165(9):A1925, 2018.

[40] Paul Coman, Eric Darcy, Christian Veje, and Ralph White. Modelling li-ion cell thermal runaway triggered by an internal short circuit device using an efficiency factor and arrhenius formulations. *JES*, 164(4):A587–A593, 2017.

[41] Yang Peng, Lizhong Yang, Xiaoyu Ju, Baisheng Liao, Kai Ye, Lun Li, Bei Cao, and Yong Ni. A comprehensive investigation on the thermal and toxic hazards of large format lithium-ion batteries with lifepo4 cathode. *Journal of Hazardous Materials*, 381:120916, 2020.

[42] Christiane Essl, Andrey W Golubkov, and Anton Fuchs. Influence of aging on the failing behavior of automotive lithium-ion batteries. *Batteries*, 7(2):23, 2021.

[43] Yuliya Preger, Loraine Torres-Castro, Taina Rauhala, and Judith Jeevarajan. Perspective—on the safety of aged lithium-ion batteries. *Journal of the Electrochemical Society*, 169(3):030507, 2022.

[44] M Börner, A Friesen, M Grützke, YP Stenzel, G Brunklaus, J Haetge, S Nowak, FM Schappacher, and M Winter. Correlation of aging and thermal stability of commercial 18650-type lithium ion batteries. *Journal of Power Sources*, 342:382–392, 2017.

[45] Alex Friesen, Fabian Horsthemke, Xaver Mönnighoff, Gunther Brunklaus, Roman Krafft, Markus Börner, Tim Risthaus, Martin Winter, and Falko M Schappacher. Impact of cycling at low temperatures on the safety behavior of 18650-type lithium ion cells: Combined study of mechanical and thermal abuse testing accompanied by post-mortem analysis. *Journal of Power Sources*, 334:1–11, 2016.

[46] Hanwei Zhou, Conner Fear, Rachel E Carter, Corey T Love, and Partha P Mukherjee. Correlating lithium plating quantification with thermal safety characteristics of lithium-ion batteries. *Energy Storage Materials*, 66:103214, 2024.

[47] Xinlei Gao, Kuijie Li, Yuan-cheng Cao, Gregory J Offer, and Huizhi Wang. Simulation and understanding of degraded lithium-ion battery self-heating ignition. *Applied Energy*, 384:125435, 2025.

[48] Kandler Smith, Gi-Heon Kim, Eric Darcy, and Ahmad Pesaran. Thermal/electrical modeling for abuse-tolerant design of lithium ion modules. *International Journal of Energy Research*, 34(2):204–215, 2010.

[49] Zeyu Chen, Bo Zhang, Rui Xiong, Weixiang Shen, and Quanqing Yu. Electro-thermal coupling model of lithium-ion batteries under external short circuit. *Applied Energy*, 293:116910, 2021.

[50] Xinfan Lin, Hector E Perez, Shankar Mohan, Jason B Siegel, et al. A lumped-parameter electro-thermal model for cylindrical batteries. *Journal of Power Sources*, 257:1–11, 2014.

[51] Akos Kriston, Andreas Pfrang, Harry Döring, Benjamin Fritsch, et al. External short circuit performance of graphite-lini1/3co1/3mn1/3o2 and graphite-lini0. 8co0. 15al0. 05o2 cells at different external resistances. *Journal of Power Sources*, 361:170–181, 2017.

[52] Alexander Rheinfeld et al. Quasi-isothermal external short circuit tests applied to lithium-ion cells: Part ii. modeling and simulation. *JES*, 166(2):A151, 2019.

[53] Ti Dong, Yiwei Wang, Peng Peng, and Fangming Jiang. Electrical-thermal behaviors of a cylindrical graphite-nca li-ion battery responding to external short circuit operation. *International journal of energy research*, 43(4):1444–1459, 2019.

[54] Steffen Hess, Margret Wohlfahrt-Mehrens, and Mario Wachtler. Flammability of li-ion battery electrolytes: flash point and self-extinguishing time measurements. *Journal of The Electrochemical Society*, 162(2):A3084, 2015.

[55] Ruqing Fang and Zhe Li. A modeling framework of electrochemo-mechanics of lithium-ion battery: part ii. porous electrodes with contact stress effect. *Journal of The Electrochemical Society*, 169(9):090515, 2022.

[56] Ruqing Fang and Zhe Li. A multiscale electrochemo-mechanical model of porous electrode in lithium-ion batteries: The coupling of reaction and finite deformation. *Electrochimica Acta*, 475:143581, 2024.

[57] Yun-Jin Fang and Jun-Ming Qian. Isobaric vapor- liquid equilibria of binary mixtures containing the carbonate group- ocoo-. *Journal of Chemical & Engineering Data*, 50(2):340–343, 2005.

[58] MN Richard and JR Dahn. Accelerating rate calorimetry study on the thermal stability of lithium intercalated graphite in electrolyte. i. experimental. *Journal of The Electrochemical Society*, 146(6):2068, 1999.

[59] TD Hatchard, DD MacNeil, A Basu, and JR Dahn. Thermal model of cylindrical and prismatic lithium-ion cells. *JES*, 148(7):A755, 2001.

[60] Sravan Pannala, Hamidreza Movahedi, Taylor R Garrick, Anna G Stefanopoulou, and Jason B Siegel. Consistently tuned battery lifetime predictive model of capacity loss, resistance increase, and irreversible thickness growth. *Journal of The Electrochemical Society*, 171(1):010532, 2024.

[61] Xiao-Guang Yang, Yongjun Leng, Guangsheng Zhang, Shanhai Ge, and Chao-Yang Wang. Modeling of lithium plating induced aging of lithium-ion batteries: Transition from linear to nonlinear aging. *Journal of Power Sources*, 360:28–40, 2017.

[62] E Linul, L Marsavina, T Voiconi, and T Sadowski. Study of factors influencing the mechanical properties of polyurethane foams under dynamic compression. In *Journal of Physics: Conference Series*, volume 451, page 012002. IOP Publishing, 2013.

[63] Morten Hovd and Richard D Braatz. Handling state and output constraints in mpc using time-dependent weights. In *Proceedings of the 2001 ACC*, volume 3, pages 2418–2423. IEEE, 2001.

[64] Dominic Liao-McPherson. Lecture notes: On the implementation of nonlinear nmpc using sqp methods, November 2020.

[65] Jing Mao, William Tiedemann, and John Newman. Simulation of li-ion cells by dualfoil model under constant-resistance load. *ECS Transactions*, 58(48):71, 2014.

[66] Alexander Rheinfeld, Andreas Noel, Jörn Wilhelm, Akos Kriston, Andreas Pfrang, and Andreas Jossen. Quasi-isothermal external short circuit tests applied to lithium-ion cells: Part i. measurements. *Journal of The Electrochemical Society*, 165(14):A3427, 2018.

[67] Scott Marquis, Valentin Sulzer, Robert Timms, Colin Please, and Jon Chapman. An asymptotic derivation of a single particle model with electrolyte. *JES*, 166(15):A3693, 2019.

[68] Valentin Sulzer, Scott G. Marquis, Robert Timms, Martin Robinson, and S. Jon Chapman. Python Battery Mathematical Modelling (PyBaMM). *JORS*, 9(1):14, 2021.

[69] Peyman Mohtat, Suhak Lee, Valentin Sulzer, Jason B Siegel, and Anna G Stefanopoulou. Differential expansion and voltage model for li-ion batteries at practical charging rates. *JES*, 167(11):110561, 2020.

[70] Scott J Moura, Federico Bribiesca Argomedo, Reinhardt Klein, Anahita Mirtabatabaei, and Miroslav Krstic. Battery state estimation for a single particle model with electrolyte dynamics. *IEEE Transactions on Control Systems Technology*, 25(2):453–468, 2016.

[71] Hyung-Joo Noh, Sungjune Youn, Chong Seung Yoon, and Yang-Kook Sun. Comparison of the structural and electrochemical properties of layered li [nixcoymnz] o2 (x= 1/3, 0.5, 0.6, 0.7, 0.8 and 0.85) cathode material for lithium-ion batteries. *Journal of Power Sources*, 233:121–130, 2013.

[72] Matthew Hough and Lindon Roberts. Model-based derivative-free methods for convex-constrained optimization. *SIOPT.*, 32(4):2552–2579, 2022.

[73] DD MacNeil, D Larcher, and JR Dahn. Comparison of the reactivity of various carbon electrode materials with electrolyte at elevated temperature. *Journal of the electrochemical society*, 146(10):3596, 1999.

[74] MN Richard and JR Dahn. Accelerating rate calorimetry study on the thermal stability of lithium intercalated graphite in electrolyte. ii. modeling the results and predicting differential scanning calorimeter curves. *Journal of The Electrochemical Society*, 146(6):2078, 1999.

[75] Jun-ichi Yamaki, Hideyasu Takatsuji, Tetsuya Kawamura, and Minato Egashira. Thermal stability of graphite anode with electrolyte in lithium-ion cells. *Solid State Ionics*, 148(3-4):241–245, 2002.

[76] Ph Biensan, B Simon, JP Peres, A De Guibert, M Broussely, JM Bodet, and F Perton. On safety of lithium-ion cells. *Journal of Power Sources*, 81:906–912, 1999.

[77] Peyman Mohtat, Suhak Lee, Jason B Siegel, and Anna G Stefanopoulou. Comparison of expansion and voltage differential indicators for battery capacity fade. *Journal of Power Sources*, 518:230714, 2022.

[78] Seong Jin An, Jianlin Li, Debasish Mohanty, Claus Daniel, Bryant J Polzin, Jason R Croy, Stephen E Trask, and David L Wood. Correlation of electrolyte volume and electrochemical performance in lithium-ion pouch cells with graphite anodes and nmc532 cathodes. *Journal of The Electrochemical Society*, 164(6):A1195, 2017.

[79] Mohammad Ayayda, Ralf Benger, Timo Reichrath, Kshitij Kasturia, Jacob Klink, and Ines Hauer. Modeling thermal runaway mechanisms and pressure dynamics in prismatic lithium-ion batteries. *Batteries*, 10(12):435, 2024.

[80] Haipeng Chen, Pengfei Zhang, Yaobo Wu, and Yuqi Huang. A comprehensive analysis of preload force effects on the opening of safety valves and thermal runaway behavior in prismatic batteries. *Journal of Energy Storage*, 105:114693, 2025.

[81] Vivian Tran, Jason Siegel, and Anna Stefanopoulou. Emergency li-ion battery discharge using nonlinear model predictive control with temperature and venting pressure constraints. In *2023 ACC*. IEEE, 2023.

[82] Iman Ebrahimi, Ricardo de Castro, Vivian Tran, Anna Stefanopoulou, and Shuang Feng. Emergency battery discharge under safety constraints using optimization-based controllers. In *2024 American Control Conference (ACC)*, pages 3498–3503. IEEE, 2024.

[83] Takuya Iwanaga, William Usher, and Jonathan Herman. Toward SALib 2.0: Advancing the accessibility and interpretability of global sensitivity analyses. *Socio-Environmental Systems Modelling*, 4:18155, May 2022.

[84] Jon Herman and Will Usher. SALib: An open-source python library for sensitivity analysis. *The Journal of Open Source Software*, 2(9), jan 2017.

[85] Max D Morris. Factorial sampling plans for preliminary computational experiments. *Technometrics*, 33(2):161–174, 1991.

[86] Qing Xu, Xiaoyang Wang, Hong Ye, Lili Gong, Peng Tan, and Tingrui Pan. An accurate state of health estimation method for lithium-ion batteries based on expansion force analysis. *Energy*, page 136155, 2025.

[87] Peyman Mohtat, Suhak Lee, Jason B Siegel, and Anna G Stefanopoulou. Reversible and irreversible expansion of lithium-ion batteries under a wide range of stress factors. *Journal of The Electrochemical Society*, 168(10):100520, 2021.

[88] Gennady Y Gor, John Cannarella, Jean H Prévost, and Craig B Arnold. A model for the behavior of battery separators in compression at different strain/charge rates. *Journal of The Electrochemical Society*, 161(11):F3065, 2014.

[89] Andrea Saltelli. Making best use of model evaluations to compute sensitivity indices. *Computer physics communications*, 145(2):280–297, 2002.

[90] Ilya M Sobol. Global sensitivity indices for nonlinear mathematical models and their monte carlo estimates. *Mathematics and computers in simulation*, 55(1-3):271–280, 2001.

[91] Kuijie Li, Jiahua Li, Xinlei Gao, Yao Lu, Depeng Wang, Weixin Zhang, Weixiong Wu, Xuebing Han, Yuan-cheng Cao, Languang Lu, et al. Effect of preload forces on multidimensional signal dynamic behaviours for battery early safety warning. *Journal of Energy Chemistry*, 92:484–498, 2024.

[92] Chengwei Jin, Jun Xu, Zhenyu Jia, Yanmin Xie, Xianggong Zhang, and Xuesong Mei. Expansion force signal based rapid detection of early thermal runaway for pouch batteries. *Energy*, 312:133685, 2024.

[93] Qi Chuang, Yan Hongtao, Yang Ju, Lin Chunjing, Zhou Yapeng, Hu Yuanzhi, and Chen Bin. Study on the characteristics of thermal runaway expansion force of lini0. 5co0. 2mn0. 3o2/graphite lithium-ion batteries with different socs. *Electrochimica Acta*, 495:144448, 2024.

[94] Hongpeng Lv, Depeng Kong, Ping Ping, Gongquan Wang, Hengle Zhao, and Xinyi Dai. Anomaly detection of lifepo4 pouch batteries expansion force under preload force. *Process Safety and Environmental Protection*, 176:1–11, 2023.

[95] Chunjing Lin, Jingbo Mao, Xiaotao Zhang, Tao Yan, Chuang Qi, Ju Yang, and Xuning Feng. A study of expansion force propagation characteristics and early warning feasibility for the thermal diffusion process of lithium-ion battery modules. *Journal of Energy Storage*, 98:113076, 2024.

[96] Simon F Schuster, Tobias Bach, Elena Fleder, Jana Müller, Martin Brand, Gerhard Sextl, and Andreas Jossen. Nonlinear aging characteristics of lithium-ion cells under different operational conditions. *Journal of Energy Storage*, 1:44–53, 2015.

[97] Peter M Attia, Alexander Bills, Ferran Brosa Planella, Philipp Dechent, Goncalo Dos Reis, Matthieu Dubarry, Paul Gasper, Richard Gilchrist, Samuel Greenbank, David Howey, et al. "knees" in lithium-ion battery aging trajectories. *Journal of The Electrochemical Society*, 169(6):060517, 2022.

[98] Meinert Lewerenz, Andrea Marongiu, Alexander Warnecke, and Dirk Uwe Sauer. Differential voltage analysis as a tool for analyzing inhomogeneous aging: A case study for lifepo4— graphite cylindrical cells. *Journal of Power Sources*, 368:57–67, 2017.

[99] Cedric Kirst, Alexander Karger, Jan P Singer, and Andreas Jossen. Non-destructive electrode potential and open-circuit voltage aging estimation for lithium-ion batteries. *Journal of Power Sources*, 602:234341, 2024.

[100] Meinert Lewerenz and Dirk Uwe Sauer. Evaluation of cyclic aging tests of prismatic automotive linimncoo2-graphite cells considering influence of homogeneity and anode overhang. *Journal of energy storage*, 18:421–434, 2018.

[101] Meinert Lewerenz, Alexander Warnecke, and Dirk Uwe Sauer. Post-mortem analysis on lifepo4— graphite cells describing the evolution & composition of covering layer on anode and their impact on cell performance. *Journal of Power Sources*, 369:122–132, 2017.

[102] Yingchen Xie, Shan Wang, Ruihe Li, Dongsheng Ren, Mengchao Yi, Chengshan Xu, Xuebing Han, Languang Lu, Benedikt Friess, Gregory Offer, et al. Inhomogeneous degradation induced by lithium plating in a large-format lithium-ion battery. *Journal of Power Sources*, 542:231753, 2022.

[103] Johannes Sieg, Mathias Storch, Johannes Fath, Adnan Nuhic, Jochen Bandlow, Bernd Spier, and Dirk Uwe Sauer. Local degradation and differential voltage analysis of aged lithium-ion pouch cells. *Journal of Energy Storage*, 30:101582, 2020.

[104] Johannes Philipp Fath, Daniel Dragicevic, Laura Bittel, Adnan Nuhic, Johannes Sieg, Severin Hahn, Lennart Alsheimer, Bernd Spier, and Thomas Wetzel. Quantification of aging mechanisms and inhomogeneity in cycled lithium-ion cells by differential voltage analysis. *Journal of Energy Storage*, 25:100813, 2019.

[105] Lars von Kolzenberg, Jochen Stadler, Johannes Fath, Madeleine Ecker, Birger Horstmann, and Arnulf Latz. A four parameter model for the solid-electrolyte interphase to predict battery aging during operation. *Journal of Power Sources*, 539:231560, 2022.

[106] Jochen Stadler, Carsten Krupp, Madeleine Ecker, Jochen Bandlow, Bernd Spier, and Arnulf Latz. Investigation and modeling of cyclic aging using a design of experiment with automotive grade lithium-ion cells. *Journal of Power Sources*, 521:230952, 2022.

[107] Victor W Hu and Daniel T Schwartz. Low error estimation of half-cell thermodynamic parameters from whole-cell li-ion battery experiments: Physics-based model formulation, experimental demonstration, and an open software tool. *Journal of The Electrochemical Society*, 169(3):030539, 2022.

[108] Sravan Pannala, Andrew Weng, Ian Fischer, Jason B Siegel, and Anna G Stefanopoulou. Low-cost inductive sensor and fixture kit for measuring battery cell thickness under constant pressure. *IFAC-PapersOnLine*, 55(37):712–717, 2022.

[109] Suhak Lee, Jason B Siegel, Anna G Stefanopoulou, Jang-Woo Lee, and Tae-Kyung Lee. Electrode state of health estimation for lithium ion batteries considering half-cell potential change due to aging. *Journal of The Electrochemical Society*, 167(9):090531, 2020.

[110] Marion Fuhrmann, Laurent Torcheux, and Yo Kobayashi. Knee point prediction for lithium-ion batteries using differential voltage analysis and degree of inhomogeneity. *Journal of Power Sources*, 621:235210, 2024.

[111] Hisashi Kato, Yo Kobayashi, and Hajime Miyashiro. Differential voltage curve analysis of a lithium-ion battery during discharge. *Journal of Power Sources*, 398:49–54, 2018.

[112] Pauli Virtanen, Ralf Gommers, Travis E. Oliphant, Matt Haberland, and SciPy 1.0 Contributors. SciPy 1.0: Fundamental Algorithms for Scientific Computing in Python. *Nature Methods*, 17:261–272, 2020.

[113] Tsutomu Ohzuku, Yasunobu Iwakoshi, and Keijiro Sawai. Formation of lithium-graphite intercalation compounds in nonaqueous electrolytes and their application as a negative electrode for a lithium ion (shuttlecock) cell. *Journal of The Electrochemical Society*, 140(9):2490, 1993.

[114] Andrew Weng, Jason B Siegel, and Anna Stefanopoulou. Differential voltage analysis for battery manufacturing process control. *Frontiers in Energy Research*, 11:1087269, 2023.

[115] George Baure and Matthieu Dubarry. Synthetic vs. real driving cycles: A comparison of electric vehicle battery degradation. *Batteries*, 5(2):42, 2019.

[116] Christiane Rahe, Stephen T Kelly, Mansoureh Nourozi Rad, Dirk Uwe Sauer, Joachim Mayer, and Egbert Figgemeier. Nanoscale x-ray imaging of ageing in automotive lithium ion battery cells. *Journal of Power Sources*, 433:126631, 2019.

[117] Christian Weisenberger, David K Harrison, Chengke Zhou, and Volker Knoblauch. Revealing the effects of microstructural changes of graphite anodes during cycling on their lithium intercalation kinetics utilizing operando xrd. *Electrochimica Acta*, 461:142629, 2023.

[118] Thomas Waldmann and Margret Wohlfahrt-Mehrens. Effects of rest time after li plating on safety behavior—arc tests with commercial high-energy 18650 li-ion cells. *Electrochimica Acta*, 230:454–460, 2017.

[119] Meinert Lewerenz, Georg Fuchs, Lisa Becker, and Dirk Uwe Sauer. Irreversible calendar aging and quantification of the reversible capacity loss caused by anode overhang. *Journal of Energy Storage*, 18:149–159, 2018.

[120] Meinert Lewerenz, Philipp Dechent, and Dirk Uwe Sauer. Investigation of capacity recovery during rest period at different states-of-charge after cycle life test for prismatic li (ni1/3mn1/3co1/3) o2-graphite cells. *Journal of Energy Storage*, 21:680–690, 2019.

[121] Christoph R Birkl, Matthew R Roberts, Euan McTurk, Peter G Bruce, and David A Howey. Degradation diagnostics for lithium ion cells. *Journal of Power Sources*, 341:373–386, 2017.

[122] Kuijie Li, Xinlei Gao, Shijian Peng, Shengshi Wang, Weixin Zhang, Peng Liu, Weixiong Wu, Huizhi Wang, Yu Wang, Xuning Feng, et al. A comparative study on multidimensional signal evolution during thermal runaway of lithium-ion batteries with various cathode materials. *Energy*, 300:131560, 2024.

[123] Weilong Ai, Ludwig Kraft, Johannes Sturm, Andreas Jossen, and Billy Wu. Electrochemical thermal-mechanical modelling of stress inhomogeneity in lithium-ion pouch cells. *Journal of The Electrochemical Society*, 167(1):013512, 2019.